# Numerical Modeling of Inclined Dense Jets in Stagnant Water on a Sloped Bottom

By

**Xinyun Wang**

Thesis submitted to the University of Ottawa
In partial fulfillment of the requirements
for the Master of Applied Science in Civil Engineering

Department of Civil Engineering

Faculty of Engineering

University of Ottawa

# Abstract

Desalination plants are becoming essential due to the limited water resources in order to reduce the pressure of high demand of freshwater in many countries in recent decades. A concerning problem associated with desalination plants is the high concentration brine which has high risk to marine environments. Inclined dense jets are commonly used to treat brine produced by desalination plants or in industrial outfall discharges. They are produced when the brine is discharged at an upwardly inclined angle through a pipe or a diffuser system. Previous studies have mainly focused on jets on a horizontal bottom. In the present study, the influence of sloped bottom is investigated by numerical simulations using a modified solver in OpenFOAM (pisoFoam). Four different Reynolds Averaged Navier Strokes (RANS) turbulence models (Realizable $k-\varepsilon$, Standard $k-\varepsilon$, RNG $k-\varepsilon$ and Nonlinear $k-\varepsilon$ were employed to assess the accuracy of the selected turbulence models in predicting the jet behavior. Jets of inclination angle of 30° with four different initial conditions (Froude number=15, 20, 25, 30) on three different bed slope angles (2°, 5°, 10°) in stagnant water were conducted. Although inclined dense jets of the discharge angel of 60° are more common in discharge systems, sometimes they cannot be used in shallow waters in order to prevent surface pollution. In such cases, a relatively small jet inclining angle can be used to prevent the surface pollution and as shown in this thesis, bed slope can enhance the brine mixing and dilution. The results showed that Realizable $k-\varepsilon$ model is more accurate among the turbulence models studied herein. The dilution at the impact point can be estimated based on the Froude number and initial conditions. After the impact point, the slope did enhance the dilution of the plume compared to the horizontal bed. The dilution was thus affected by the slope and the dilution after the impact point on the slope appeared to be linearly related to the distance to the source. Besides, the slope could enhance the jet dilution up to 20% compared with the horizontal bed after the impact point.

# Acknowledgments

This thesis signified the end of the master's study experience. These two years provided me with precious experiences and memories in Ottawa.

The external support of many people provided encouragement and confidence for me to finish the master study.

Firstly, I would like to thank my primary supervisor, Dr. Majid Mohammadian, for his constant encouragement and guidance since the first day I came to Ottawa. He always supports me whether it is in daily life or studying. He has walked me through all the stages of writing this thesis and gave me countless help and inspirations. I am deeply grateful for his help and patience in completing this thesis.

Secondly, I would like to thank Dr. Philip J. Roberts from the Georgia Institute of Technology. I still want to thank him because during the experiment setup stage in 2019, Dr. Philip J. Roberts has given me lot of useful suggestions and ideas for the research in the outfalls system. Without him, I cannot finish the setup of my experiments and some ideas in my research.

Thirdly, I would like to express my gratitude to Robert Quehl, for editing the thesis. I cannot complete this thesis that meets academic standards without him.

I also would like to thank professors in the department of Civil engineering, Dr. Colin Rennie, Dr. Ioan Nistor, Dr. Ousmane Seidou, all the people I met in the Lab and faculty, Mark Lapointe, Leo Denner, Dr. Leon Boegman, Dr. Amir Azimi, Luc Cloutier, and Paula Oppici who gave me lots of help and support for my experiments and study.

Finally, I would like to thank my friends, Xueming Wang, Ruoyao Ou, and my family (Mom, Dad, and Mohan Ni) for their support throughout these years.

# Table of Contents

# List of Figures

# List of Tables

# List of Acronyms

CFD: Computational Fluid Dynamic

DNS: Direct Numerical Simulation

FDM: Finite Difference Method

FEM: Finite Element Method

FVM: Finite Volume Method

GGDH: General Gradient Diffusion Hypothesis

IDJ: Inclined Dense Jet

LA: Light Attenuation

LES: Large Eddy Simulation

LIF: Laser Induced Fluorescence

LRR: Launder-Reece-Rodi (LRR)

PTV: Particle Tracking Velocimetry

PDE: Partial Differential Equation

PISO: Pressure-Implicit with Splitting of Operators

PIV: Particle Image Velocimetry

PLIF: Planar Laser Induced Fluorescence

RANS: Reynolds Averaged Navier–Stokes

RNG: Renormalization Group

SGDH: Standard Gradient Diffusion Hypothesis

SGS: Sub-Grid Scale

SST: Shear Stress Transport

# List of Symbols

| | |
|---|---|
| $b_c$ | Concentration spread width [m]; |
| $B$ | Buoyancy flux [m$^4$/s$^3$]; |
| $D$ | Diameter of nozzle[m]; and diffusion coefficient [m$^2$/s] |
| F | Densimetric Froude number; |
| $f$ | Body force on control volume[N]; |
| $F_{viscous}$ | Viscous force[N]; |
| $g$ | Gravity acceleration [m/s$^2$]; |
| $g'$ | Specific gravitational acceleration [m/s$^2$]; |
| L | Length scale[m]; |
| $\mathrm{L_q}$ | Source length scale [m]; |
| $\mathrm{L_m}$ | Momentum length scale [m]; |
| m | Mass of control volume[kg]; |
| $M$ | Momentum flux[N·s·m$^{-2}$·s$^{-1}$]; |
| $Q$ | Mass flux[kg/s$^{-1}$m$^2$]; |
| $P$ | Pressure [N/m$^2$]; |
| Re | Reynolds number; |
| r | Radial distance from jet centerline [m]; |
| $s$ | Distance along trajectory[m]; |
| S | Salinity in Eqn. 3.9; |
| $\mathrm{S}_{ij}$ | Strain rate tensor; |
| $S_c, S_m$ | Dilution value of the jet centerline peak; |
| $S_r$ | Dilution value of return point; |
| $S_i$ | Dilution value of impact point; |
| T | Temperature [℃]; |
| $U_0$ | Velocity at source [m/s]; |
| $u, v, w$ | Velocity in the *x*, *y*, *z* direction, respectively[m/s]; |
| $x, y, z$ | Coordinates; |
| $X_0$ | Horizontal location of nozzle [m]; |
| $Y_0$ | Vertical location of nozzle [m]; |
| $X_c$ | Horizontal location of centerline peak [m]; |
| $X_t$ | Horizontal location of terminal rise height [m]; |

| | |
|---|---|
| $X_t$ | Horizontal location of return point [m]; |
| $X_i$ | Horizontal location of impact point [m]; |
| $X_i$ | Vertical location of impact point [m]; |
| $Y_c$ | Vertical location of centerline peak [m]; |
| $Y_t$ | Terminal rise height [m]; |
| $\alpha$ | Inclination angle [°]; |
| $\beta$ | Slope angle [°]; |
| $\varepsilon$ | Dissipation rate in $k-\varepsilon$ models[$m^2/s^3$]; |
| $k$ | Turbulent kinetic energy[$km^2/s^2$]; |
| $\nu$ | Kinematic viscosity [$m^2/s$]; |
| $\rho_0$ | Density of jet [$kg/m^3$]; |
| $\rho_a$ | Density of ambient water [$kg/m^3$]; |
| $\rho_t$ | Water density as a function of temperature [$kg/m^3$]; |
| $\mu_t$ | Turbulent viscosity; [ $m^2/s$]; |
| $u_i'u_j'$ | Reynolds-stress[Pa]; |
| $u'$ | The fluctuation of the velocity component [m/s]; |
| $\omega$ | Dissipation rate in $k-\omega$ models[$m^2/s^3$]; |
| $C, \eta, \sigma, \gamma, A$ | Constants in numerical or mathematical models; |

# Chapter 1 Introduction

## 1.1 Background

The demand for water supply has considerably increased along with the increase of the population. More than 2 billion people live in countries with severe water shortages, and over 60% of the global population is predicted to face severe water scarcity by 2025 (Schewe *et al.*, 2014). However, according to the databases of the World Health Organization, less than 3% of water is fresh water and less than 1/3 of that can be used by humans on this planet since 2/3 of freshwater is found frozen in the glaciers, while 97% of the other water is in the oceans (UNESCO, 2019). With the tremendous risk of water resource scarcity, seawater has been addressed as a significant potential alternative to alleviate water scarcity.

Desalination, the process of removing the salt from seawater to produce water that meets the various requirements, has become the most popular way to produce freshwater for agricultural applications and other uses in recent decades. There are almost 20000 desalination plants in the world that provide water to more than 300 million people all over the world. About 150 countries rely on desalination plants to meet their freshwater needs, and more than 48% of desalination plants are located in the Middle East and North Africa (Jones *et al.*, 2019). Although desalination plants have excellent potential for providing sustainable water resources, the planning and design of desalination plants have gained considerable attention concerning environmental issues in the coastal areas since the 1970s (Holly and Grace, 1971).

In the process of desalination, a major concern is the treatment of the highly concentrated salty water. Although there are several alternatives for disposal of the brine, one of the most economically attractive and easiest ways is to discharge it back into the ocean to dilute it because the brine has almost the same constitution as seawater (Latteman *et al.*, 2010). The salinity of the discharged brine is usually 10~20% higher than the receiving water, sometimes reaching 30%, and is 5 ℃ ~15 ℃ warmer than the ambient seawater. The density difference between brine and ambient seawater is a key factor that controls the mixing and spreading process. Since the brine is heavier than ambient water, if it is discharged directly without any treatment, the discharge plume will sink to the seafloor and flow along the seabed forming a massive polluted water area and may cause fatal effects unless it is adequately dissipated. It is not only harmful to humans, plants and animal life, but might be injurious to the whole ecosystem (Al-Mutaz, 1991). It is essential to research the characteristics present during the mixing process and to use various approaches to obtain a comprehensive understanding of mixing at outfall systems, to predict and minimize the potential negative effects to the surrounding ecosystems.

Based on these factors, the outfall systems of desalination plants must be designed properly, as they affect the mixing behavior in the near-field region, which can extend to hundreds of meters from the outfall system. Some desalination plants have applied direct discharge strategies, such as Al-Jubail desalination plants (Baig and Al Kutbi, 1998), where the brine is discharged through a 1.8 km long cascading channel to achieve a high dilution rate. This can be seen as surface discharging channels, which are economically friendly, but this strategy has a high risk of harm to organisms living in shallow water, and it will cause larger water surface pollution. Compared with the directly discharged strategies, the most effective method to discharge brine water from desalination plants is via a submerged outfall system – which terminates in diffuser sections with single port or multiple ports. Negatively buoyant jets ($\rho_{jet} > \rho_{ambient}$) are frequently used with such diffusers. The mixing of inclined dense turbulent jets has been an area of interest concerning the outfalls of desalination plants or wastewater treatment plants.

Depending on local regulations, a certain minimum dilution must be achieved at the worst receiving condition, which means the velocity of ambient water is possibly zero. If the minimum dilution can be reached in stagnant water, then it can be reached in most cases, since the outfall systems are typically in the presence of cross-flow or waves in real life. As a result, many studies have been conducted on inclined dense jets in stagnant ambient water.

Typically, the brine-fluid will be discharged upwards from a single-port (or multi-port) diffuser located on the sea bed, and because it is denser than the ambient water, the jet will reach the highest point then return back to the sea bed at impact point (return point) where it continues to spread as a gravity current (Figure 1.1). As a result, the location of the hightest point and return point and dilution at these points must be estimated to make sure that the design is adequate and local dilution regulations are met. The discharge angle can range from 0°~90°, usually 90° is not included because the vertical discharge is more popular in positive buoyant jets ($\rho_{jet} < \rho_{ambient}$), and this type of jet will not fall back to the discharge outlet in stagnant water. In some discharge environments with sloped bottoms, there are two different types of discharge (Figure 1.2). The direct discharge can cause tremendous seashore impact and high risk of pollution on the slope with very low dilution rates(Figure 1.2.a). When the brine is discharged as an inclined turbulent jet, the mixing efficiency is elevated(Figure 1.2.b). After the impact point, the jet can continue to flow along the slope bottom, causing more mixing.

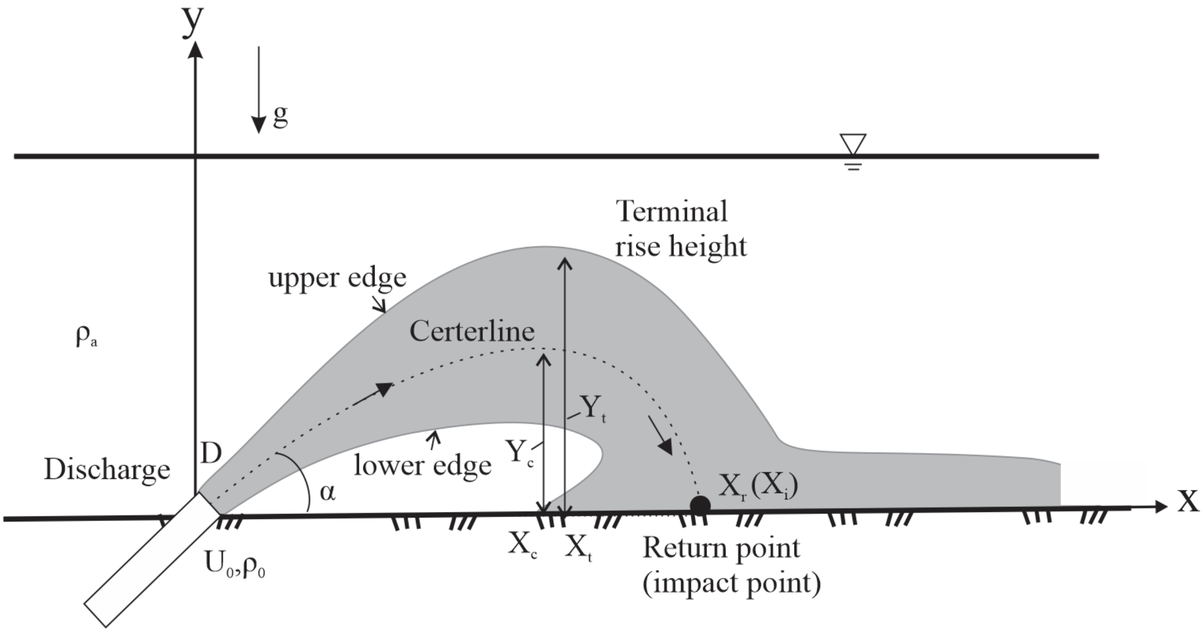

Figure 1.1 Schematic diagram of an inclined dense jet (discharge angle $\alpha$) in stagnant water

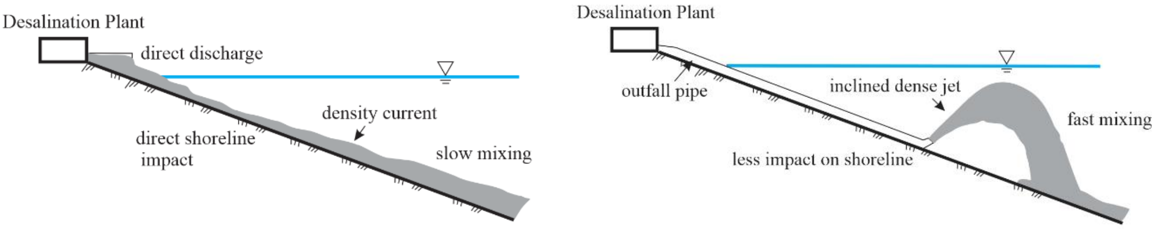

(a) Directly discharge (b) Inclined dense jet

Figure 1.2 Two discharge methods at the desalination plants outfalls (modified after Bleninger (2008))

Numerous studies of inclined dense jets in stagnant ambient water on a horizontal bottom have been carried out both experimentally and numerically. Research studying the maximum height and return points have been carried out in recent years. Many studies pointed out that discharge angles (30°~90°) above horizontal have great advantages; these are related to better dilution levels at the impact point (impingement point). Zeitoun (1970) carried out the first experiment on inclined dense jets with discharge inclination of 30°, 45°, and 60°, this experiment shows that 60° could provide the maximum dilution in stagnant water. The “optimal angle of 60°” was adopted and approved in subsequent experiments from many studies (Roberts and Toms, 1987) (Roberts *et al*., 1997). Roberts *et al*., (1997) also carried out one comprehensive investigation of inclined dense jet with 60° in stationary water focusing on the dilution along the bottom layer. Similar experiments on inclined dense jet are carried out by numerous researchers (Bloomdields and Keer, 2002)( Cipollina *et al*., 2005) (Kikkert *et al*., 2007 & 2010) (Oliver *et al*., 2013b).

Many techniques have been used to measure these geometric characteristics such as photographs and point measurements. Photographs provide comprehensive and uesful location information, while conductivity probes combined with the point measurements can calculate the salinity levels and obtain the dilution information. At the same time, modern technologies provide more accurate results for concentration and velocity without intrusive measurements, such as Light Attenuation (LA), Laser-Induced Fluorescence (LIF), Particle Image Velocimetry (PIV) and Particle Tracking Velocimetry (PTV)(Ramakanth, 2016). Numerical models and CFD simulations have also had great achievements, and many software programs have proven to be useful tools in predicting the mixing process in outfall designs. Different numerical simulations of inclined dense jets have been performed by various authors and their works, including commercial integral models (CorJet, VISJET, Visual Plumes) (Bleninger and Jirka, 2008)(Frick,1984)(Jirka, 2008), or non-hydrostatic methods by solving Reynolds-averaged Navier-Stokes (RANS) or Large Eddy Simulations (LES). RANS and LES models have been also employed using open-source toolboxes or software such as OpenFOAM and Ansys Fluent (Mohammadian *et al*., 2020)(Gildeh *et al*., 2015)(Gildeh *et al*., 2014)(Zhang *et al*., 2016). All these studies have provided dimensionless coefficients to predict key quantities of the jet mixing, such as the location and dilution of the terminal height as well as impact or return points.

## 1.2 Objectives of the study

Jets with different angles have been studied frequently; however, not only will the initial condition of the jet itself affect the mixing progress, the ambient and the bottom of the receiving floor will also affect the mixing process; the bottom of the floor is under high risk because the jets are usually denser and they will flow along the bottom eventually.

The boundary conditions have also been of interest in jet studies. Thus, the main objectives of this study are:

1- To evaluate the performance of numerical models in the simulation of inclined dense jets in stagnant water on a **sloped bottom** in OpenFOAM;

2- To verify the simulation results, focusing on the concentration fields and finding more accurate models for simulation;

3- To investigate the effect of sloped bottoms on the mixing of inclined dense jets in stagnant water.

In order to achieve these objectives, numerical studies have been carried out. OpenFOAM is the main software used in this project to run all the simulations, and the process is explained in detail in Chapter 3.

### 1.3 Novelty of the study

Inclined dense jets in stagnant water have been studied broadly. Most of them focus on the jet's characteristics before the impact point (return point) or neglect the bottom's influence. There are very few studies that have been done on the characteristics of inclined dense jets beyond the impact point; the numerical modeling in this field is currently in progress in the literature. Understanding the jet development after the impact point on sloped bottoms is necessary, and considering more practical applications, the sea beds in real life are not always horizontal. This leads this study to focus on the sloped bottom boundary condition, which influences the mixing of the brine after the impact points.

This research presents a 3D OpenFOAM numerical study on the mixing of inclined dense jets on a sloped bottom. This is the first time, to the best of the author's knowledge, that numerical modeling is used to simulate inclined dense jets on a sloped bottom. Moreover, in this study, several turbulence models have been studied and evaluated to choose the best one that can be used in the outfall design of desalination plants and the wastewater treatment industry.

### 1.4 Organization of thesis

This thesis includes five chapters as detailed below:

Chapter 1 is the introduction. Chapter 2 presents a comprehensive literature review of inclined dense jets in stagnant water experimentally and numerically. Also, this chapter discusses different turbulence models that have been developed to simulate incompressible turbulence flows. Chapter 3 provides the theoretical concept of numerical models and the process to develop the model using the OpenFOAM toolbox. Chapter 4 presents a technical paper: Numerical modeling of inclined dense jets in stagnant ambient water on a sloped bottom, which contains the results from numerical simulations. Chapter 5 presents some concluding remarks and ideas for future study.

# Chapter 2 Literature Review

## 2.1 Introduction

As mentioned in the introduction chapter, it is necessary to properly design outfall systems to protect the marine environment. These discharges usually lead to the formation of turbulent jets. Turbulence appears in unsteady flows that have significant fluctuations or mixing and dissipation. The Reynolds number is used to distinguish turbulent jets and laminar flow (White, 2010), which is defined as Equation 2.1; the turbulence occurs with a high Re value (e.g. $> 3000$).

$$\mathrm{Re} = \frac{UL}{\nu} \tag{2.1}$$

This number is dimensionless. U is a velocity scale, L is a length scale, and ν is the kinematic viscosity of the fluid. The behavior of the jets is quite different under different temperatures and densities, or environmental conditions.

A typical negative buoyant jet is shown in Figure 2.1. It features a nozzle inclined upwards to horizontal with an angled discharge (α) through a round nozzle with diameter D at the velocity $U_0$.

As mentioned, negative buoyant jets are used as a common discharge method for desalination plants. They are discharged upwards in the form of inclined dense jets. At the discharge point, the jet momentum is sufficient to overcome the negative buoyancy so that the jets can rise. As the jet is rising, the negative buoyancy force ultimately becomes sufficient to reduce the upward momentum to zero, and then the jet will fall because of the gravitational force. This process can enhance the mixing efficiency because it can increase the mixing length with an angle on the discharge. Therefore, every inclined jet with a negative buoyancy will have a terminal rise height that will be determined by the ratio of the initial jet momentum flux and the buoyancy forces on the jet. The jet will eventually fall back to the sea floor due to its higher density, and it will continue spreading and mixing with the ambient water.

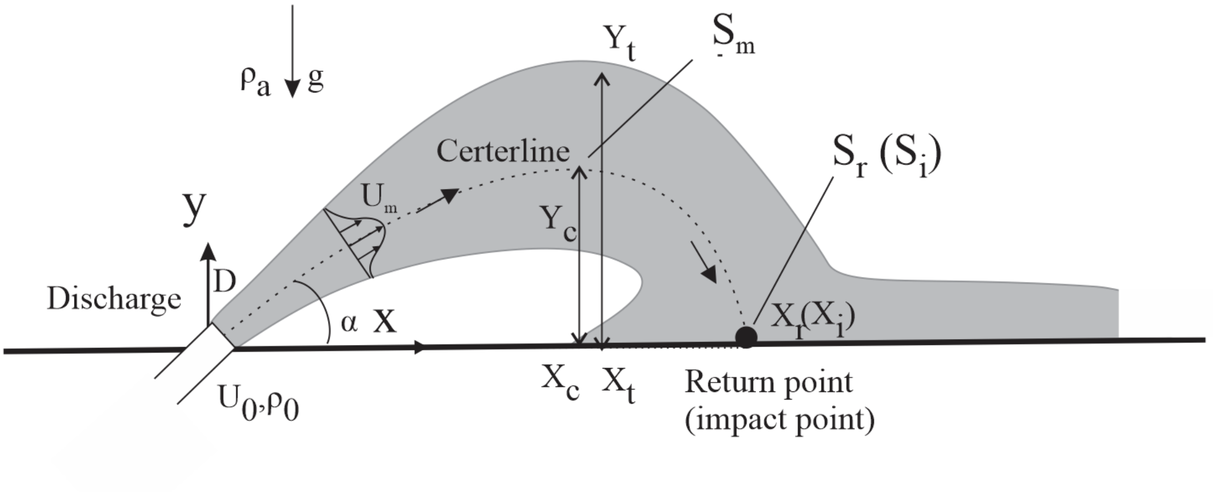

Figure 2.1 Schematic diagram of a typical negative buoyant jet on a horizontal bottom

For making experimental data suitable for large-scale industrial design, it is necessaey to use dimensionless parameters. In the range of inclined dense jets, the typical dimensionless parameter is the initial densimetric Froude number (F). It is the ratio of jet momentum flux to the buoyancy forces on the jet. The jet Froude number can be written in terms of three variable that define the jet, they are:

1) The kinematic momentum flux M, which can be written as

$$M = \pi D^2 {U_0}^2/4 \tag{2.2}$$

Where D is the nozzle diameter and $U_0$ is the jet velocity.

2) The volume flux of the jet which is given by

$$Q = \pi D^2 U_0/4 \tag{2.3}$$

3) The kinematic buoyancy flux which is calculated as

$$B = g'Q \tag{2.4}$$

where g’ is specific gravitational acceleration, defined as $g' = g\frac{\Delta\rho}{\rho_0}$, where $\Delta\rho = \rho_a - \rho_0$, $\rho_0$ is the density of the jet and $\rho_a$ is ambient density.

The Froude number F is defined as

$$F = \frac{M^{5/4}}{QB^{1/2}} = \left(\frac{\pi}{4}\right)^{-\frac{1}{4}} (\frac{\rho_0}{\rho_a})^{\frac{1}{2}} \left(\frac{{U_0}^2}{g'D}\right)^{\frac{1}{2}} \tag{2.5}$$

Most research adopt part of (2.5) as densimetric Froude number, F, which is

$F = \frac{U_0}{\sqrt{Dg'}}$. This definition is also adopted in this study.

From these fluxes, two important length scales have been addressed by many authors (Roberts *et al.*, 1997), and are commonly used in jet analysis.

$$L_m = \frac{M^{3/4}}{B^{1/2}} = (\frac{\pi}{4})^{\frac{1}{4}} \frac{U_0 D}{\sqrt{g'D}} = (\frac{\pi}{4})^{\frac{1}{4}} DF \tag{2.6}$$

$$L_q = \frac{Q}{M^{1/2}} = (\frac{\pi}{4})^{\frac{1}{4}} D \tag{2.7}$$

$\mathrm{L_q}$ is the distance where the initial volume flux approximately equal to volume flux of the entrained ambient fluid (Nemlioglu *et al.*, 2014). $\mathrm{L_m}$ is the distance where jet momentum shows more dominance than buoyancy. The initial volume flux becomes dynamically unimportant when the distance from the nozzle is much greater than $\mathrm{L_q}$ (Roberts *et al.*, 1997).Important dimensional analyses and dimensionless parameters in jet studies are provided in the following. For a dense jet with an angle to horizontal $\alpha$ in a stagnant ambient, the terminal rise height of jet $Y_t$ can be given by

$$\frac{Y_t M^{1/2}}{Q} = f_1(F, \alpha) \tag{2.8}$$

If jet discharge angle is fixed, the jet behaviour is dominated by the momentum flux and buoyancy flux, thus (2.8) can be rewritten as

$$\frac{Y_t}{L_m} = f(\frac{L_m}{L_q}) \tag{2.9}$$

When $\frac{\mathrm{L_m}}{\mathrm{L_q}} \gg 1$, the source volume flux Q is dropped out from effective parameters. So Eqn. (2.9) can be written as

$\frac{Y_t}{l_m} = C$; or $\frac{Y_t}{DF} = C_1$

C and $C_1$ is a constant that can be derived from experiments.

Similarly, the location of the centerline peak can be written as $\frac{X_c}{DF} = C_2$ , $\frac{Y_c}{DF} = C_3$ .

The dilution of the jet at the centerline peak can be defined as

$$S = \frac{\rho_0 - \rho_a}{\rho_c - \rho_a} = f_2(F, \alpha) \tag{2.10}$$

When the discharge angle is fixed, it can be written as $\frac{S}{F} = C_4$

($\rho_c$ is the maximum mean density at the centerline peak $((X_c, Y_c))$ of the jet)

The impact point is also important because the additional mixing will happen in the spreading layer downstream beyond the impact point, causing the dilution to increase along the bottom. The dilution and the location of the impact point $S_i, x_i$ (it can be seen as return point with horizontal bottom) is also essential, and can be obtained from

$$\frac{X_i(X_r)}{DF} = C_5\,; \frac{S_i(S_r)}{F} = C_6 \tag{2.11}$$

In the early stages of the research, many studies focused on $f_1(F, \alpha)$ ,$f_2(F, \alpha)$ and related coefficients $C_1$ , $C_4$, $C_{5,}$ $C_6$ with different discharge angle $\alpha$, because the terminal height and dilution are the important parameters of the outfall design. Many studies have been developed based on experiments and numerical models, which will be reviewed in detail below.

## 2.2 Experimental studies

Negative buoyant jets have been explored by many researchers, including vertical jets and inclined dense jets. In many experiments, dyed fluids have been commonly employed to illustrate dense jet physical characteristics. Most of them take photographs and apply point measurements. The former can provide valuable quantitative information on the jet's trajectory, and the latter can provide information about the dilution at any point. Bosanquet *et al.*, (1961) were the first to experiment with negative jets by applying Prandtl mixing length theory (Prandtl, 1925) and flow concepts from Groume-Grjimailo (1923). They studied horizontal and 45° inclined negative buoyant jets using diluted magnetite slurry, which can provide both color and density differences. However, the instant photo can only show the outline of the jets; the concentration and location of the brine are not easy to recognize visually in the photo. Later, Turner and James (1966) and Zeitoun *et al.*, (1970) performed plenty of experiments with vertical dense jets. Zeitoun and William (1971) used a laboratory model to estimate the average height of these jets in various flow conditions and density differences. and they obtained the terminal rise height of the jet from their experiments. Different authors got different results of jet’s height because it was found to be very difficult to measure near the top of the jet due to the fluctuations. But they all found that the dilution of the vertical jets is limited because the jet will fold on itself. At the same time, the vertical jet might have sufficient momentum to reach the surface of the receiving water and might spread and encompass a larger area than the completely submerged jets. Thus, the applications of vertical jets are quite limited.

Zeitoun and William (1971) also tried to determine the mixing characteristics of jets with inclination angles of 30°, 45° and 60°. They used Rhodamine B as a tracer to determine the trajectories, and the time-averaging photo shots were applied. The concentration measurements were carried out by extracting point samples. They found that the non-dimensionalized maximum edge varied with the discharge angle; however, the non-dimensionalized location of the return point can be almost the same. They also found that the 60° angle of the nozzle can produce the maximum trajectory path and maximum dilution under the same condition of initial flow.

Roberts and Toms (1987) carried out an experiment on an inclined dense jet with dye (Rhodamine B) and photographs in stagnant and flowing water. They studied dilution and trajectories of jet with 60 ° and 90 ° inclination. The concentration measurements were determined by fluorometer with vertically arranged sampling tubes. The terminal height was determined by averaging the "height of the top of visible dye plume". However, using photographs and the naked eye to track the dilution trace is not precise or accurate.

Lane *et al.*, (1993) made some progress by using shadowgraph images to capture the jet maximum rise height, and conductivity probes were used to measure the concentration profile spot by spot (Figure 2.2). They found that near the source, the plume is symmetric but changes to asymmetric downstream. The detrainment of a plume can be observed on the lower side, which leads that the upper boundary is sharper than the lower one.

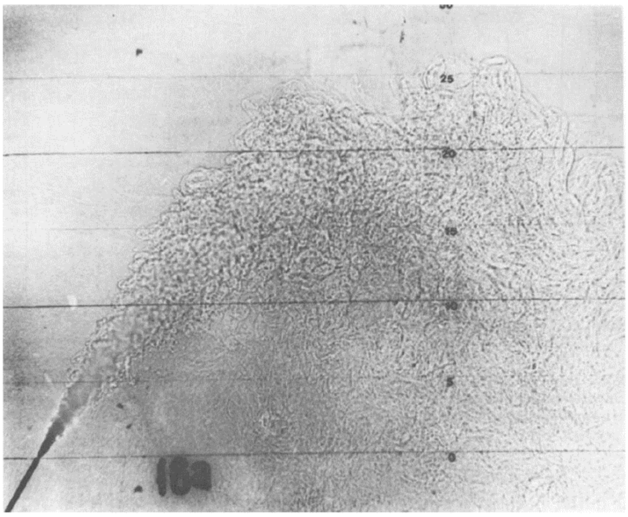

Figure 2.2 Shadowgraph of the negative buoyant jet at 60° source inclination (From Lane-Serff *et al.*, (1993))

In 1994, Lindberg (1994) performed experiments at 30°,45°, 60° and 90° inclinations using the same shadowgraph technology to measure the location of terminal rise. They found all the length scales increase with higher inclination angles.

Bloomfield and Kerr (2002) ran some experiments on inclined turbulent fountains using the shadowgraph method and recorded videos of the results, including different discharge angles from 0° to 60° to the vertical (30° ~ 90° to horizontal). For less confusion, the jet angle to the horizontal is adopted. During the experiments, they found that the final fountain height was smaller than the initial maximum height due to the interaction between the up-flow and down-flow (Figure 2.3). This interaction between the up-flow and down-flow for jets with an inclination angle was smaller than a vertical fountain. The initial fountain height increased with the increase of the discharge angle. The maximum terminal height can be reached at the inclination angle of 80 ° (to the horizontal axis).

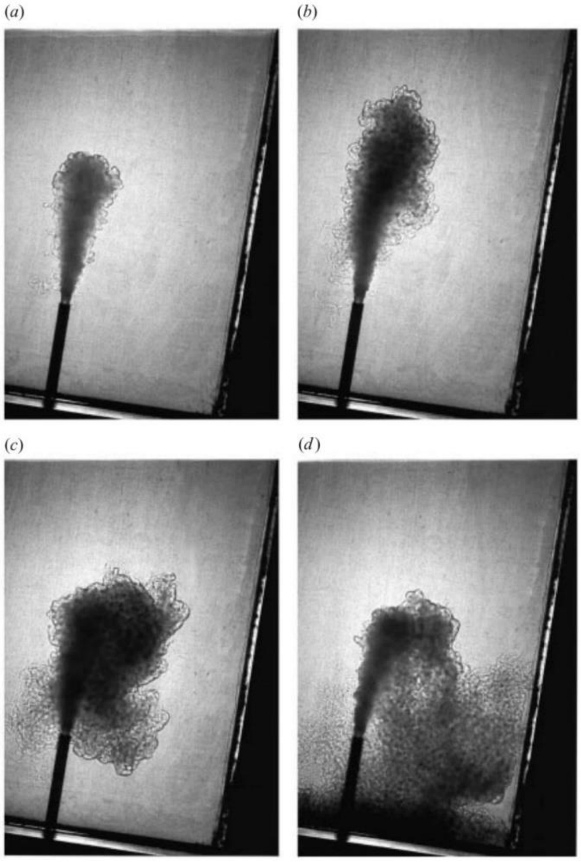

*(a) flow is jet-like at initial stage (b) The jet reach an initial maximum height (c) Interaction between upward and downward plumes (d) The jet has a smaller final height*

Figure 2.3 Photographs of the turbulent fountain with a discharge angle of 80 degrees (From Bloomfield *et al*. (2002))

Later, Cipollina *et al*., (2005) used photos to capture the geometry of jets with different inclination angles with a large range of Froude numbers (13 to 120). Three different angles (30° , 45°, 60°), different nozzle diameters, density differences and flow rates were also employed in this research, they found that all the parameters were correlated to the Froude number. At the same time, they found that a moderate difference of viscosity was not affecting the properties of the jets, which implied that the geometrical properties of jets was independent of the Reynolds number, which was consistent with previous studies (e.g. Roberts *et al*. 1997).

Papakonstantis *et al*. (2011a and 2011b) used photo images and a conductivity probe to do detailed research about the geometry and concentration characteristics of dense jets with inclinations of 45° 60° and 75°. They also measured the turbulence intensity variation. All the experimental results were in agreement with previous studies.

Bashitialshaaer *et al*., (2012) focused on the geometric characteristics of inclined dense jets by changing five initial jet parameters, including different discharge angles, nozzle diameters, jet densities and flow rates. All the results were recorded by the video camera. Five geometric quantities relevant to the design of the brine discharge systems were proved to be related to densimetric Froude number. This study also observed that the analysis of inclined dense jet had a limitation of Froude number (less than 100). This is because the data scatter increased significantly with large Froude numbers. They also found that, in agreement with other studies, 60 inclination angle showed better dilution than other angles (30° or 45°).

Besides using photographs and shadowgraphs in physical experiments, which might cause subjective errors, some other new and popular techniques are applied in jet studies, such as Laser-Induced Fluorescence (LIF), Particle Image Velocimetry (PIV) and Particle Tracking Velocimetry (PTV). These techniques not only can provide precise results including concentration and motion trail changing but also can give more information at any desired cross-section and plane such as a 2D or 3D view of the flow velocity field or concentration.

Laser-Induced Fluorescence (LIF) is described by Ferrier *et al*. (1993). Except for water flows and jet mixing analysis, this technique is also widely used in many areas including art pigment (Anglos *et al*. 1996) analysis, biochemical (Chen *et al*. 2001) or temperature analysis (Coolen *et al*. 1999). The basic setup of LIF is shown in Figure 2.4.

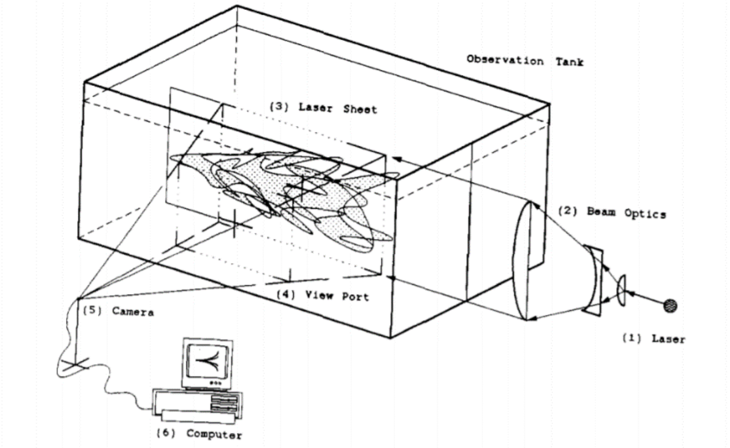

Figure 2.4 The schematic diagram of laser-induced fluorescence (LIF)(From Ferroer *et al*., 1993)

With this technology, a clearer picture of concentration fields can be obtained because this system can capture the entire concentration filed repeatedly in 1/30s intervals over thousands of points in the plane.

There is another technique usually applied to detect the movement of turbulent flow: Particle Image Velocimetry (PIV) or Particle Tracking Velocimetry (PTV). These measurement techniques have undergone dramatic development and application in fluid dynamics in the last two decades ( Sciacchitano *et al*., 2012)( Scharnowski *et al*., 2013). The essential components of the PIV system are a light to illuminate the flow area and a camera to capture the image continually, which can provide flow velocity fields. This system always works with a laser system. Figure 2.5 shows the schematic of PIV (McKendrick 2015).

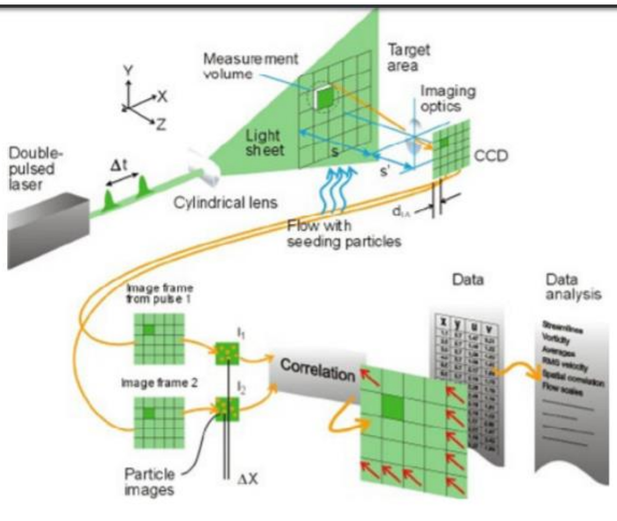

Figure 2.5 The schematic of particle image velocimetry (PIV) system

(*From Dantec Dynamics, website:www.dantecdynamics.com*)

With this new technology, the study of inclined dense jets has developed quickly, and more accurate results have been obtained. Roberts *et al*. (1997) preformed experiments on inclined dense jet with an angle of 60°, performed with LIF and microconductivity probes, focused on the impact point and the flow beyond it. They defined the end of the mixing zone where the intensity of concentration fluctuation falls to 5% of the average value, and the parameters of the terminal height and dilution and other jet characteristics were also presented, which is quite practical in outfall design. Kikkert *et al*. (2007) performed some research on inclined dense jets using LA technology and LIF techniques. They developed an analytical solution to predict the jet trajectory and then compared it with the results of their own experiments as well as previous studies (Zeitoun, 1971)(Roberts *et al*., 1997). Their analytical solution provided reasonable predictions of jets with inclination ranging from 0 to 75°with a large range of Froude number (14 to 99). They conducted another study in 2010 (Kikkert *et al*. 2010) that investigated the behaviors of jets under the influence of ambient flow with five discharge conditions and measured the three-dimensional trajectories of jets with LA technology.

PIV measurements are also commonly used in jet research. Shao and Law (2010) incorporated Particle Image Velocimetry (PIV) and Planar Laser Induced Fluorescence (PLIF) to collect the velocity and concentration field data in inclined dense jets with discharge angles of 30 and 45° . The mixing and dilution, including geometric properties, were carried out. Lai and Lee (2012) presented a comprehensive experimental investigation on inclined dense jets with six different angles, ranging from (15°~60°). LIF and PIV were applied in this study to provide jet mixing characteristics and turbulence properties including velocity data, geometric features and dilution data.

Other than experimental studies, the different models are also becoming popular in jet studies; combining experiments and model prediction methods can provide more comprehensive information and a wider scope of applications. There are many specialized modeling methods to simulate pollution development from the outfall systems. They included empirical and analytical methods, integral models and CFD models, as described in the following.

## 2.3 Empirical and analytical methods and integral models

The region of discharge influence can be divided into near field and far field. In this thesis, the entire study is about the near field. Based on the advection and diffusion mechanisms, many methods have been carried out to provide a better understanding of discharge behavior.

Empirical solutions are mainly used in near field solutions to obtain the important parameters related to the jet's characteristics. The basic idea of using dimensionless analysis is that it can scale results from the laboratory to full-scale design, and as mentioned in the introduction of this chapter, many researchers have used them and keep improving them.

Analytical solution refers to the use of simplified derivations to solve governing equations (McCutcheon, 2006). Cipollina *et al*. (2004) used an analytical approach to predict the behavior of inclined dense jets including four jet parameters which resulted in a set of algebraic and differential equations; the results showed good agreement with previous studies.

The Lagrangian jet model VISJET has also been explored in experimental jet studies (Cheung *et al*., 2000)(Lai and Lee, 2012). This model has also been widely used in the study of the interaction between jets and crossflow (Lee and Chu, 2012), (Choi *et al*., 2016), (Lai and Lee, 2014).

Jirka (2004) presented a set of equations for buoyant jets in different ambient water conditions including uniform stagnant water and moving water with "CorJet" software. This method has been accepted in many studies, and has been compared with other integral models and has demonstrated a good correlation (Davidson and Nokes, 2007).

Papanicolaou *et al*., (2008) presented Gaussian and "top hat" integral models for inclined dense jets, especially for vertical jets. They compared their predictions with the concentration measurements in the experiments and showed that the "top hat" model performed better than the Gaussian model. Based on their research, some new models such as the "Forced Jet" model have been studied by various researchers (Carazzo *et al*., 2010).

Numerous studies focus on the empirical coefficients of the jet characteristics on inclined dense jets on a horizontal bottom based on experiments and modeling; these parameters and coefficients are collected by the author and shown in **Appendix A**.

Jirka (2008) was the first researcher to study the influence of the bottom with slopes on submerged negatively buoyant jet mixing (Figure 2.6).

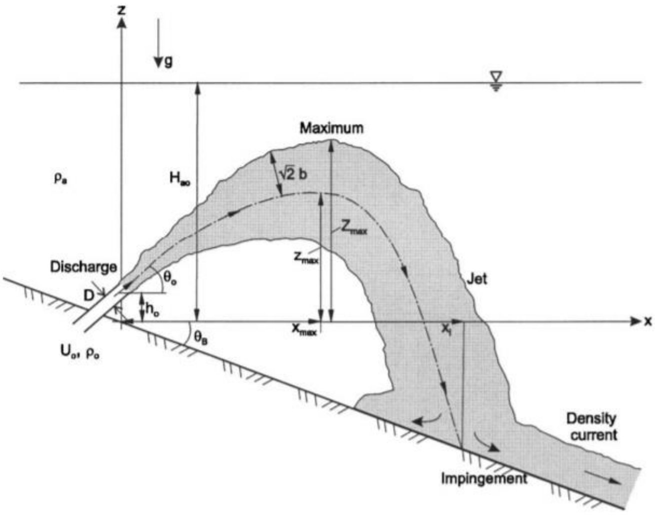

Figure 2.6 Schematic side view of inclined dense jet in stagnant ambient wanter on sloping bottom(From Jirka, 2008).

The integral model CorJet was validated with existing research data on trajectory and dilutions. After validating the model, the entire scope of discharge from 0°~90° and for the various slope angles (0°~30°) with zero discharge height were applied in this model, and the predictions of jet behaviour and information at the impact point over the variable bottom angle were presented. Normalized centerline trajectories with different possible bottom slopes are shown in Figure 2.7.

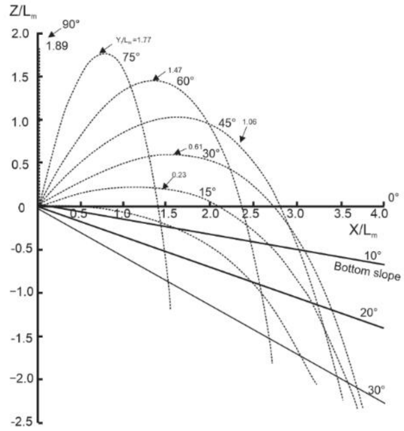

Figure 2.7 Trajectory of inclined dense jets with different angles of discharge and sloping bottom (Modified from Jirka, 2008)

In Figure 2.7, it is shown that with a horizontal bottom, the largest offshore impact point can be provided with a discharge angle of 30°- 45°.

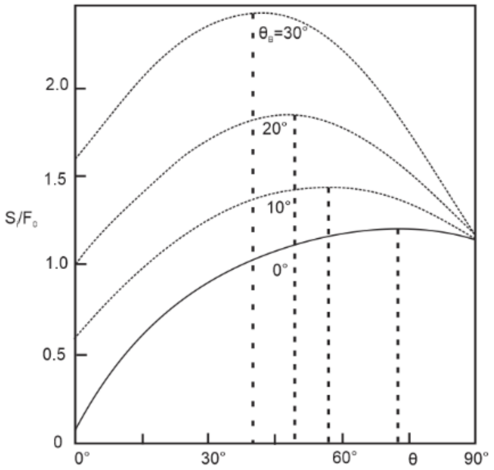

Figure 2.8 Dilution at impact point with different inclination and different sloped angle using Corjet (Modified after Jirka 2008)

Figure 2.8 shows the normolized dilution at the impact point with different discharge angles ($0^{\circ} \leq \theta_0 \leq 90°$) and sloped angles (0°,10°,20°,30°). With the horizontal bottom, the maximum dilution can be obtained from the discharge angle of 60° - 75°, which can lead the jet reach the surface and cause pollution when there is no enough water depth. With a moderate (sloped bottom$10^{\circ} \leq \theta_B \leq 20°$), the maximum dilution at the impact point can be reached with discharge angel around 45-60°, while for a strong slope ($\theta_B = 30°$), the maximum dilution occurs for a flatter discharge angle around 30°-45°. This figure shows that the maximum dilution at the impact point can be obtained with the discharge angel 45° and the 30° sloped bottom. The conclusion is that discharge angles (30°~45°) with a sloping bottom can be utilized for better dilution levels. A flatter discharge angle can allow the discharge port to be located more near shore in weak ambient current conditions (shallow ambient water).

In the abovementioned paper, the author just gave the trajectory prediction based on the modified model without any experimental results for the sloping bottom.

Another study provided a semi-analytical solution of jet characteristics with different discharge angles (30~60°) and different nominal bottom angles (5~15°) (Oliver *et al.* 2013). This semi-analytical solution was based on the analytical solution from Kikkert *et al.*, (2007). Oliveralso compared their results with experiments from their own work (Oliver 2012) and discussed the details of impact and return points (results are shown in 2.4). In their experiments, they removed the physical bottom to find out the jet characteristics on the nominal boundary.

Nikiforakis *et al*. (2014) presented the first experimental study of inclined dense jets on a sloped bottom. They performed point measurements by conductivity probes to get concentration information of the jet after the impact point with different Froude numbers (11~23). they found that the vertical concentration profiles after the impact point are almost linear, while the dilution value for discharge inclination 60° is higher than 45°. However, they didn't provide information about geometric and mixing properties at the impact point, and they also did not compare their results with other research studies.

## 2.4 Impact point and return point

As mentioned before, the impact point has also been studied in many studies because the inclined jet falls back to the bed eventually, and mixing is significantly reduced after the impact point because the effluent will stay attached to the horizontal boundary. Technically speaking, the return point and impact point are different only when the discharge port has an elevation height because the definition of the return point is when the jet returns at the same elevation as the discharge height. There are still some arguments about the impact point and return point; in many studies, these two points are regarded as the same point because of the small distance between them; as a result, these two points are only worth discussing when there is a slope at the bottom or jet has a large elevation height at outfall (Figure 2.9).

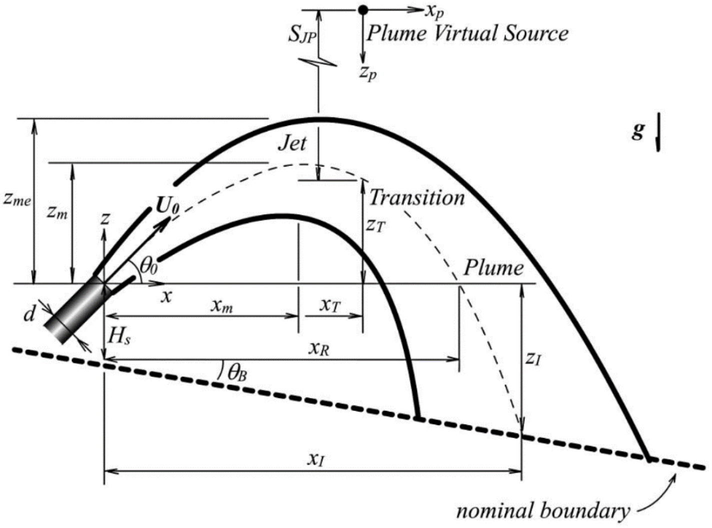

Figure 2.9 Schematic diagram of a negatively buoyant discharge on the nominal slope boundary (Figure from Oliver 2013a)

Coming back to Oliver's research, they gave detailed information for the return point and impact point. The location and the dilution at these points are demonstrated by a semi-analytical solution shown in Table 2.1.

Table 2.1 The dilution and location of the return point and impact point

| | **Return point** | **Impact point** |
|---|---|---|
| **Dilution** | $\frac{1}{F_0}\frac{C_0}{Cm} = K_{R_I}\frac{12^{1/3}}{1.61}\sqrt{k_t}K_{R\theta}^{5/3} = k_{RI}0.55K_{R\theta}^{5/3}$<br>$K_{R\theta} = 1 + \sin\theta_0\left\{1 - \frac{1}{tan^2\theta_0}\left[-1 + \frac{1}{2\sqrt{\sin\theta_0}}ln\left(\frac{1+\sqrt{\sin\theta_0}}{1-\sqrt{\sin\theta_0}}\right)\right]\right\}$ | $\frac{C_0}{c_t} = \left(12\frac{k_t^4}{F_0^2}\right)^{1/3}\left(\frac{z_p}{d}\right)^{5/3}$<br>$\frac{S_{JP}}{d} = \frac{F_0}{\sqrt{k_t}}$ |
| **Location** | $\frac{x_{R*}}{F_0} = \frac{1}{\sqrt{k_t}}\cos\theta_0\left\{\frac{1}{2\sqrt{\sin\theta_0}}ln\left(\frac{1+\sqrt{\sin\theta_0}}{1-\sqrt{\sin\theta_0}}\right) + 12^{1/3}\left[1 - \left(\frac{1}{K_{R\theta}}\right)^{1/3}\right]\right\}$ | $x_{p*} = 12^{1/3}S_{JP*}\cos\theta_0\left[1 - \frac{1}{\left(z_{p*}/S_{JP*}\right)^{1/3}}\right]$<br>$z_{I*} - H_{S*} = x_{I*}\tan\theta_B$<br>$x_{I*} = x_{p*} + x_{T*}$<br>$z_{p*} = S_{JP*} + z_{T*} + z_{I*}$ |

Oliver and his colleagues compared the results with the CorJet model. The simulation cannot be performed well by the integral model in the prediction of the location of these two points; They determined that CorJet underpredicted the dilution at these two points, but the semi-analytical solution shows a good fit with the experimental data. However, in the experimental study, there is no information of impact point on the real physical bottom. Therefore, more improvements should be developed in the future.

After the impact point, the jets are spreading on the bottom acting as gravity current. Few studies are carried out about the spreading layer on the horizontal bottom. Roberts *et al.*, (1997) first investigated that the characteristics of the spreading layer. Abessi *et al.*, (2015) investigated the inclined dense jets with inclination angles from 15° to 85° on a horizontal bottom, they found the dilution at the impact point was related to jet inclination smaller than 60°. They also found that the concentration is relatively increasing near the bed, the reason might be the accumulation of the fluid elements. The characteristics on the boundary layer should be addressed because it might lead to the high-risk exposure of seagrass in the salted environment.

## 2.5 CFD simulations

Computational fluid dynamics (CFD), is employed to solve fluid-flow problems with numerical solutions using computers. Computers with high speed and large storge space have enabled CFD to find solutions to many different flow problems, such as compressible or incompressible, laminar or turbulent flows and single or multi-phase flows.

The most fundamental approach in modeling turbulent jets is solving the Navier-Stokes equations; these are continuous equations that describe fluid flows. CFD simulations involve various methods such as Direct simulations (DNS), Large Eddy Simulation (LES) and Reynolds Averaged Navier Stokes (RANS). The LES and RANS methods are the most common types of turbulence models. The RANS model and its application will be detailed in Chapter 3.

CFD simulation of inclined dense jets has been performed by several authors. One study carried out CFD simulation of inclined dense jets with angles between 45 and 90° using a three-dimensional model – the Shear Stress Transport (SST) with ANSYS CFX software (Vafeiadou *et al*. 2005). Oliver *et al*. (2008) compared the standard $k - \varepsilon$ model with previous experimental results from other studies(Kikkert *et al*., 2007). Seil and Zhang (2010) used SST and Renormalization Group (RNG) model and employed the ANSYS FLUENT software to do the simulation of the single or multiple ports at discharge. The results were compared with previous experimental studies (Nemlioglu and Roberts, 2006) (Roberts *et al*., 1997).

Gildeh *et al*. (2015) study the performance of five different RANS turbulence models on inclined dense jets with three different discharge angles with the software OpenFOAM. The geometrical and mixing characteristics are studied and compared with one previous study (Shao and Law, 2010). They concluded that LRR and realizable $k - \varepsilon$ models had better performance. In 2016, they presented another numerical study on the geometry and characteristics of inclined dense jets with two discharge angles (30° and 45°) by two turbulence models- Launder-Reece-Rodi and Realizable $\mathrm{k} - \varepsilon$ (Kheirkhah Gildeh *et al*., 2016). The results were compared to the previous experimental data. They also investigated the effect of buoyancy on the production and dissipation of turbulent kinetic energy with a modified standard $\mathrm{k} - \varepsilon$ model using SGDH (standard Boussinesq gradient diffusion hypothesis)and GGDH(general gradient diffusion hypothesis) approaches. Applying the buoyancy term in the turbulence model improved the performance of models with respect to predicting the spread of dense jets.

Zhang *et al*. (2016) presented a detailed investigation of inclined dense jets with 45° inclined angle using a large eddy simulation (LES) approach with both the Smagorinsky and Dynamic Smagorinsky sub-grid scale (SGS) models. The results showed that LES could predict satisfactory geometric information in most aspects while the dilution is underestimated; the reason might be the inaccuracy of the SGS models for such applications. After one year, these authors carried out another LES simulation on inclined dense jets with two different discharge angle of 45° and 60°(Zhang *et al.*, 2017). The same conclusion was drawn: that the LES model reasonably predicts the jets' trajectories, but the impact dilution was underestimated by ~20%, and this might correspond to the mesh quanlity and grid resolution. In this research, the author also found that the LES model can clearly present that localized concentration build-up at the impact point, while RANS models are not able to do so. The accurate simulation of the mixing behavior of jet and wall interaction process is still challenging.

Ardalan and Vafaei (2019) carried out similar numerical modeling research on inclined dense jets using the realizable $k-\varepsilon$ turbulence model. The previous experimental results were used to evaluate the model's results(Ardalan and Vafaei, 2018). The result showed that the geometrical characteristics collected from the numerical and physical models were in good agreement.

# Chapter 3 Numerical Models

## 3.1 Introduction

Experimental investigations, theoretical modeling, and fieldworks are three main methods to study the fluid flow process. Much reliable physical information can be obtained from experiments; however, it is impractical and quite expensive to set up a full-scale experimental investigation. Although some scaled models are employed in fluid flow studies, experimental and scaling errors cannot be ignored, especially in the turbulent flow, due to irregular and chaotic changes that make these scaled models inaccurate. Simulations of physical processes can be performed based on mathematical models, and with the assistance of advanced computers, researchers can simulate realistic conditions and obtain detailed information which coupled with lab or field data, can provide useful information.

The flow movement can be described by conservation laws. It is possible to numerically solve a set of partial differential equations with boundary and initial conditions. In order to solve these equations, it is necessary to carry out a discretization method. There are various methods of discretization, which are classified into mesh (grid) methods and mesh-free methods; the former is widely adopted. It is necessary to point out two steps in mesh methods: 1) dividing the region into smaller regions; 2) adopting discretization of governing equations over the mesh or numerical grid.

Three important discretization methods are widely used nowadays: Finite Difference Method (FDM), Finite Volume Method (FVM) and Finite Element Method (FEM) (Peiró *et al.*, 2005). In mathematics, Finite Difference Method (FDM) is based upon the differential form of governing equations. Finite Volume Method (FVM) is based upon an integral form of governing equations, and is written in a form that can be solved in a given volume or cell; it is more efficient in solving fluid flow problems. Finite Element Method (FEM) is based on a piecewise representation of a solution in a specified basis function. It typically provides a continuous solution, and it calculates the flow properties in every node. FVM and FEM are efficient for all geometries including ones with complicated shapes and features.

Some important criteria should be considered such as consistency, stability, convergence, conservation, boundedness, realizability and accuracy (Kheirkhah Gildeh, 2013).

## 3.2 Governing equations

In fluid dynamics, the most commonly used governing equations are known as Navier- Stokes equations, which were discovered over 150 years ago (Jamshed, 2015). In hydraulic applications, fundamental principles that are used deal with the conservation of mass, momentum and energy.

*Conservation of mass*

The first law states that mass must be conserved, which is known as a continuity equation, that is, the mass of a system remains constant, and it cannot be created or destroyed. That means, for a control volume, the rate of increase of mass is equal to the net influx of mass $\frac{dm}{dt} = 0$(Figure 3.1).

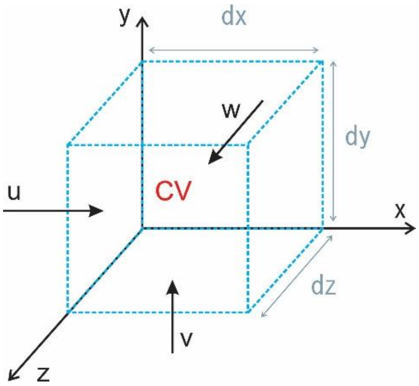

Figure 3.1 The element of fluid control volume

This can be written in differential form.

$$\left\{\frac{\partial(\rho u)}{\partial x} + \frac{\partial(\rho v)}{\partial y} + \frac{\partial(\rho \omega)}{\partial z}\right\} dx\, dy\, dz = \frac{\partial(\rho u_j)}{\partial x_j} dx\, dy\, dz = -\frac{\partial(\rho\, dx\, dy\, dz)}{\partial t} \qquad (3.1)$$

In vector notation it is

$$\frac{\partial \rho}{\partial t} + \nabla \cdot (\rho u)\, du = 0 \qquad (3.2)$$

Where $u,v,w$ are the velocities in the x, y,z directions, respectively, $t$ is time and $\rho$ is the density of the fluid. In this study, we are considering incompressible fluid, so the equation can be reduced to

$$\frac{\partial u}{\partial x}+\frac{\partial v}{\partial y}+\frac{\partial w}{\partial z}=\frac{\partial u_j}{\partial x_j}=0 \tag{3.3}$$

*Momentum equation*

The conservation of momentum is developed based on Newton's second Law, which is

$$F=ma=\frac{d}{dt}(mV) \tag{3.4}$$

In fluid dynamics, the forces acting on a control volume include two types; one is the set of forces acting upon the fluid, which includes gravity, electromagnetic and so on; the other set of forces is acting on the surface of the fluid, such as pressure and shear stress. Based on these, an equation for the forces acting on the control volume can be written as:

$$F=\oiiint_{v}\ \rho f dV-\oiint_{s}\ pdS+F_{viscous} \tag{3.5}$$

where $f$ represents the body force, and $p$ represents the pressure on the fluid surface and $F_{viscous}$ is the viscous force.

The equation for a three-dimensional system can be written as:

x-direction :

$$\frac{\partial(\rho u_x)}{\partial t}+\left(\frac{\partial\rho u_x u_x}{\partial x}\right)+\left(\frac{\partial\rho u_y u_x}{\partial y}\right)+\left(\frac{\partial\rho u_z u_x}{\partial z}\right)=\left(\frac{\partial\tau_{x,x}}{\partial x}\right)+\left(\frac{\partial\tau_{x,y}}{\partial y}\right)+\left(\frac{\partial\tau_{z,x}}{\partial z}\right)-\frac{\partial P}{\partial x} \tag{3.6}$$

y-direction :

$$\frac{\partial(\rho u_y)}{\partial t}+\left(\frac{\partial\rho u_x u_y}{\partial x}\right)+\left(\frac{\partial\rho u_y u_y}{\partial y}\right)+\left(\frac{\partial\rho u_z u_y}{\partial z}\right)=\left(\frac{\partial\tau_{x,y}}{\partial x}\right)+\left(\frac{\partial\tau_{y,y}}{\partial y}\right)+\left(\frac{\partial\tau_{z,y}}{\partial z}\right)-\frac{\partial P}{\partial y}-g \tag{3.7}$$

z-direction :

$$\frac{\partial(\rho u_z)}{\partial t}+\left(\frac{\partial\rho u_x u_z}{\partial x}\right)+\left(\frac{\partial\rho u_z u_y}{\partial y}\right)+\left(\frac{\partial\rho u_z u_z}{\partial z}\right)=\left(\frac{\partial\tau_{x,z}}{\partial x}\right)+\left(\frac{\partial\tau_{y,z}}{\partial y}\right)+\left(\frac{\partial\tau_{z,z}}{\partial z}\right)-\frac{\partial P}{\partial z} \tag{3.8}$$

Where $P$ is the fluid pressure and $g$ is the gravitational acceleration, and $\tau$ is the shear stress.

*Conservation of energy*

The third principle is the conservation of energy which is not used in the present study.

*Density equation*

The density equation is very important in this study because the density difference between a dense jet and receiving water is one of the key factors that control the Froude number, an important parameter for jet studies which controls the flow. The density can be calculated from an equation for the state of seawater as proposed by Millero and Poisson (1981).

$$\rho = \rho_t + AS + BS^{3/2} + CS \tag{3.9}$$

where

$$A = 8.24493 \times 10^{-1} - 4.0899 \times 10^{-3}T + 7.6438 \times 10^{-5}T^2 - 8.2467 \times 10^{-7}T^3 + 5.3875 \times 10^{-9}T^4$$

$$B = -5.72466 \times 10^{-3} + 1.0227 \times 10^{-4}T - 1.6546 \times 10^{-6}T^2$$

$$C = 4.8314 \times 10^{-4}$$

$\rho_t$ is the density of water, has the following relationship with temperature:

$$\rho_t = 999.842594 + 6.793952 \times 10^{-2}T - 9.095290 \times 10^{-3}T^2 + 1.001685 \times 10^{-4}T^3 - 1.120083 \times 10^{-6}T^4 + 6.536336 \times 10^{-9}T^5 \tag{3.10}$$

In this study, the temperature is assumed to be constant, S refers to the salinity in the water, which can be used to calculate the concentration.

### 3.3 Turbulence models

The numerical modeling of turbulent flows has been challenging for researchers and engineers because this process is very complicated. Many scientists and researchers have contributed to this field and tried to make improvements in the last two centuries.

One of the biggest challenges with turbulence modeling is its wide range of length and time scale.

Generally, there are three main methods for modeling turbulent flows: DNS (Direct Numerical simulation), RANS (Reynolds Averaged Navier-Stokes), and LES (Large Eddy Simulation) including their modified versions and variations. These three methods are shown in Figure 3.2 schematically (Anderson and Wendt, 1995). It is clear that some differences exist between these three main methods, and the DNS method can solve all turbulent flow problems. However, there are still many limitations and a limited range of applications for these methods.

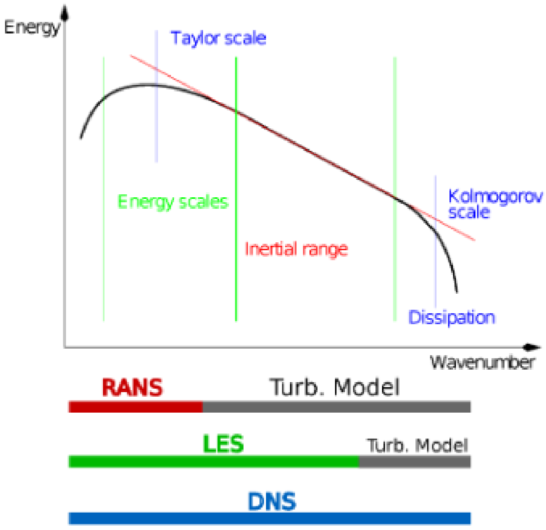

Figure 3.2 The application range of RANS, LES and DNS (From Anderson and Wendt, 1995)

### 3.3.1 Directed Numerical Simulation (DNS)

In DNS method, the Navier-Stokes equations are numerically solved for the entire range of spatial and temporal scales with flow variables of turbulence flow, however, in most real engineering cases, the flows cannot be computde directly due to the wide range of scales. DNS method doesn't require modeling, but it demands larage range of resolution including dissipation scales and large scales; meanwhile, this method is extremely costly, so it makes this method more suitable for scientific purposes rather than industrial fields. Orszag and Patterson Jr (1972) performed a computation of isotropic turbulent flow at a low Reynolds number of 35, and although the resolution is inadequate by today's standards, the calculation inspired much turbulent flow computing of three-dimensional homogeneous isotropic turbulence. Rogallo (1981) combined this with a transformation equation to compute homogeneous turbulence successfully. Some of these results are still being used to evaluate turbulence models nowadays.

### 3.3.2 Reynolds-averaged Navier-Stokes (RANS) Equations

The RANS method is currently the most computationally practical method/approach for turbulence modeling. It is essential to know the term "average," when a fluid is moving, no matter whether it is unconfined or confined, it always carries a certain amount of energy. It will dissipate some energy through friction or viscous effect. As discussed before, N-S equations can describe turbulence flow. Unfortunately, the solution of these non-linear equations for all length and time scales is truly an impossible task analytically and numerically. Even though there are supercomputers that can solve the turbulence equations, it is still costly and time-consuming (Lee *et al*., 2013). So Reynolds (1895) presented an idea that decomposed turbulent quantities into a mean and a fluctuation part; this solution is based on a fundamental 'assumption' that turbulence is a 'random' phenomenon. Therefore, quantities like velocity, pressure density and material concentration can be divided into relevant time-averaged values and their related turbulent fluctuation component, shown below:

Velocity: $u_i = \overline{u_i} + u_i'$ (3.11)

Pressure: $p_i = \overline{p_i} + p_i'$ (3.12)

Density: $\rho_i = \overline{\rho_i} + \rho_i'$ (3.13)

By introducing these equations with the N-S equation, and using the time-average of each term into the result of the N-S equation, the Reynolds Averaged Navier-Stokes (RANS) can be written as:

$$\frac{\partial \overline{u_i}}{\partial t} + \overline{u_j}\frac{\partial \overline{u_i}}{\partial x_j} = -\frac{\partial \bar{p}}{\partial x_i} + \nu\frac{\partial^2 \overline{u_i}}{\partial x_j \partial x_j} - \frac{\partial \overline{u_i' u_j'}}{\partial x_j} \tag{3.14}$$

$$\frac{\partial \overline{u_i}}{\partial x_i} = 0 \tag{3.15}$$

Comparing with the Navier- Stokes equations, a new set of terms is of form $\overline{u'w'}$ emerges on the right-hand side. The convective term is expressed in the non-conservative form, and $\overline{u_i' u_j'}$ is the Reynolds-stress. It is necessary to establish turbulence models to predict the Reynold-stress and find the closure of the mean flow system.

There are various RANS turbulence models concerning the number of transport equations such as zero-equation, one equation and two-equation models.

Many studies have been done on zero-equation models or algebraic models such as Mixing Length, Cebeci-Smith, etc., and one equation models such as Wolfstein, Baldwin-Barth, etc. (Spiegel, 1963) (Cebeci *et al*., 1972) (Wolfshtein, 1969) (Baldwin and Barth, 1991).

However, in this study, we will focus on two-equation models, the biggest advantage of the two-equation models is that they can meet the requirements for different flows simply and affordably.These advantages make two-equation models more common for most types of engineering problems. Nonetheless, RANS models still have some limitations (Schobeiri, 2010): (1) not be suitable for most turbulence-induced secondary flows; (2) swirling flows with rotations are also a shortcoming in most such models; and (3) RANS cannot perform well in some unsteady flows such as internal combustion engines and stagnant regions in flows.

### ***Two-Equation Models***

Standard $k-\varepsilon$ model, Realizable $k-\varepsilon$ model, RNG $k-\varepsilon$ model, $k-\omega$ model shear stress transport (STT) model, and the nonlinear $k-\varepsilon$ models are some of the two-equation models. The main difference between the two-equation model and other models (zero equation model or one equation model) is that two separate transport equations are solved for two independent turbulence length and time scales. Some common two-equation models are described below.

### ***Standard $k-\varepsilon$ models***

This model was first introduced by Chou (1945). The term “standard” refers to the calculation method of turbulent viscosity and the form of the equation for the turbulence dissipation rate (Van *et al.*, 2006).

This model contains the transport equation of kinetic energy k and the transport equation for dissipation $\varepsilon$. The length and time scales are established for these two aspects:

$$l_0 \propto \frac{k^{3/2}}{\varepsilon}, \tau_0 \propto \frac{k}{\varepsilon}. \tag{3.16}$$

It is neessary to use the dimensional analysis to obtain this empirical relationship. The equation used by Launder *et al.*, (1972) are: turbulent kinetic energy

$$\frac{\partial k}{\partial t} = \frac{1}{\rho}\frac{\partial}{\partial x_j}\left(\frac{\mu_t}{\sigma_k}\frac{\partial k}{\partial x_j}\right) + \frac{\mu_t}{\rho}\left(\frac{\partial \overline{V_i}}{\partial x_j} + \frac{\partial \overline{V_j}}{\partial x_i}\right)\frac{\partial \overline{V_i}}{\partial x_j} - \varepsilon \tag{3.17}$$

dissipation

$$\frac{\partial \varepsilon}{\partial t} = \frac{1}{\rho}\frac{\partial}{\partial x_j}\left(\frac{\mu_t}{\sigma_\varepsilon}\frac{\partial \varepsilon}{\partial x_j}\right) + C_{\varepsilon 1}\frac{\mu_t}{\rho}\frac{\varepsilon}{k}\left(\frac{\partial \overline{V_i}}{\partial x_j} + \frac{\partial \overline{V_j}}{\partial x_i}\right)\frac{\partial \overline{V_i}}{\partial x_j} - \frac{C_{\varepsilon 2}\varepsilon^2}{k} \tag{3.18}$$

the turbulent viscosity, $\mu_t$ can be writen as :

$$\mu_t = \rho C_\mu \frac{k^2}{\varepsilon} \tag{3.19}$$

The constants $\sigma_k, \sigma_\varepsilon, C_{\varepsilon 1}, C_{\varepsilon 2}$ are listed in Table 3.1, the calibration coefficients obtained from simple flow.

Table 3.1 Closure coefficients of $k-\varepsilon$ models

| $C_\mu$ | $\sigma_k$ | $\sigma_\varepsilon$ | $C_{\varepsilon 1}$ | $C_{\varepsilon 2}$ |
|---|---|---|---|---|
| 0.09 | 1 | 1.3 | 1.44 | 1.92 |

The $k-\varepsilon$ model can simulate various flow situations successfully. However, there is no perfect result for some turbulent flows where a major separation is involved, it meas this model lack of sensitivity to the adverse pressure gradient. Another main shortcoming of this model is that it can significantly over-predict the shear stress. This model also has some difficulties in obtaining the streamline rotational strains and the body-force efforts (Rodi and Scheuerer, 1986).

Although this model has many shortcomings and various limitations, it has a good variety of applications, and many scholars have achieved good simulations of turbulent flow based on it. Many studies have proposed improved variants of the standard $k-\varepsilon$ model, which have proven to be very useful and meaningful, both in academic and industrial applications. Davidson and Transfer (1990) presented a new turbulence model based on the development of the $k-\varepsilon$ models with algebraic Reynolds stress model, and this new concept can be applied to the flows with rotation and other cases. Liu and Wen (2002) compared a modified version of turbulence model and the low-Reynolds number model from Ince and Launder (1995) in buoyant diffusion flows; it turns out that the $k-\varepsilon$ model underpredicts the buoyancy-driven production of turbulent kinetic energy and other parameters of turbulent flows. Further turbulence models are discussed in the following.

### *Realizable $k-\varepsilon$ model*

The standard eddy viscosity formulation for incompressible turbulence is:

$$-\overline{u_i u_j} = -\frac{2}{3}k\delta_{ij} + v_T\left(U_{i,j} + U_{j,i}\right) \tag{3.20}$$

$$v_T = C_\mu \frac{k^2}{\varepsilon}$$

$$C_\mu = 0.09$$

To ensure realizability, the coefficient $C_\mu$ is not a constant, it is related to the mean strain rate. Many experiments have proven that under certain conditions in boundary layer and homogeneous shear flows, the values of $C_\mu$ can be quite different.

Shih *et al*. (1995) proposed a new $k-\varepsilon$ eddy viscosity model for high Reynolds number turbulent flows. A new approach for dissipation rate equation and a new realizable eddy viscosity formulation have been adopted, they did some calibration of the model’s coefficients.

The results are summarized in Table 3.2.

$$C_\mu = \frac{1}{A_0 + A_s U^{(*)} \frac{k}{\varepsilon}} \qquad (1)$$

$$C_1 = \max\left\{0.43, \frac{\eta}{\eta+5}\right\} \text{ where } \eta = \frac{S_k}{\varepsilon} \quad (2)$$

Table 3.2 Closure coefficients of Realizable $k - \varepsilon$ model

| $\sigma_k$ | $\sigma_\varepsilon$ | $C_1$ | $C_2$ | $C_\mu$ | $A_0$ |
|---|---|---|---|---|---|
| 1.0 | 1.2 | (2) | 1.9 | (1) | 4.0 |

Comparing the new turbulence model with the results from standard $k{-}\varepsilon$ models, DNS, LES and experiments on different types of flow, the results showed that the realizable $k{-}\varepsilon$ model was much better than the standard $k{-}\varepsilon$ model in almost all cases. More importantly, the new dissipation rate equation is expected to increase the numerical stability in turbulent flow calculations.

The most significant difference between the realizable $k{-}\varepsilon$ model and the standard one is that there are new formulation for turbulent viscosity and new transport equation for the dissipation rate in realizable $k{-}\varepsilon$ model. However, it has an important limitation: non-physical turbulent viscosities will be produced when the flow contains rotating. Thus, caution should be taken when applying this model to such flow systems.

### *RNG $k{-}\varepsilon$ model*

RNG (Renormalization Group) theory has been used to derive the $k{-}\varepsilon$ constants, which improves the ability of the $k{-}\varepsilon$ family of models by using dynamic scaling, invariance and iterated perturbation methods (Yakhot and Smith 1992). It attempts to formulate a universal law of the small scales in N-S equations, by using some equations that incorporate a Gaussian random force, and supposes that this equation describes small-scale properties of turbulent flow in the inertial range.

RNG is similar in form to the standard $k{-}\varepsilon$ models, but with an additional term $C_{\varepsilon 2}^{*}$ in the $\varepsilon$ equation. The constants of this model are calculated explicitly from the standard k-e model. They are listed in Table 3.3.

$$\frac{\partial \varepsilon}{\partial t} = \frac{1}{\rho}\frac{\partial}{\partial x_j}\left(\frac{\mu_t}{\sigma_\varepsilon}\frac{\partial \varepsilon}{\partial x_j}\right) + C_{\varepsilon 1}\frac{\mu_t}{\rho}\frac{\varepsilon}{k}\left(\frac{\partial \bar{V}_i}{\partial x_j} + \frac{\partial \bar{V}_j}{\partial x_i}\right)\frac{\partial \bar{V}_i}{\partial x_j} - \frac{C_{\varepsilon 2}^{*}\varepsilon^2}{k} \qquad (3.21)$$

$$C_{\varepsilon 2}^{*} = C_{\varepsilon 2} + \frac{C_\mu \eta^3 (1-\eta/\eta_0)}{1+\beta\eta^3} \tag{3.22}$$

$$\eta = Sk/\varepsilon \tag{3.23}$$

$$S = 2(S_{ij}S_{ij})^{1/2} \tag{3.24}$$

where S is the modulus of the mean rate-of-strain tensor, the turbulent viscosity can be calculated in the same way as the standard $k$−$\varepsilon$ model (Wilcox,1998).

Table 3.3 Closure coefficients of RNG $k-\varepsilon$ model

| $C_\mu$ | $\sigma_k$ | $\sigma_\varepsilon$ | $C_{\varepsilon 1}$ | $C_{\varepsilon 2}$ | $\eta_0$ | $\beta$ |
|---|---|---|---|---|---|---|
| 0.0837 | 0.7179 | 0.7179 | 1.063 | 1.7215 | 4.38 | 0.012 |

RNG also provides a formula for viscosity with the low-Reynolds number effects. This model significantly improves the accuracy of the strained flows; it also enhances the accuracy for swirling flows. The accuracy of this model highly depends on the treatment of the near-wall region.

### *Two equation k-ω model*

This model was first proposed by Kolmogorov (1942). It is different from the k- $\varepsilon$ equation in the transport terms. Here, the $\varepsilon$ equation is replaced with the $\omega$ transport equation, which includes the solution of transport equations for the turbulent kinetic energy and $\omega$. It combines the physical reasoning with dimensional analysis. In his research, Kolmogorov postulates the following transport equations.

$$\frac{\partial k}{\partial t} + U_j \frac{\partial k}{\partial x_j} = \tau_{ij} \frac{\partial \overline{u_\iota}}{\partial x_j} - \beta^* k\omega + \frac{\partial}{\partial x_j}\left[(v + \sigma^* v_T)\frac{\partial k}{\partial x_j}\right] \tag{3.25}$$

$$\frac{\partial \omega}{\partial t} + \overline{u_\iota}\frac{\partial \omega}{\partial x_i} = -\gamma_1 \frac{\omega}{K}\tau_{ij}\frac{\partial \overline{u_\iota}}{\partial x_j} + \frac{\partial\left(\frac{v_T\,\partial\omega}{\sigma_\omega \partial x_i}\right)}{\partial x_i} - \gamma_2\omega^2 + \frac{\partial}{\partial x_j}\left[(v + \sigma v_T)\frac{\partial \omega}{\partial x_j}\right] \tag{3.26}$$

$$v_T = \frac{k}{\omega} \tag{3.27}$$

k-ω model has undergone several changes and many researchers are trying to add additional terms. Wilcox (2008) developed one which is commonly used. The coefficients are shown in Table 3.4.

Table 3.4 Closure coefficients of the $k-\omega$ model

| $\gamma_1$ | $\gamma_2$ | $\beta^*$ | $\sigma$ | $\sigma^*$ |
|---|---|---|---|---|
| $-\frac{5}{9}$ | $\frac{3}{40}$ | 0.09 | 0.5 | 0.5 |

Comparing the results from $k{-}\varepsilon$ model with the flow adverse pressure gradient condtion, the k-$\omega$ model performs significantly better, and this model has the advantage on the viscous sub-layer due to the simplicity of its formulations. Besides, this model has significant advantages in numerical stability because it has straightforward Dirichlet boundary conditions rather than damping functions (Menter, 1993). In the near wall layers, the k-$\omega$ model is also much more accurate than $k{-}\varepsilon$ model.

However, a main disadvantage of the k-$\omega$ model is that it strongly depends on the free-stream values (Wilcox, 1991). Some researchers have investigated this problem and demonstrated that the model does not correctly predict the asymptotic behavior of the turbulence when it approaches the wall.

### *The SST k-ω model*

The $k{-}\varepsilon$ model and k-$\omega$ model fail for flows with pressure-induced separation. With the need for accurate prediction of aeronautical flows with adverse pressure gradients and separations, considering the strength and the shortcoming of the $k{-}\varepsilon$ model and k-$\omega$ model, Menter *et al*. (1994) were motivated to develop other models such as SST k-ω models.

SST refers to Shear-Stress Transport, and this model was originally used for aeronautical applications. It is a “hybridized” model that combines the strength and superior behavior of the k-$\varepsilon$ and k-$\omega$ models. The k-$\varepsilon$ model prediction is more reasonable for flow regions away from the wall, and is insensitive to the initial parameters of the main free stream flow, whereas k-$\omega$ behaves much better close to the wall. Therefore, it seems quite useful to combine the advantages of these two models. Menter *et al*., (1994) modified the k-$\omega$ model to consider the transport effects of the turbulent shear stress. The SST model uses k-$\varepsilon$ formulation along the wall from the inside of the bournday layer to the viscous sublayer. It can avoid the common problem in the k-$\omega$ model of being too sensitive to the turbulence free-stream boundary conditions and turbulence properties because it switches to a k-$\varepsilon$ model in the free stream.

### *The nonlinear $k{-}\varepsilon$ model*

It is very challenging to find universal equations for many industrial and engineering applications. Therefore, an accurate numerical solution of the nonlinear equations has become a valuable tool, and it can be used to validate the theoretical models.. . As mentioned before, the standard $k{-}\varepsilon$ model follows the Boussinesq hypothesis in the definition of the stress-strain relation, the $k{-}\varepsilon$ and k-$\omega$ models can not perform well in some cases such as large adverse pressure gradients (Yin *et al*., 2013). Ehrhard (1999) proposed that nonlinear methods can predict the Reynold stresses with reasonable accuracy. Therefore, a new model, the nonlinear k- $\varepsilon$ turbulence model, can be modified from the RNG $k{-}\varepsilon$ turbulence model and the k-$\omega$ turbulence model.

The non-linear $k{-}\varepsilon$ model combines the advantage of Wilcox's k-$\omega$ model for the prediction of the near-wall region and the $k{-}\varepsilon$ model for the main streamflow. The accuracy of nonliner $k{-}\varepsilon$ turbulence model was improved by combining the nonlinear solution for Reynolds stress which is achieved through the turbulence velocity scale and turbulence time scale. The results for the nonlinear solution satisfy the principles of realizability and frame invariance. Liu *et al*., (2014) used it to simulate the unsteady flow and predict the pressure fluctuations through a model pump turbine for engineering applications. The numerical results and experiments had good agreement.However, some experts found that there are some disadvantages to this model in some applications. Balabel and El-Askary (2011) found that nonlinear $k{-}\varepsilon$ turbulence model could not perform as well as as a linear turbulence model in prediction of simple jet flows(non-impinging). But it is suitable to predict the turbulent viscosity structure such as the near-wall region with inhomogeneous flow and the anisotropic Reynolds stresses.

### *LRR (Launder, Reece and Rodi Model)*

The Launder-Reece-Rodi Model is one of the Reyolds Stress Turbulence models. This model has a main transport equation for Reynolds stress based on subtracting the averaged momentum equation from the instantaneous one (Launder *et al*., 1975)

$$\frac{D\overline{u_\iota u_J}}{Dt} = \frac{\partial \overline{u_\iota' u_J'}}{\partial t} + \overline{u_k}\frac{\partial \overline{u_\iota' u_J'}}{\partial x_k} = D_{ij}^{\nu} + D_{ij}^{T} + \phi_{ij} + P_{ij} + \varepsilon_{ij} \tag{3.28}$$

$D_{ij}$ is the diffusion term, $P_{ij}$ is the production term, $\phi_{ij}$ is the pressure strain rate correlation term, and $\varepsilon_{ij}$ is the turbulent dissipation rate term.

The viscous diffusion term is calculated by

$$D_{ij}^{\nu} = \nu \frac{\partial^2 \overline{u_i' u_j'}}{\partial x_k x_k} \tag{3.29}$$

The turbulent diffusion term is calculated by

$$D_{ij}^{T} = \frac{\partial}{\partial x_l}\left(C_s \frac{\varepsilon}{k} \overline{u_l u_k} \frac{\partial \overline{u_l u_j}}{\partial x_k}\right) \tag{3.30}$$

Where $C_s$= 0.22

The production term can be calculated by

$$P_{ij} = -\overline{u_i' u_k'} \frac{\partial \overline{u_j}}{\partial x_k} - \overline{u_j' u_k'} \frac{\partial \overline{u_i}}{\partial x_k} \tag{3.31}$$

The dissipation term is calculated by

$$\varepsilon_{ij} = -2\nu \overline{\frac{\partial u_i'}{\partial x_k} \frac{\partial u_j'}{\partial x_k}} \tag{3.32}$$

$$\frac{\partial \varepsilon}{\partial t} + \overline{u_k} \frac{\partial \varepsilon}{\partial x_k} = C_{\varepsilon 1} \frac{P_k \varepsilon}{k} - C_{\varepsilon 2} \frac{\varepsilon^2}{k} + \frac{\partial}{\partial x_j}\left(C_\varepsilon \frac{k}{\varepsilon} \overline{u_i' u_j'} \frac{\partial \varepsilon}{\partial x_j}\right) \tag{3.33}$$

where $C_{\varepsilon 1}$=1.44 , $C_{\varepsilon 2}$=1.90

This model is more accurate than two-equation models in most cases because it directly calculates Reynolds stresses.

### 3.3.3 Large-eddy Simulation (LES)

Since there are some failures of the RANS method, engineers are considering other methods and techniques in turbulence models. Large-eddy Simulation (LES) is one of them. It was proposed by Smagorinsky (1963) and Deardorff (1970). LES is a turbulence computation method between RANS and DNS. There are some differences among these models; DNS does not require modeling, and RNAS approaches require extensive modeling.

The main idea of LES is to simulate directly the inertial subrange in stead of all the range including dissipation scales in DNS method. LES only needs to represent the high-wavenumber part of the inertial sub-range.

When using LES, the spatially averaging methods are applied to defince the velocity, pressure velocity for the large flow structures. One common way to do this is by defining this spatial average by convolving these quantities with an appropriate filter function. In LES, only the large turbulent eddies are accurately resolved, while those smaller than the grid size are modeled. Small-scale structures are believed to be homogenous and possess a universal character. LES can improve the performance of results compared to the RANS method, and the application of it in the prediction of turbulent flows in many configurations is increasing, primarily in internal flows or for those flows that include more than one phase.

Since LES ignores the smallest length scales, it does not perform well in some flows where small scales play an important role such as near-wall flows and multiphase flows (Piomelli and Balaras, 2002) (Fox, 2012). Also, the high cost of LES limits the use of this method (Krishnan, 2008).

## 3.4 Introduction of CFD and OpenFOAM

Computational fluid dynamics, or simply CFD, is considered a good way to solve fluid-flow problems with numerical solutions by using computers. High-speed and large-memory computers have enabled CFD to find solutions to many different flow problems, including compressible or incompressible, laminar or turbulent flows, single- or multi-phase flows.

However, there are some constraints regarding these CFD methods. The first is that computers can only perform arithmetic and logic. This means that non-arithmetic operations must be represented by arithmetic and logic operations. The second constraint is that computers represent numbers using a finite number of digits; that means errors still exist; however, in order to get the most precise results, these errors must be controlled. The third constraint involves the computer itself; it has limited storage memory and operating speed. Larger memory capacities and more advanced processors signify higher economic costs.

Even so, Computational Fluid Dynamics (CFD) still has plenty of advantages such as flexibility, accuracy, and breadth of applications. It becomes more and more critical with the increase in the power of computers.

There are three steps for generating solutions in CFD: (1) Discretize the domain; (2) Discretize the PDE (partial differential equations); (3) Specify the algorithm. As mentioned, the approximate numerical solution for fluid flow can be obtained through discretization. Based on these methods, many different software and codes are used to address the numerical simulations. These include ANSYS CFD, OpenFOAM, SU2 code, etc. OpenFOAM is regarded as a useful tool to do the numerical modeling and simulation in this study.

### 3.4.1 OpenFOAM

OpenFOAM is a CFD software package of free, open source libraries under the general public license produced by OpenCFD Ltd. and a commercial version was initially released in 2004.

This software is widely used in both academic research and industrial applications. Recently, it has been further developed and used by many researchers (Greenshields, 2017).

OpenFOAM, with a wide range of fuctions, is able to solve complex fluid flows involving chemical reactions, turbulence and heat transfer. These features have been developed under object-oriented C++ language in the construction of programming, virtual constructors and run-time selection. It is an open-source software, which means it can also allow users to construct new models and solvers without changing the main source code. There are two categories for the 250 prebuilt applications in OpenFOAM, all the solvers are designed to solve a specific problem in fluid mechanics. It is easy for users to extend the solvers and utilities and libraries in OpenFOAM.

This software is based on FVM (Finite Volume Method) to discretize and solve dynamic problems. It first creates a three-dimensional volume and divides it into small volumes or meshes. After this, OpenFOAM creates the initial and boundary condition to solve the conservation equations that are defined and applied to the geometry. Then it solves the modeling equations using built mesh. Figure 3.3 shows the overall structure of OpenFOAM (Greenshields, 2017).

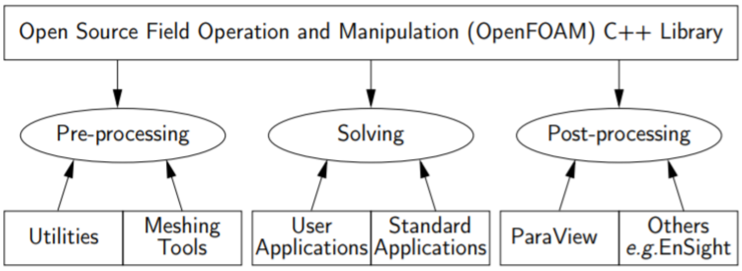

Figure 3.3 OpenFOAM overall structure

Figure 3.4 shows the basic content of one OpenFOAM case. It usually has three parts: system folder, constant folder and 0 folder (zero folder).

- System folder: defines the parameters related to the solution procedure such as *controlDict* to set up time step, writing step, and simulation time, etc. ; the *fvschemes* to change the discretization schemes used in the solution; *fvsolution* to choose the solvers tolerances and other algorithm controls that are set for the simulation.
- Constant folder: *blockMeshDict* controls mesh characteristics, *transproperties* can adjust the turbulence models and material properties for each different case

- 0 folder: determine the initial conditions of the flow fields, including kinetic energy *k*, dissipation ε, velocity, density, pressure, temperature, etc.

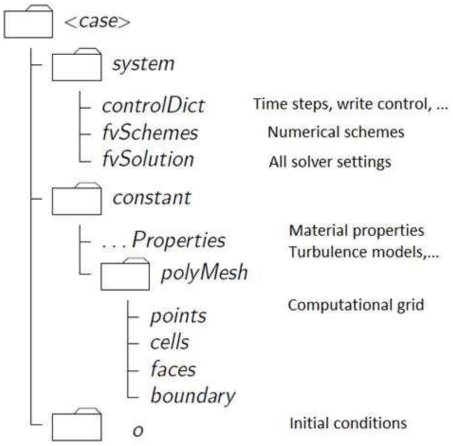

Figure 3.4 Basic content in one OpenFOAM case

### 3.4.2 Improved PisoFoam solver - pisoFoam5

In this study, the employed solver is named pisoFoam5, which is modified based on the pisoFoam solver within OpenFOAM as described in the following. The PisoFoam solver is a transient solver for incompressible flows, using the PISO algorithm (Pressure Implicit with Splitting of Operators) (Issa *et al*., 1986).

As mentioned, the incompressible continuity and momentum equations are:

$$\nabla \cdot \boldsymbol{u} = 0 \tag{3.34}$$

$$\frac{\partial \boldsymbol{u}}{\partial x} + \nabla \cdot (\boldsymbol{u}\boldsymbol{u}) - \nabla \cdot (v \nabla \boldsymbol{u}) = -\nabla p \tag{3.35}$$

There is no pressure equation for incompressible flow, so it is necessary to derive one using continuity and momentum equations, and the continuity equation has a restriction on the computed field. The non-linearity in the convection term ($\nabla \cdot (\boldsymbol{u}\boldsymbol{u})$ is dealt with using an iterative solution technique,

$$\nabla \cdot (\boldsymbol{u}\boldsymbol{u}) \approx \nabla \cdot (\boldsymbol{u}^0 \boldsymbol{u}^n) \tag{3.36}$$

Where $\boldsymbol{u}^0$ is the currently available solution, $\boldsymbol{u}^n$ is for the new solution, and the algorithm cycles will end when $\boldsymbol{u}^0 = \boldsymbol{u}^n$.

The main ideas of PISO are as follows:

- pressure-velocity system contains two complex coupling terms:

Non-linear convection term, containing u-u coupling

Linear pressure-velocity coupling

- For a small time-step (small Courant numbers), the pressure-velocity coupling is much stronger than the non-linear coupling, for each time step, and it can capture the fluctuations associated with turbulence;
- Repeat the pressure correctors without updating calculation of the momentum equation;
- The pressure corrector will create a conservative velocity field in the first steep, then the second and following steps will continue establishing the pressure distribution.

Figure 3.5 shows the PISO algorithm flow procedure.

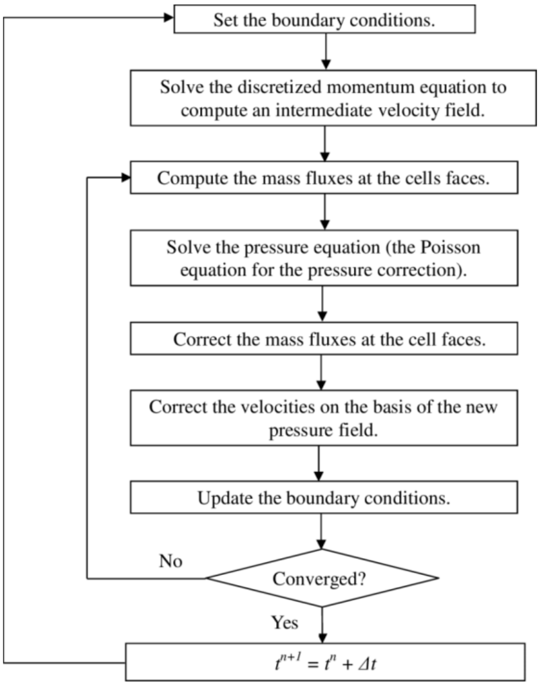

Figure 3.5 PISO algorithm loop flow

Let us take a look inside of the code of the pisoFoam solver in OpenFOAM.

The conservative fluxes, *phi*, derived from the last time step is used to discretize the momentum equation. It should be mentioned that *phi* represents the “old “velocity, or $\boldsymbol{u}^0$ in the convective term.

```
fvVectorMatrix UEqn
(
    fvm::ddt(U)
  + fvm::div(phi, U)
  - fvm::laplacian(nu, U)
);
```

Then the pressure from the previous step is used to solve the momentum equations, this is the step for the momentum predictor.

```
solve(UEqn == -fvc::grad(p));
```

The pressure-corrector step is then looped with fixed times (*nCorr*), then the next pressure-corrector step is performed.

The PISO loop in OpenFOAM is shown below.

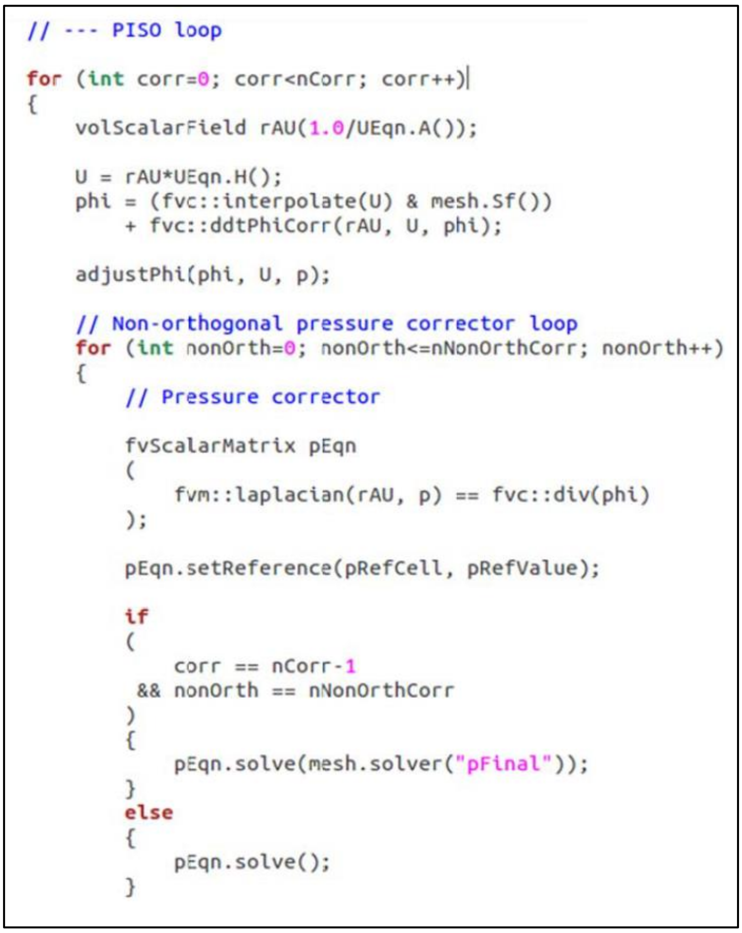

```
// --- PISO loop

for (int corr=0; corr<nCorr; corr++)
{
    volScalarField rAU(1.0/UEqn.A());

    U = rAU*UEqn.H();
    phi = (fvc::interpolate(U) & mesh.Sf())
        + fvc::ddtPhiCorr(rAU, U, phi);

    adjustPhi(phi, U, p);

    // Non-orthogonal pressure corrector loop
    for (int nonOrth=0; nonOrth<=nNonOrthCorr; nonOrth++)
    {
        // Pressure corrector

        fvScalarMatrix pEqn
        (
            fvm::laplacian(rAU, p) == fvc::div(phi)
        );

        pEqn.setReference(pRefCell, pRefValue);

        if
        (
            corr == nCorr-1
         && nonOrth == nNonOrthCorr
        )
        {
            pEqn.solve(mesh.solver("pFinal"));
        }
        else
        {
            pEqn.solve();
        }
```

The modified *PisoFoam5* is used in this thesis to solve the concentration during the simulation, in which the concentration equation was added in the pisoFoam solver.

Firstly, we added the concentration fields in to the *creatFields.H*, which is one of the directories in the *pisoFoam solver* folder.

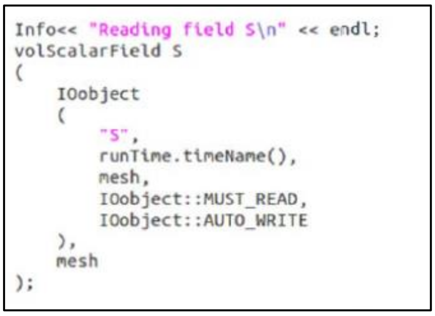

```
Info<< "Reading field S\n" << endl;
volScalarField S
(
    IOobject
    (
        "S",
        runTime.timeName(),
        mesh,
        IOobject::MUST_READ,
        IOobject::AUTO_WRITE
    ),
    mesh
);
```

Then concentration equations are added in another directory - *pisoFoam.C.* as shown below.

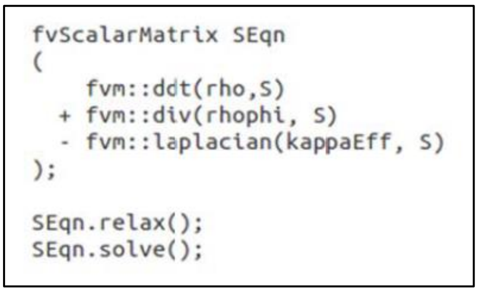

```
fvScalarMatrix SEqn
(
    fvm::ddt(rho,S)
  + fvm::div(rhophi, S)
  - fvm::laplacian(kappaEff, S)
);

SEqn.relax();
SEqn.solve();
```

### 3.4.3 Preparation of the case file

As mentioned, there are three folders in one basic OpenFOAM case, including 0 folder, *system* and *constant*. This part presents the details of each folder.

***Constant directory***

After OpenFOAM version 5, the *blockMeshDict* was moved into the *system* folder, while it connected with the mesh setup. The author still introduces this in the *constant* folder. With the *blockMeshDict*, the mesh can be set up easily. The domain was divided into several blocks; for each block, there are eight vertices, and all the boundary conditions as a patch or wall will be defined in this dictionary as well.

Here is an example of coarse mesh for the present case.

*BlockMeshDict*

```
vertices
(
        (0 0 0)//0
        (120 -14.5 0)//1
        (0 1.117 0)//2
        (120 -13.383 0)//3
        (0 2.069 0)//4
        (120 -12.431  0)//5
        (0 50 0)//6
        (120 50 0)//7
        (0 0 19.524)//8
        (120 -14.5 19.524)//9
        (0 1.117 19.524)//10
        (120 -13.383  19.524)//11
        (0 2.069  19.524)//12
        (120 -12.431  19.524)//13
        (0 50  19.524)//14
        (120 50  19.524)//15
        (0 0 20)//16
        (120  -14.5 20)//17
        (0 1.117 20)//18
        (120  -13.383 20)//19
        (0 2.069 20)//20
        (120 -12.431 20)//21
        (0 50 20)//22
        (120 50 20)//23
);

blocks
(
    hex (0 1 3 2 8 9 11 10) (80 2 20) simpleGrading (6.67 0.81 0.1)//0
    hex (8 9 11 10 16 17 19 18) (80 2 1) simpleGrading (6.67 0.81 1)//1
    hex (2 3 5 4 10 11 13 12) (80 2 20) simpleGrading (6.67 1 0.1)//2
    hex (10 11 13 12 18 19 21 20) (80 2 1) simpleGrading (6.67 1 1)//3
    hex (4 5 7 6 12 13 15 14) (80 30 20) simpleGrading (6.67 7.3 0.1)//4
    hex (12 13 15 14 20 21 23 22) (80 30 1) simpleGrading (6.67 7.3 1)//5
);
```

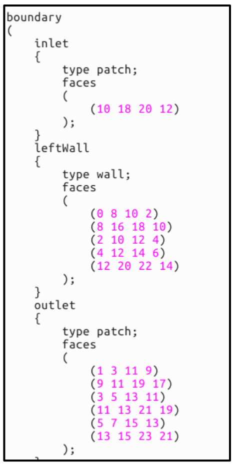

```
boundary
(
    inlet
    {
        type patch;
        faces
        (
            (10 18 20 12)
        );
    }
    leftWall
    {
        type wall;
        faces
        (
            (0 8 10 2)
            (8 16 18 10)
            (2 10 12 4)
            (4 12 14 6)
            (12 20 22 14)
        );
    }
    outlet
    {
        type patch;
        faces
        (
            (1 3 11 9)
            (9 11 19 17)
            (3 5 13 11)
            (11 13 21 19)
            (5 7 15 13)
            (13 15 23 21)
        );
```

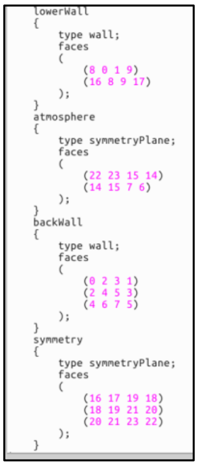

```
    lowerWall
    {
        type wall;
        faces
        (
            (8 0 1 9)
            (16 8 9 17)
        );
    }
    atmosphere
    {
        type symmetryPlane;
        faces
        (
            (22 23 15 14)
            (14 15 7 6)
        );
    }
    backWall
    {
        type wall;
        faces
        (
            (0 2 3 1)
            (2 4 5 3)
            (4 6 7 5)
        );
    }
    symmetry
    {
        type symmetryPlane;
        faces
        (
            (16 17 19 18)
            (18 19 21 20)
            (20 21 23 22)
        );
    }
```

And the *transproperties* dictionary includes the transport models (Newtonian) viscosity and density for the fluids.

*transproperties dictionary*

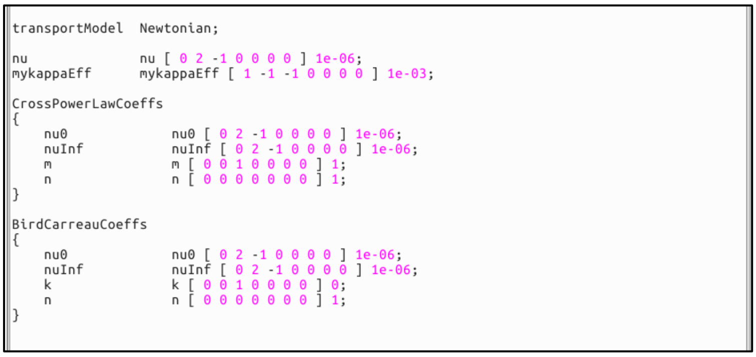

```
transportModel  Newtonian;

nu              nu [ 0 2 -1 0 0 0 0 ] 1e-06;
mykappaEff      mykappaEff [ 1 -1 -1 0 0 0 0 ] 1e-03;

CrossPowerLawCoeffs
{
    nu0             nu0 [ 0 2 -1 0 0 0 0 ] 1e-06;
    nuInf           nuInf [ 0 2 -1 0 0 0 0 ] 1e-06;
    m               m [ 0 0 1 0 0 0 0 ] 1;
    n               n [ 0 0 0 0 0 0 0 ] 1;
}

BirdCarreauCoeffs
{
    nu0             nu0 [ 0 2 -1 0 0 0 0 ] 1e-06;
    nuInf           nuInf [ 0 2 -1 0 0 0 0 ] 1e-06;
    k               k [ 0 0 1 0 0 0 0 ] 0;
    n               n [ 0 0 0 0 0 0 0 ] 1;
}
```

The *turbulenceProperties* can control the turbulence models that were introduced before such as (RANS or LES); OpenFOAM has plenty of turbulence models. In this case, the details are shown below:

*turbulenceProperties*

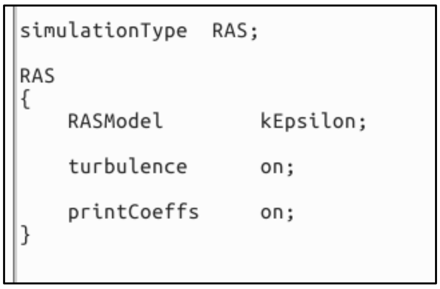

```
simulationType  RAS;

RAS
{
    RASModel        kEpsilon;

    turbulence      on;

    printCoeffs     on;
}
```

### *System directory*

There are three directories in the system folders. *controDict*, *fvscheme*, and *fvsolutions*, with details shown below:

*controDict file*

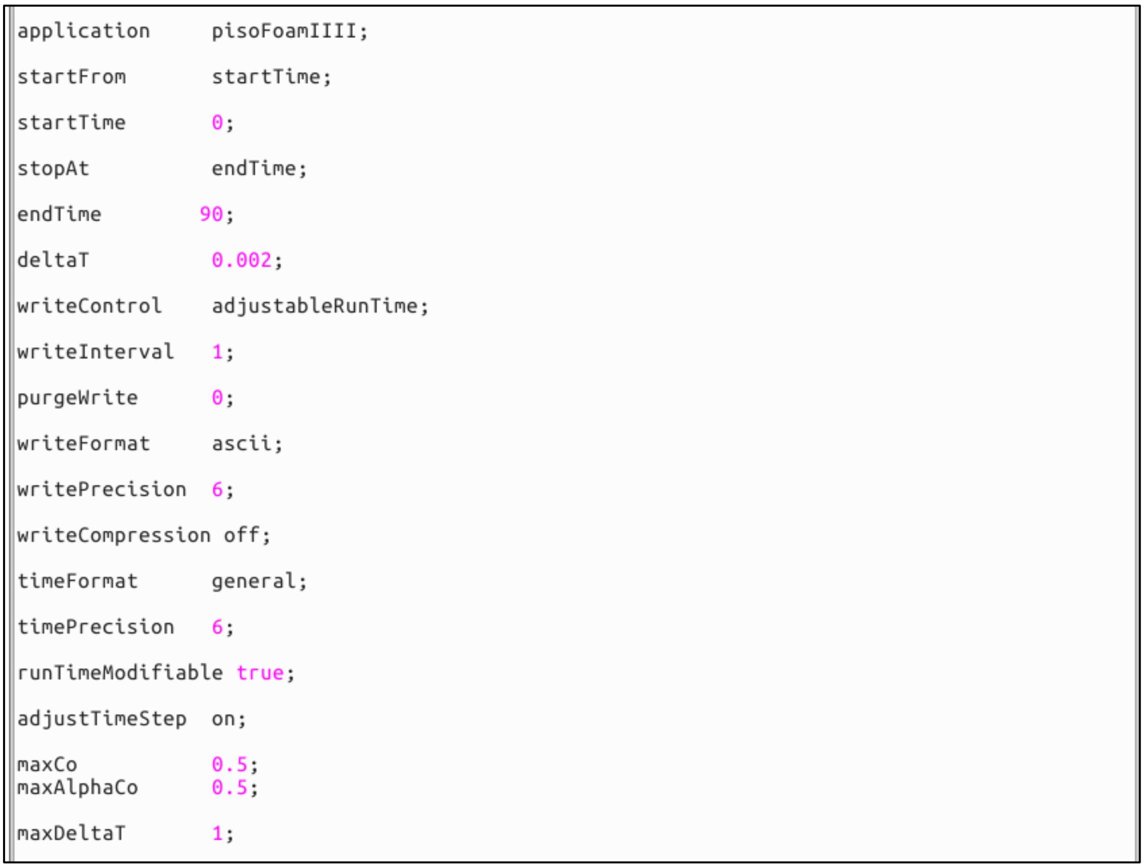

```
application     pisoFoamIIII;

startFrom       startTime;

startTime       0;

stopAt          endTime;

endTime        90;

deltaT          0.002;

writeControl    adjustableRunTime;

writeInterval   1;

purgeWrite      0;

writeFormat     ascii;

writePrecision  6;

writeCompression off;

timeFormat      general;

timePrecision   6;

runTimeModifiable true;

adjustTimeStep  on;

maxCo           0.5;
maxAlphaCo      0.5;

maxDeltaT       1;
```

*fvScheme file*

```
gradSchemes
{
    default         Gauss linear;
}

divSchemes
{
      default         none;
    div(phi,U)      Gauss linearUpwind Grad(U);
    div(phi,omega)  Gauss upwind;
    div(phi,epsilon)  Gauss upwind;
    div(R)          Gauss upwind;
    div(phi,nuTilda)    Gauss upwind;
    div((nuEff*dev2(T(grad(U))))) Gauss linear;
    div(rhophi,T)      Gauss upwind;
    div(rhophi,S)      Gauss limitedLinear 1;
    div((nu*dev2(T(grad(U))))) Gauss linear ;
    div(rhoPhi,U)  Gauss linear;
    div(phi,alpha)  Gauss vanLeer;
    div(phi,k)      Gauss upwind;
    div(((rho*nuEff)*dev2(T(grad(U))))) Gauss linear;
}

laplacianSchemes
{
    //default         Gauss linear corrected;
    default         Gauss linear limited 0.5;
}

interpolationSchemes
{
    default         linear;
}
```

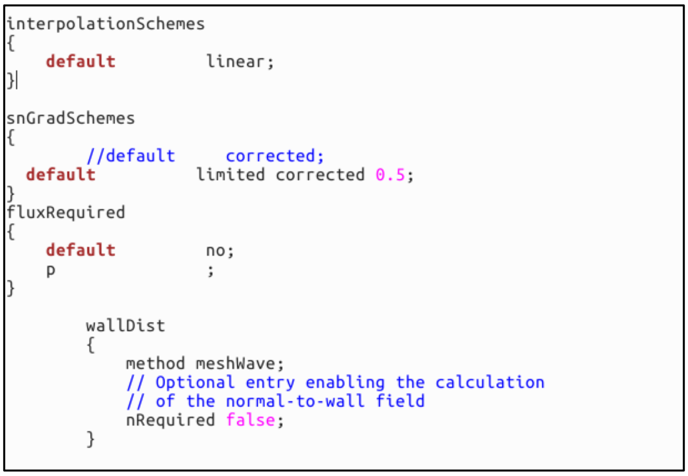

```
interpolationSchemes
{
    default         linear;
}

snGradSchemes
{
        //default      corrected;
  default           limited corrected 0.5;
}
fluxRequired
{
    default         no;
    p               ;
}

        wallDist
        {
            method meshWave;
            // Optional entry enabling the calculation
            // of the normal-to-wall field
            nRequired false;
        }
```

*fvSolutions file*

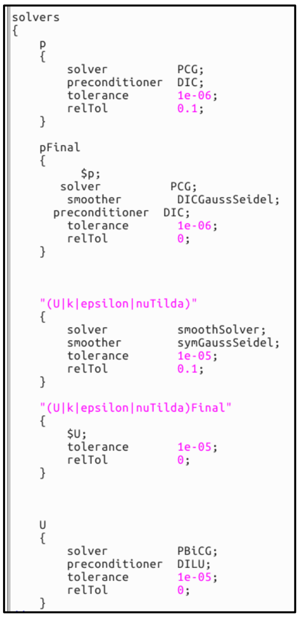

```
solvers
{
    p
    {
        solver          PCG;
        preconditioner  DIC;
        tolerance       1e-06;
        relTol          0.1;
    }

    pFinal
    {
          $p;
       solver          PCG;
        smoother        DICGaussSeidel;
      preconditioner  DIC;
        tolerance       1e-06;
        relTol          0;
    }


    "(U|k|epsilon|nuTilda)"
    {
        solver          smoothSolver;
        smoother        symGaussSeidel;
        tolerance       1e-05;
        relTol          0.1;
    }

    "(U|k|epsilon|nuTilda)Final"
    {
        $U;
        tolerance       1e-05;
        relTol          0;
    }



    U
    {
        solver          PBiCG;
        preconditioner  DILU;
        tolerance       1e-05;
        relTol          0;
    }
```

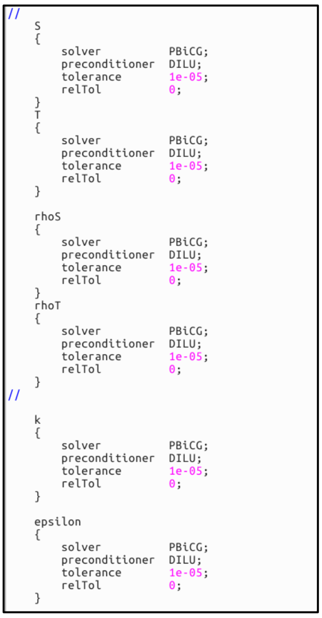

```
//
    S
    {
        solver          PBiCG;
        preconditioner  DILU;
        tolerance       1e-05;
        relTol          0;
    }
    T
    {
        solver          PBiCG;
        preconditioner  DILU;
        tolerance       1e-05;
        relTol          0;
    }

    rhoS
    {
        solver          PBiCG;
        preconditioner  DILU;
        tolerance       1e-05;
        relTol          0;
    }
    rhoT
    {
        solver          PBiCG;
        preconditioner  DILU;
        tolerance       1e-05;
        relTol          0;
    }
//

    k
    {
        solver          PBiCG;
        preconditioner  DILU;
        tolerance       1e-05;
        relTol          0;
    }

    epsilon
    {
        solver          PBiCG;
        preconditioner  DILU;
        tolerance       1e-05;
        relTol          0;
    }
```

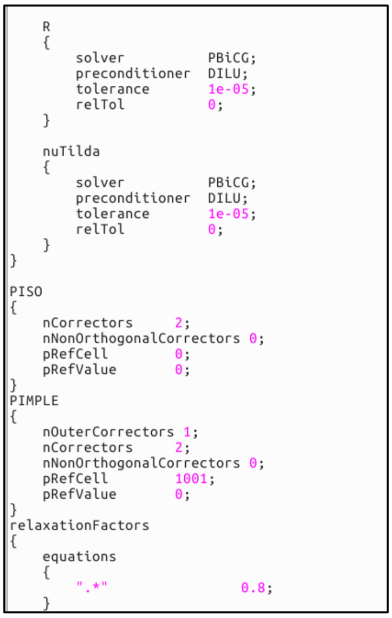

```
    R
    {
        solver          PBiCG;
        preconditioner  DILU;
        tolerance       1e-05;
        relTol          0;
    }

    nuTilda
    {
        solver          PBiCG;
        preconditioner  DILU;
        tolerance       1e-05;
        relTol          0;
    }
}

PISO
{
    nCorrectors     2;
    nNonOrthogonalCorrectors 0;
    pRefCell        0;
    pRefValue       0;
}
PIMPLE
{
    nOuterCorrectors 1;
    nCorrectors     2;
    nNonOrthogonalCorrectors 0;
    pRefCell        1001;
    pRefValue       0;
}
relaxationFactors
{
    equations
    {
        ".*"                   0.8;
    }
```

### *0 folder*

The detailed initial conditions of this study will be described in **Chapter 4:** Numerical modeling of inclined dense jets in stagnant ambient water on a sloped bottom.

# Chapter 4 Technical Paper: Numerical Modeling of Inclined Dense Jets in Stagnant Ambient Water on a Sloped Bottom [1]

**Abstract** – Desalination plants have a significant potential to alleviate water resource scarcity in many areas and countries. Outfall characteristics need to be investigated since brine discharge can be harmful to the marine environment. Compared with direct discharging methods, which could cause serious consequences for both the environment and the economy, inclined dense jets can be used in discharge systems to enhance the mixing efficiency and reduce environmental impacts. Although much research has been done on inclined dense jets on horizontal bottoms, the mixing of inclined dense jets on sloped bottoms has been less studied. In this research, numerical simulations of inclined dense turbulent jets in stagnant ambient water with three different sloped bottoms (2°, 5°, 10°) were conducted. One Reynolds-Averaged Navier-Stokes turbulence model: Realizable $K{-}\varepsilon$, was applied in predicting the jet mixing properties using a finite volume model (OpenFOAM). Based on the numerical results, the geometrical properties, such as terminal rise height, return point, impact point, and location of centerline peak were investigated. The dilution variation along the bottom was also investigated. The results were compared with various experiments. It was found that Realizable $K-\varepsilon$ performed well compared with the other $K-\varepsilon$ models. The slope can enhance the dilution on the bottom up to 20% higher than a horizontal bottom within the range considered in this paper.

Keywords: inclined dense jet, sloped bottom, mixing, OpenFOAM, CFD

---

[1] Xinyun Wang and Abdolmajid Mohammadian, "Numerical modeling of inclined dense jets in stagnant ambient water on a sloped bottom", ready to submit to Desalination and Water Treatment

## 4.1 Introduction

Desalination plants are becoming indispensable for many countries to reduce the pressure of water scarcity due to increasing population and limited freshwater resources. Desalination is the method of distractining salts and minerals from seawater to meet agricultural, industrial, or drinking water standards. The main environmental problem of desalination plants is brine discharge. The concentration of the brine is usually 3%~5%, or even sometimes up to 25% higher than the receiving water, depending on the desalination processing method (Baawain *et al.*, 2015). Improper discharging can lead to fatal environmental impacts for marine species near outfall systems. A similar challenge of discharge is also encountered in some domestic industrial wastewater discharge outfalls. One approach is discharging the brine directly from the outfalls (without any diffuser), and although this is the most economical solution, it could cause a large area of pollution on the seabed due to lower mixing and dilution processes (Figure 4.1.a).

Typically, concentrated brine is discharged in the form of IDJ (inclined dense jet) from submerged diffusers set on the seabed (Figure 4.1.b). Comparing these two methods, the IDJ can increase the initial dilution rate and reduce pollution on the seabed. Since the brine is denser, it will fall back onto the seafloor eventually and develop a gravity current moving along the seabed.

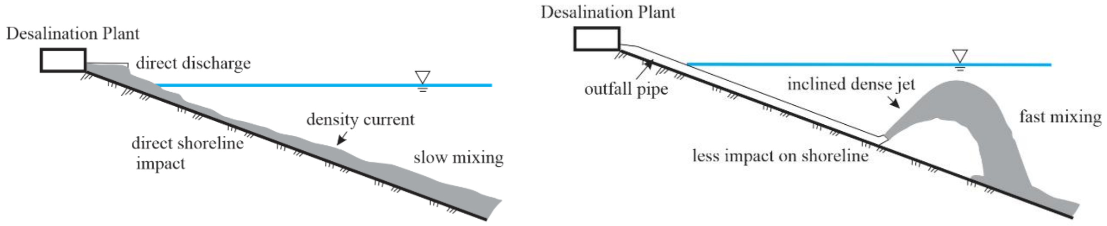

(a) direct discharge (b) inclined dense jet

Figure 4.1 Two discharge methods at desalination plant outfalls (Modified after (Bleninger and Jirka 2008))

As a result of increased interest in IDJ, extensive research has been conducted and applied for decades. Many studies have had a tendency to focus on the location and the concentration of the terminal height ($Y_t$) and return point (or impact point) ($X_i$ or $X_r$), which is the point where the jet falls back to the horizontal bottom (Figure 4.2). The information of these two points produces environmental concerns about when the jet is nearest the surface and when it returns to the seafloor.

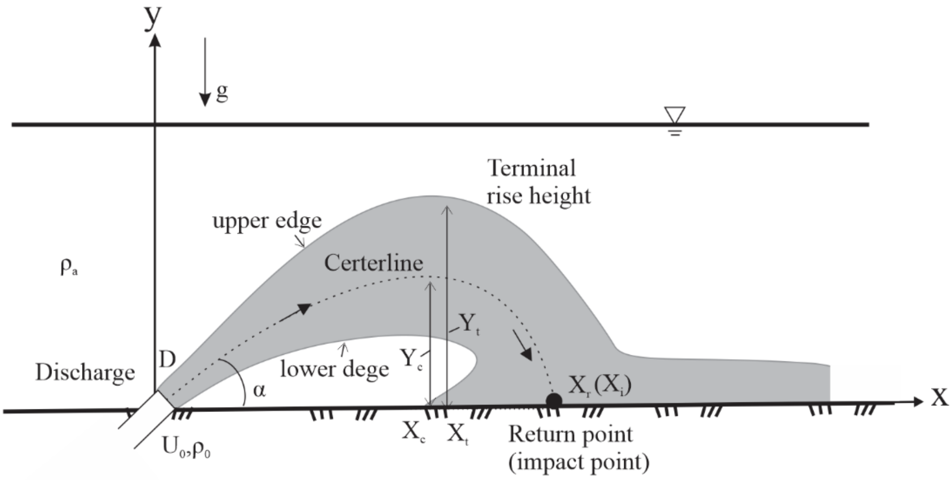

Figure 4.2. Schematic diagram of a typical negative buoyant jet on a horizontal bottom

Experimental and numerical modeling studies of IDJ with different angles in stagnant water have been carried out by many researchers with PIV or PLIF or other technologies to obtain the geometric and dilution characteristics of IDJ with discharge angles ranging from 0 to 90°(Roberts *et al.*, 1997), (Cipollina *et al.*, 2004, 2005),(Kikkert *et al.*, 2007,2010), (Lai and Lee, 2012) (Shao and Law, 2010) (Papakonstantis *et al.*, 2011a, 2011b) (Bashitialshaaer *et al.*, 2012) (Crowe 2013). It is time-consuming to build large-scale experiments to simulate the real case. To deal with a wide range of brine discharge angles and velocities, mathematical and numerical models have been applied to provide a comprehensive prediction in outfall design. In particular, the computational fluid dynamics (CFD) models are becoming popular in predicting the mixing behavior. Different CFD simulations of IDJ have been performed by various authors, including integral models such as CorJet (Jirka 2004) (Jirka 2008), VISJET (LEE JHW 2003) and Visual Plumes (Frick 1984). Hydrodynamic methods have also been used by solving Reynolds-averaged Navier-Stokes (RANS) or Large Eddy Simulation (LES) models using open source toolboxes or software such as OpenFOAM and Ansys Fluent (Gildeh *et al.*, 2015, 2016)(Mohammadian *et al.*, 2020) (Zhang *et al.*, 2017) (Oliver *et al.*, 2008)(Zhang *et al.*, 2016). The results showed good agreement with the experimental studies. All these studies provided dimensionless coefficients to predict key quantities of jet mixing. (Table 2)

The influence of boundary interaction on the behavior of IDJ should be addressed. Many studies focused on a horizontal bottom or ignored the effect of the bottom. Roberts *et al.*, (1997) did some research on the spreading layer including layer thickness and end zone of jet mixing. In practice, the brine still can affect the bottom boundaries after falling back and the seabed usually has a natural inclination. Comparing Figure 4.2 with Figure 4.3, the jet will continue moving along the bottom after the return point, and some geometric and dilution characteristics change due to the slope.

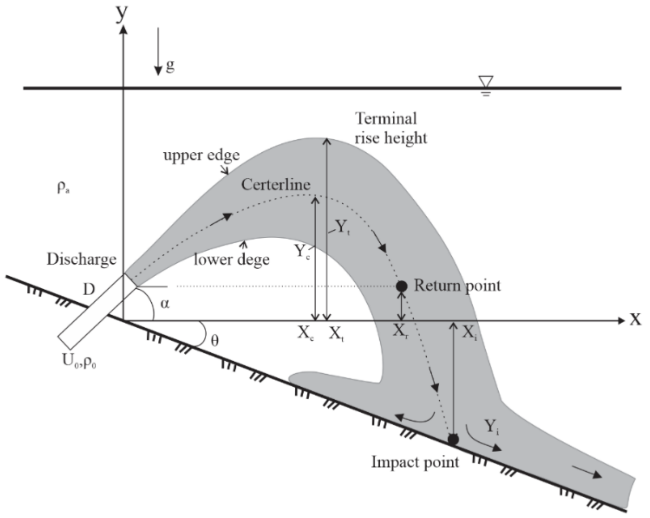

Figure 4.3 Schematic side view of IDJ discharging into stagnant ambient water on the sloped bottom

Although there have been few experimental studies on the slope bottom, the intergal model and analytical solution of the jet on the sloped bottom are carried out by many researchers.

Jirka (2008) firstly carried out numerical integral modeling using Corjet (Jirka 2004) to study IDJ on a sloped bottom (Figure 4.4).

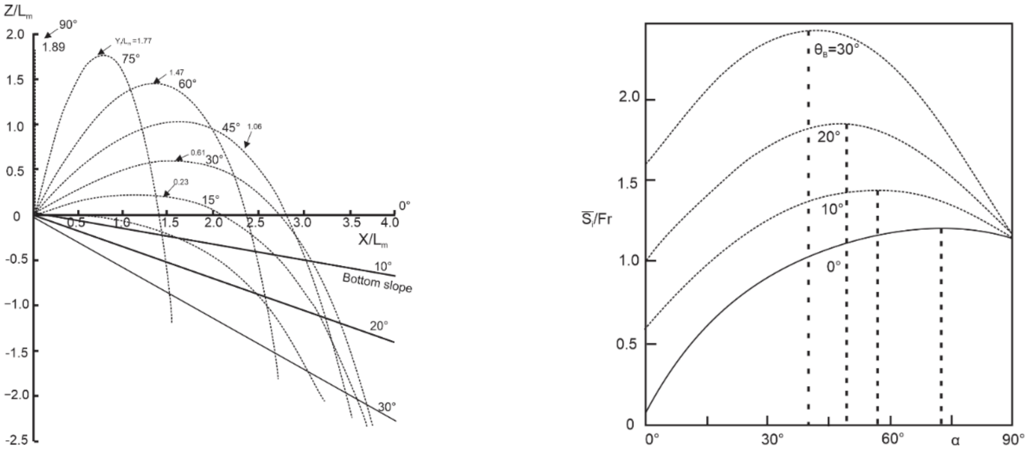

(a)

(b)

*(a) jet trajectories; (b) bulk dilution ($\frac{\overline{S_\iota}}{Fr}$)variation at different discharge angle and different sloped angle (bulk dilution ($\overline{S_\iota} \cong 1.7S_i$) $S_i$ -minimum dilution at impact point)*

Figure 4.4 Complete range of IDJ behaviour ($0° \leq \alpha \leq 90°$) on a variable sloped bottom angle ($0° \leq \theta \leq 30°$)(Performed by Corjet)(modified after Jirka (2008))

After validating the model by comparing results with jet on a horizontal bottom, he expands this method to sloped bottom. He showed that the longest impact point location can be provided by the discharge angle from 30° to 45°(Figure 4.4a), and the maximum dilution at impact point is changing with the discharge inclination and slope angle. Analyzing dilution at impact point under different discharge circumstances, one conclusion is that in practical designs a flatter discharge angel (30~45°) has design advantages, especially with a sloped bottom. Oliver *et al*., (2013) developed one extension of semi-analytical solution which based on Kikkert's method(2007) and found out the location information of the impact point on the nominal slope bottom.

Nikiforakis *et al*., (2014) carried out one experimental study of an IDJ on a sloped bottom, they applied point measurement by conductivity probes to get concentration information on the jet after the impact point with different Froude numbers (11~23). They measured the concentration at some locations after the impact point (eg. C1) on a vertical five points at 1, 2, 3, 4 and 6cm above the bottom (shown as a white line in Figure 4.5a).

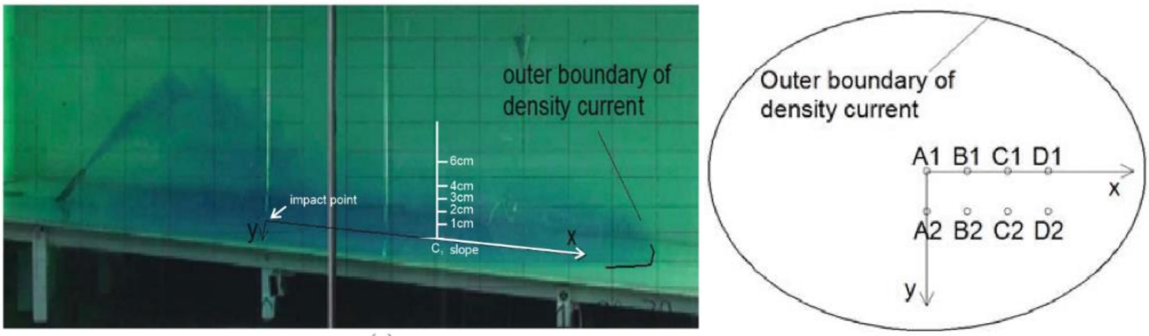

(a) (b)

Figure 4.5 (a) Experiment tank with a demonstration of concentration measurements location (b) top view of measurement location (Modified after (Nikiforakis *et al*., 2014))

They found that the dilution value for a discharge inclination of 60° is higher than for 45°. The vertical concentration profiles were approximately linear; however, there was little information about spatial characteristics and geometric properties, and they did not offer any information on the variation of the concentration along the sloped bottom.

This paper presents the results of numerical modeling on IDJ in ambient water on a sloped bottom. One discharge angle (30°) with three sloped bottoms (2°, 5°, 10°) have been applied in an open source CFD software: OpenFOAM. Mixing behavior and geometric characteristics of jets were studied, including information on terminal rise height, impact point and properties after impact point and centerline trajectory. Four different Reynolds Averaged Navier-Stokes models (Realizable $-\varepsilon$ , RNG $K-\varepsilon,$ Standard $K-\varepsilon,$ and nonlinear $K-\varepsilon$) were applied and compared with exiting experimental data in this field. For brevity, this paper mainly shows the results from the model that presented the closest match to experimental data (Realizable $K-\varepsilon$).

## 4.2 Dimensional analysis

All the data from experienmental study should be scaled upon dimensionless parameters to make data applicable into large-scale industrial designs. In the scope of IDJ, the typical dimensionless parameter is the initial densimetric Froude number, defined as

$$F=\frac{M^{5/4}}{QB^{1/2}} \text{ or } F=\frac{U}{\sqrt{g_0 D}} \tag{4.1}$$

Where M is the kinematic momentum flux, which can be written as

$$M=\pi d^2 U^2/4 \tag{4.2}$$

The volume flux of the jet can be calculated as

$$Q=\pi d^2 U/4 \tag{4.3}$$

The kinematic buoyancy flux is given by

$$B=g'Q \tag{4.4}$$

Where d is the nozzle diameter, u is the jet velocity, $g'$ is specific gravitational acceleration, which is defined as

$$g'=g\frac{\Delta\rho}{\rho_a}.\ \Delta\rho=\rho_0-\rho_a \tag{4.5}$$

From these fluxes, two important length scales are commonly used in jet analysis.

$$\mathrm{L_m}=\frac{M^{3/4}}{B^{1/2}} \tag{4.6}$$

$$\mathrm{L_q}=\frac{Q}{M^{1/2}} \tag{4.7}$$

$\mathrm{L_q}$ is the distance where the initial volume flux approximately equal to volume flux of the entrained ambient fluid (Nemlioglu *et al.*, 2014). $\mathrm{L_m}$ is the distance where jet momentum shows more dominance than buoyancy. These two length scales ($\mathrm{L_m}$ and $\mathrm{L_q}$) can be related to the jet diameter (D) and densimetric Froude number as $\mathrm{L_m}=(\pi/4)^{1/4}FD$ and $\mathrm{L_q}=$

$(\pi/4)^{1/2}D$. The initial volume flux becomes dynamically unimportant when the distance from the nozzle is much greater than $L_q$(Roberts *et al.*, 1997).

A typical negative buoyant jet is shown in Figure 4.6. It features a nozzle inclined upwards above the horizontal plane with an angled discharge through a round nozzle with diameter D at velocity U.

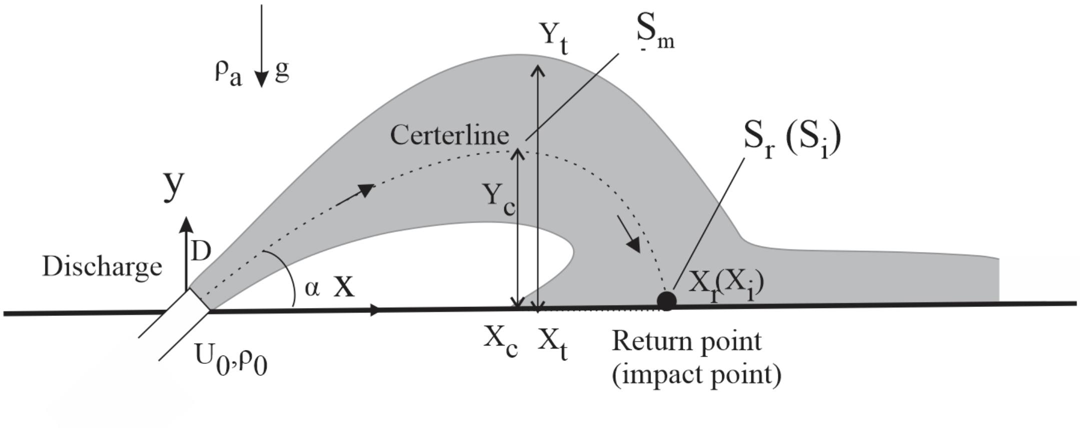

Figure 4.6 Schematic diagram of a typical IDJ on a horizontal bottom

There are some important dimensional analyses and dimensionless parameters in jet studies. For a dense jet with an angle to horizontal $\alpha$ in a stagnant ambient, the terminal rise height of jet y can be estimated by

$$\frac{y_t}{L_m} = f_1\left(\frac{L_m}{L_q}, \alpha\right) \qquad \text{or} \qquad \frac{y_t}{FD} = f_2(F, \alpha) \tag{4.8}$$

Also, the dilution of the jet at any point can be estimated from

$$S = \frac{\rho_0 - \rho_a}{\rho - \rho_a} \tag{4.9}$$

Where $\rho$ is the local density.

Similarly, the centerline peak dilution $S_m$ (as well as return point dilution $S_r$ and impact point dilution $S_i$) in the literature can be expressed as:

$$\frac{S_m}{Fr} = f_3(F\,, \alpha) \tag{4.10}$$

The empirical functions $f_1$ , $f_2$ , $f_3$ can be derived from experiments or combined experimental-numerical studies.

Some important parameters for describing the geometric and dilution characteristics can be nondimensionalized by Fr and length scales; six parameters are adopted in this study and compared with previous research results in Table 4.2.

## 4.3 Computational methodology

### 4.3.1 Governing equations

In fluid dynamics, the most commonly used governing equations are known as Navier-Stokes equations, which were obtained over 150 years ago (Jamshed, 2015). In hydraulic applications, fundamental principles that are used deal with conservation of mass, momentum and energy.

Conservation of mass

$$\frac{\partial u}{\partial x}+\frac{\partial v}{\partial y}+\frac{\partial w}{\partial z}=0 \tag{4.11}$$

Where $u, v, w$ are the velocity components for x, y, z -axis, respectively.

The momentum equations for a three-dimensional system can be written as:

x- direction

$$\frac{\partial(\rho u_x)}{\partial t}+\left(\frac{\partial \rho u_x u_x}{\partial x}\right)+\left(\frac{\partial \rho u_y u_x}{\partial y}\right)+\left(\frac{\partial \rho u_z u_x}{\partial z}\right)=\left(\frac{\partial \tau_{x,x}}{\partial x}\right)+\left(\frac{\partial \tau_{x,y}}{\partial y}\right)+\left(\frac{\partial \tau_{z,x}}{\partial z}\right)-\frac{\partial P}{\partial x} \tag{4.12}$$

y- direction

$$\frac{\partial(\rho u_y)}{\partial t}+\left(\frac{\partial \rho u_x u_y}{\partial x}\right)+\left(\frac{\partial \rho u_y u_y}{\partial y}\right)+\left(\frac{\partial \rho u_z u_y}{\partial z}\right)=\left(\frac{\partial \tau_{x,y}}{\partial x}\right)+\left(\frac{\partial \tau_{y,y}}{\partial y}\right)+\left(\frac{\partial \tau_{z,y}}{\partial z}\right)-\frac{\partial P}{\partial y}-g \tag{4.13}$$

z-direction

$$\frac{\partial(\rho u_z)}{\partial t}+\left(\frac{\partial \rho u_x u_z}{\partial x}\right)+\left(\frac{\partial \rho u_z u_y}{\partial y}\right)+\left(\frac{\partial \rho u_z u_z}{\partial z}\right)=\left(\frac{\partial \tau_{x,z}}{\partial x}\right)+\left(\frac{\partial \tau_{y,z}}{\partial y}\right)+\left(\frac{\partial \tau_{z,z}}{\partial z}\right)-\frac{\partial P}{\partial z} \tag{4.14}$$

Where P is pressure, $\tau$ is shear stress, $\rho$ is density.

Shear stress terms in the momentum equations may be calculated using turbulence models. The reader is referred to Greenshields (2017) for the details of the turbulence models employed in this study which include Realizable $-\varepsilon$ , RNG $K-\varepsilon$, Standard $K-\varepsilon$, and nonlinear $K-\varepsilon$.

The flow was assumed to be incompressible in this study, and the density for both jet and ambient water was calculated by equation (4.15) proposed by Millero and Poisson (1981):

$$\rho = \rho_t + AS + BS^{3/2} + CS \qquad (4.15)$$

where

$$A = 8.24493 \times 10^{-1} - 4.0899 \times 10^{-3}T + 7.6438 \times 10^{-5}T^2 - 8.2467 \times 10^{-7}T^3 + 5.3875 \times 10^{-9}T^4$$

$$B = -5.72466 \times 10^{-3} + 1.0227 \times 10^{-4}T - 1.6546 \times 10^{-6}T^2$$

$$C = 4.8314 \times 10^{-4}$$

$\rho_t$ is the density of water, which varies with the temperature as follows:

$$\rho_t = 999.842594 + 6.793952 \times 10^{-2}T - 9.095290 \times 10^{-3}T^2 + 1.001685 \times 10^{-4}T^3 - 1.120083 \times 10^{-6}T^4 + 6.536336 \times 10^{-9}T^5$$

In this study, the temperature was assumed to be constant, and S refers to the salinity in water,. The density is related to temperature and salinity. The concentration evolution is modeled based on the advection-diffusion equation:

$$\frac{\partial s}{\partial t} + u_x \frac{\partial s}{\partial x} + u_y \frac{\partial s}{\partial y} + u_z \frac{\partial s}{\partial z} = \frac{\partial}{\partial x}\left(D \frac{\partial s}{\partial x}\right) + \frac{\partial}{\partial y}\left(D \frac{\partial s}{\partial y}\right) + \frac{\partial}{\partial z}\left(D \frac{\partial s}{\partial z}\right) \qquad (4.16)$$

where *D* is the diffusion coefficient obtained from turbulence models.

### 4.3.2 Flow configuration and computational setup

In this study, the open Source CFD software, OpenFOAM, was employed in which, the equations are discretized by the finite volume method. The implementation of the governing equation in OpenFOAM was carried out using a modified version of the built-in impressible solver "PisoFoam". The performed modifications included the addition of buoyancy terms and calculation of density, which was validated by Gildeh *et al.*, (2015).

Figure 5a shows a schematic diagram of the simulated experimental tank; there is a slope at the bottom. The other dimensions were the same as Gildeh (2015) and Shao and Law (2010) and the computational domain was the same as the physical domain noting that only half of the tank domain was considered to perform the simulation because the problem is symmetric. The numerical simulations were performed in a tank with dimensions of 1.2m length, 0.4m width, and 0.5m depth (Figure 4.7a); the slope started at the left end of the tank and descended toward the right end (point A) as can be seen in Figure 7c. A refined mesh was used for simulations to better capture velocity and concentration in the near field zone, especially for the bottom zone

(Figure 4.7b). In this study, using mesh independency analysis, a grid of 344,000 structured cells was found to be adequate in resolving the flow features for the considered domain.

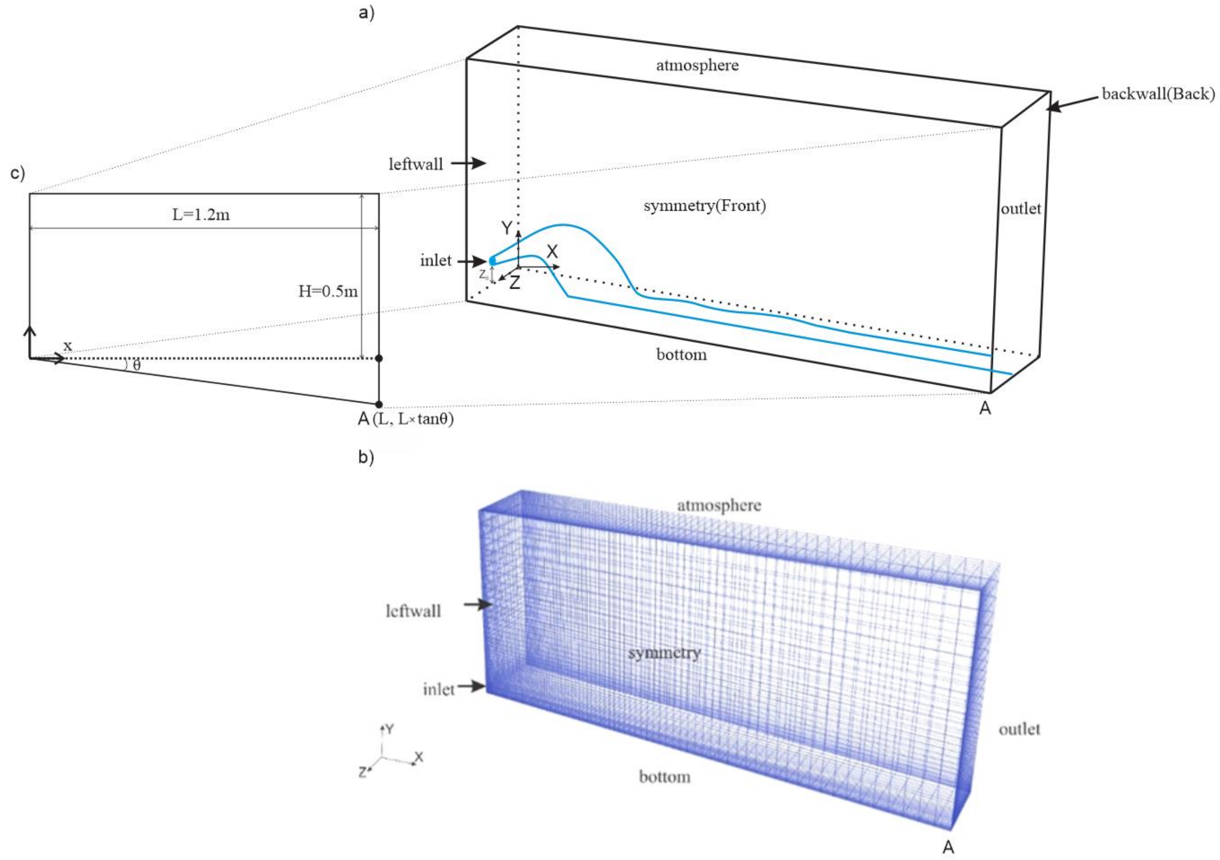

Figure 4.7 (a) the experimental tank with the additional sloped bottom; (b) computational domain with mesh system; (c) x-y plane view

The nozzle diameter (D) for the inlet was 10.7 mm and the center of the nozzle tip was fixed at 8.155mm ($Z_0$) with 30 degrees of positive incline. For the inlet, the boundary conditions were $u = U \times \cos(\alpha)\,, v = U \times \sin(\alpha)\,, w = 0, C = C_0 = S, T = T_0, k = 0.006u^2, \varepsilon = 0.06u^3/D$. Where, U is velocity of jet discharge, $u$, $v$ and $w$ are the velocity for x, y and z-axis respectively, C is the concentration of the brine. In this study, the author adopted salinity (S) as concentration (equation (4.15). The initial salinity can be calculated by equation (4.15). It needs to be mentioned that in the results and analysis section, for consistency with the literature, S means dilution, which is calculated from $C_0/C$, where $C_0$ is initial concentration and C is the local concentration. T represents temperature and in this study, the temperature is 22℃, which is the same as the ambient water. $k$ is turbulent kinetic energy and $\varepsilon$ is turbulent kinetic energy dissipation rate. For all walls, the standard wall function was used. Besides, the flow rate was fixed with U=0.6m/s. Three different slope angles θ= 2°, 5°, 10° and four different Froude numbers (15, 20, 25, 30) were applied in the simulations. The surrounding water density was set to 997.377$kg/m^3$. The initial conditions are listed in Table 4.1.

Table 4.1. Initial condition of the simulation

| Diameter (mm) | Velocity ($m/s$) | Froude Number | Density deference ($kg/m^3$) | Jet density( $kg/m^3$) | $L_m$ |
|---|---|---|---|---|---|
| 10.8 | 0.6 | 15 | 15.06815 | 1012.841 | 0.152 |
| 10.8 | 0.6 | 20 | 8.475853 | 1006.249 | 0.203 |
| 10.8 | 0.6 | 25 | 5.424559 | 1003.198 | 0.254 |
| 10.8 | 0.6 | 30 | 3.767066 | 1001.54 | 0.304 |

## 4.4 Convergence and sensitivity tests

The mesh quality is important for the numerical modeling results. In this part, coarse, medium, and fine meshes were used. Table 4.2 presents a summary of different mesh parameters of these grids.

Table 4.2 Numbers of cells and mesh quality parameters for different mesh types

| Mesh quantity | Numbers of blocks | Min volume | Max volume | Max aspect ratio | Max skewness |
|---|---|---|---|---|---|
| Coarse | $7.7832 \times 10^4$ | $9.11377 \times 10^{-8}$ | $3.17799 \times 10^{-5}$ | 29.4905 | 0.13617 |
| Medium | $3.344 \times 10^5$ | $2.12152 \times 10^{-9}$ | $1.33653 \times 10^{-5}$ | 18.4715 | 0.1571711 |
| Fine | $5.72832 \times 10^5$ | $2.88455 \times 10^{-9}$ | $4.86699 \times 10^{-5}$ | 51.8429 | 0.129718 |

Three velocity and concentration profiles for the case Fr=15 were used to check the mesh sensitivity, and the results at different locations x=1DF, x=3DF and x=5DF were compared for each profile. The concentration and velocity profiles were compared over the nondimensionalized distance y/DF as the y-axis.

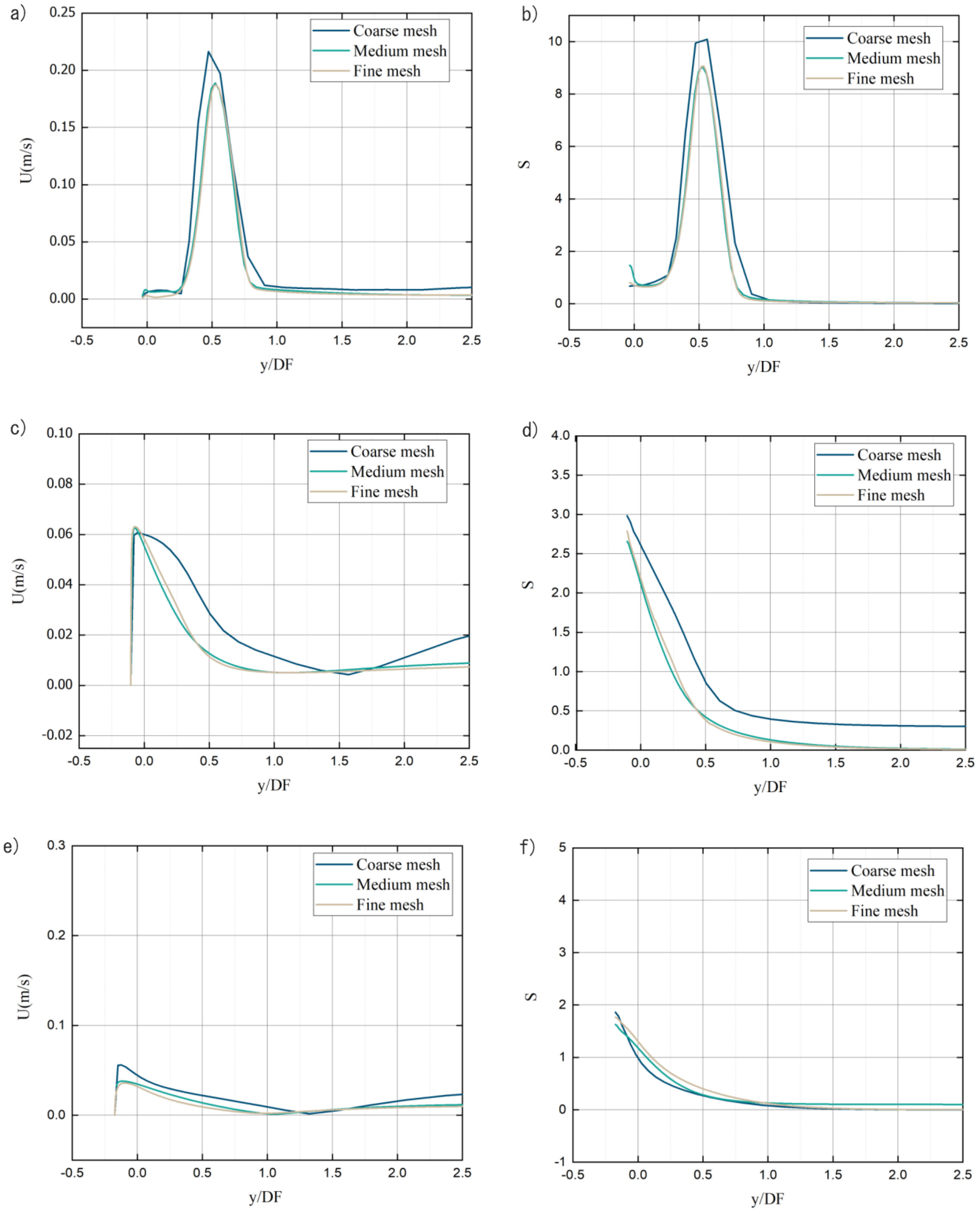

Figure 4.8 Mesh sensitivity analysis (a), (c), (e) velocity profiles respectively at x=1DF, 3DFand 5DF; (b), (d), (f) concentration profiles respectively at x=0.5DF, 1DF and 3DF.

Figure 4.8 shows that the mesh quality significantly affected the simulation results; the coarse mesh led to overestimation but results of concentration and velocity of the middle and fine meshes were very close. Considering both accuracy and computational efficiency, the medium mesh was selected in this study.

## 4.5 Results and discussion

Four different Froude numbers, (15, 20, 25, 30), one discharge angle (30°) with three different bottom slope angles (2°, 5 °, and 10°) were numerically simulated using Realizable $k-\varepsilon$, nonlinear $k-\varepsilon$ , RNG $k-\varepsilon$ and standard $k-\varepsilon$, leading to a total of $4\times4\times4=48$ simulations.

Figure 4.9 shows a comparison of various turbulence models with experimental data. Overall, Realizable $k$- $\varepsilon$ model shows better results compared with experiments. Therefore, the results and discussions in the rest of this paper only include Realizable $k-\varepsilon$ model.

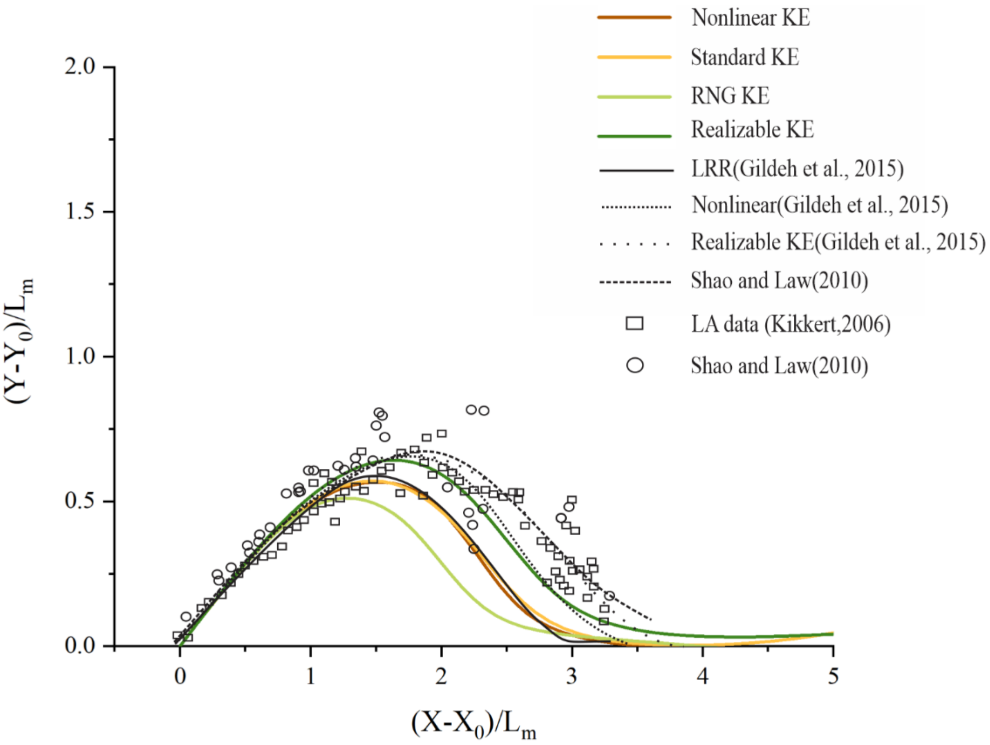

Figure 4.9 Trajectories of inclined dense jets from four models

### 4.5.1 Cross-section concentration profiles

Figure 4.10 shows concentration transverse distribution of the jet with the non-dimensionalized concentration $C/C_m$ plotted against dimensionless normal coordinate $r/b_c$, where $C$ is the concentration along the cross section. $C_m$ is the maximum concentration of the cross-section, $r$ is the radial distance and $b_c$ is the concentration spread width (using the $e^{-1}$ notation). Figure 9 shows one simulation result of jet concentration profile and three different concentration profiles (white dash line), and compared with Lai's experiment (Lai and Lee 2012), all the results have good agreement with experimental data. Similar trends also can be found in Shao's experiments (Shao and Law 2010).

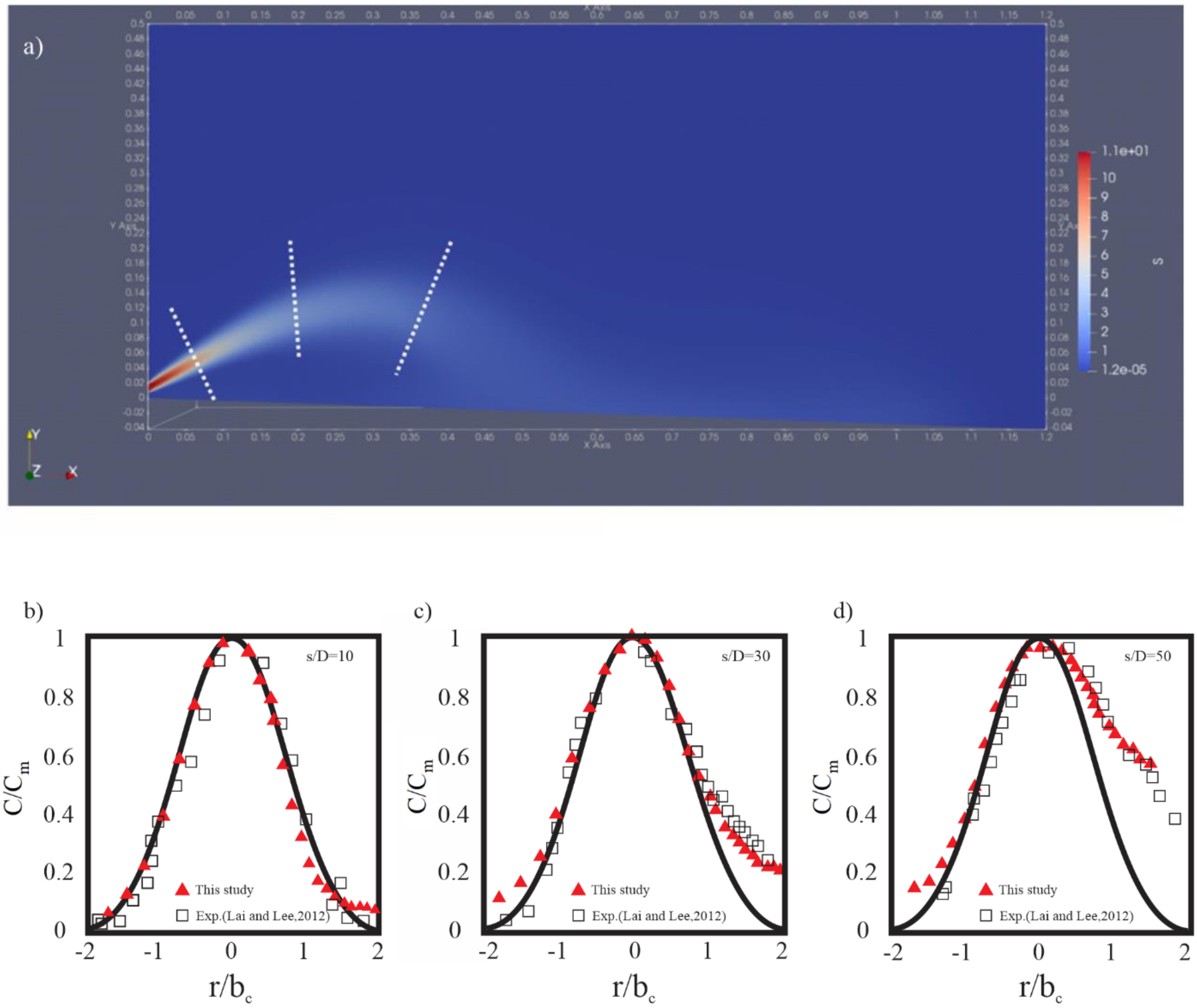

Figure 4.10 (a) Simulation result of concentration profile; (b),(c) and (d) cross-sectional profiles for s/D=10,30 and 50, respectively.

Figure 4.10 (a) shows a concentration profile for one case of IDJ (Fr=20, slope angel =2°), close to the discharge outlet. The flow can be seen to be dominated by momentum, it performed as jet. Close to the terminal rise height, the flow started spreading, the jet reached the highest point because the buoyancy effect became equal to the momentum effect. After the flow reached the highest point, it dropped towards the bottom due to gravity. During this process, more mixing and detrainment occurred, which caused flow change from jet-like to plume-like. Figures 4.10 (b),(c) and (d) are three presentative cross-section profiles of concentration fields compared with the results of Lai and Lee (2012). They can show different stages: (a) the initial stage of the jet, where the jet was dominated by the initial momentum, and concentration profiles were Gaussian distribution, (b) approaching terminal rise height, where the lower part of the jet started detraining and departing from the Gaussian line, (c) after the terminal rise height, where more detrainment and mixing happened at the lower boundary of the jet.

At the initial stage of the jet development, where $s/D \leq 20$ (Figure 4.10b), with $s$ (small letter), represents a distance along trajectory, the profiles can be described as a Gaussian distribution. After this point, s/D =30 (Figure 4.10c), the inner (lower) half had a trend that started to depart from Gaussian, whereas the outer (upper) half remained Gaussian, which means that the inner part was spread wider than the outer part, and this indicates the detrainment happened at the lower half (Figure 4.10d). After the terminal rise point, the jet can be conceptually thought of as a negatively buoyant jet behaving as a pure plume (Lai and Lee 2012).

### 4.5.2 Centerline maximum velocity decay

For the case of vertical buoyant jets, Chen and Rodi (1980) indicated that the maximum concentration along the jet centerline can be represented by a power-law relationship with dimensionless centerline dilution ($C_m/C_0$ ), Froude number (Fr), and the non-dimensionalized vertical elevation:

$$F \cdot C_m/C_0 = a(y/D\,/F)^b \tag{4.17}$$

Where $C_m$ is the maximum profile concentration and $C_0$ is the initial concentration, y is the profile elevation, $a$ and $b$ are the constants related to the types of flow, either jet, transition, or plume regime. A similar relationship can be observed for the normalized maximum centerline velocity in the case of IDJ ($U_m/U_0$), see e.g. (Shao and Law 2010) and Gildeh *et al.*, (2015). The variation of the normalized maximum centerline velocity versus the normalized location along the trajectory with different slopes is plotted in Figure 4.11. A logarithmic scale was used and the results for 10 cross-sections with Froude number 20 are shown.

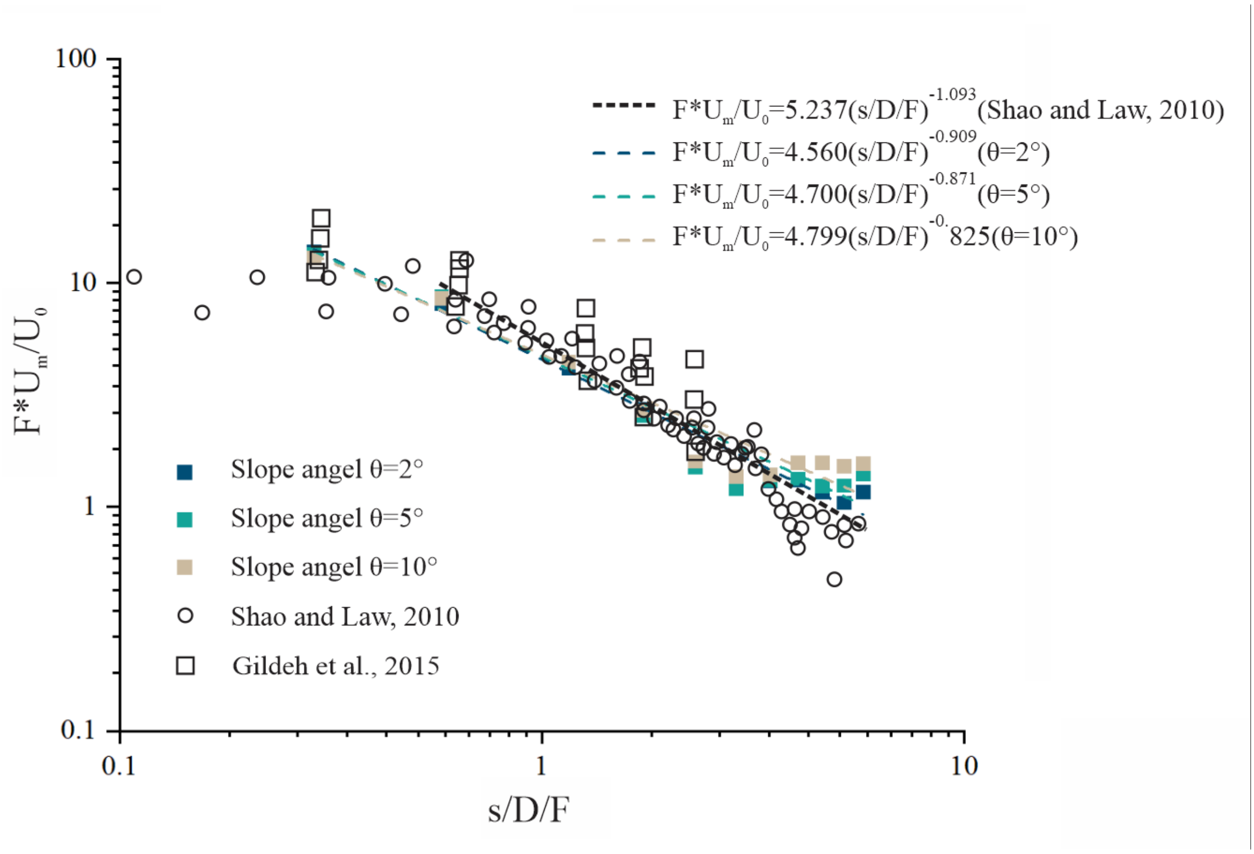

Figure 4.11 Non-dimensionalized centerline maximum velocity magnitude decay along jet trajectory (log scale)

As seen from the figure, the results have good agreement with previous studies. The velocity at the centerline decreased almost linearly before the impingement. Near the impingement, the decay of velocity was affected by the slope. The value of velocity on the slope ($U_m$) became stable and even increased slightly. On the slope, the gravity dominated the jet plume movement, the steeper slope (gray square) had larger $F \cdot U_m/U_0$ than the smaller slope (dark blue square), which means the steeper slope can provide energy for the flow to move due to gravity.

A similar method for concentration decay along jet trajectory was adopted as shown in Figure 4.12. Three fitting approximation lines (in log scale) are also presented. For better comparison. Figure 4.13 shows both maximum velocity and maximum concentration in the same graph. For the vertical axis R means Um or Cm, the circle dots show the concentration, and stars represent velocity.

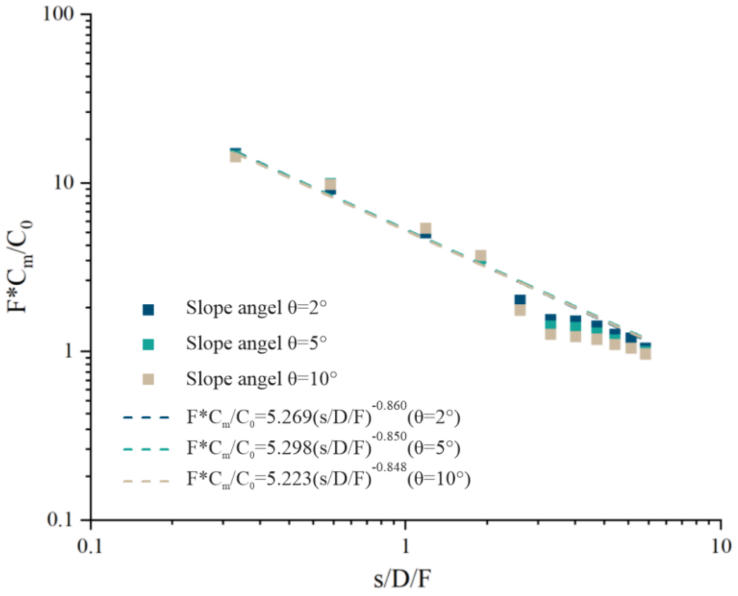

Figure 4.12 Non-dimensionalized centerline maximum concentration magnitude decay along jet trajectory (log scale)

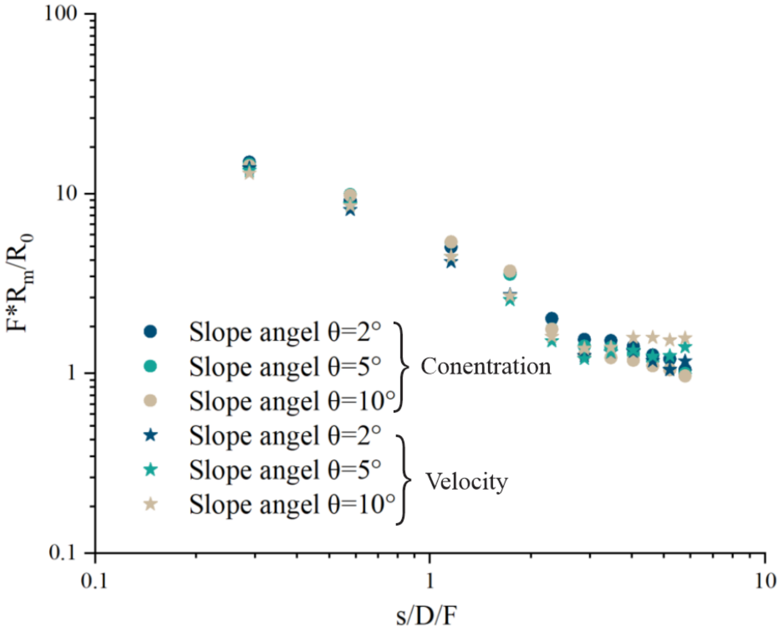

Figure 4.13 Comparison of non-dimensionalized centerline maximum velocity and concentration decay along jet trajectory (log scale)

It can be seen that the velocity decreased faster than the concentration before the impingement. After the impingement, the slope affected the changes in concentration and velocity. Velocity and concentration showed a different pattern. With a larger slope angle, the velocity increased, and concentration decreased. Indeed, due to the effect of gravity and slope leading to additional momentum compared with the horizontal bottom, the velocity increased. Concentration, however, decreased due to further dilution.

### 4.5.3 Jet trajectory and overflow characteristics

The jet trajectory, which also can be called the jet centerline, is the main geometrical property of the IDJ, it can reveal the overall jet characteristics. Trajectory is often derived from the maximum velocity or concentration at various cross-sections perpendicular to the jet. The study by (Shao and Law, 2010) showed that the concentration and velocity trajectories are mostly coinciding. The velocity profile was adopted in this study for brevity.

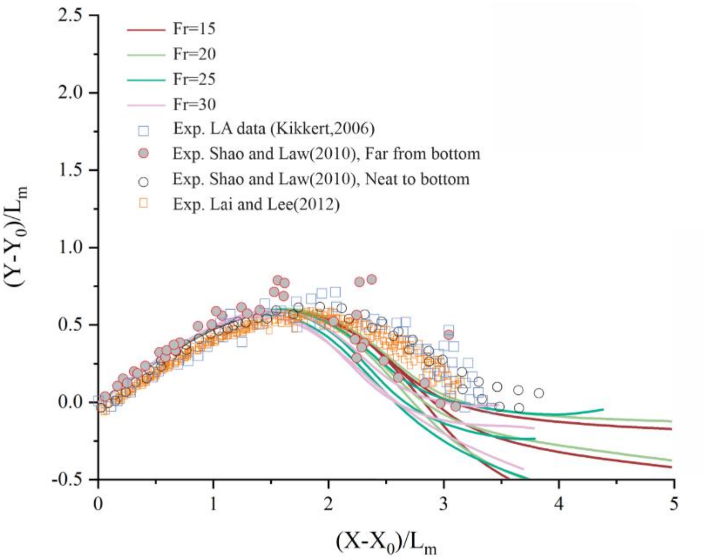

Figure 4.14 Normalized centerline trajectories

Figure 4.14 shows the normalized centerlines with different Fr numbers. The results of numerical models were made dimensionless to obtain a better comparison with experimental data, and the trajectories were normalized by $L_m$. $X_0$ and $Y_0$ give the location of the inlet (source), which are 0m and 0.013m, respectively. Some available experiments are included for the comparison(Lai and Lee 2012) (Shao and Law 2010) (Kikkert *et al.*, 2007b). Since there is no experimental data of IDJs on a sloped bottom, it is reasonable to compare the results before the return point to evaluate the performance of the numerical model. The results showed good agreement with previous studies.

Before the return point, the jets were almost symmetrical for both ascending and descending phases. After the return point, the jet trajectories were greatly affected by the sloped bottom. As mentioned, the jet passed through the return point and hit the bottom, and then moved along the sloped bottom. The boundary interaction is also mentioned in some studies, especially for the data at the return or the impact point. The impingement happened here, and the dilution along the boundary varied in a very complex manner. There is another potential influence from the bottom boundary investigated by Shao and Law (2010). When the jet discharge point is close to an impermeable and horizontal boundary, the Coanda attachment will occur, which can reduce the mixing and lead to excessive salinity along the seabed. To avoid this influence of boundary interaction, they pointed out the minimum source height necessary, which is

$$Hs/FD > 0.74 \qquad (4.18)$$

In this study, the ratio was smaller than 0.74, but no Coanda attachment was observed. The reason for this might be that the value 0.74 is an approximate value. Other potential reasons include the fact that the slope might affect the Coanda attachment. In addition, the numerical model might not be able to precisely capture the Coanda attachment.

### 4.5.4 Geometrical and mixing characteristics

The geometrical properties of IDJs are important for outfall design. Many geometrical characteristics can be defined in dimensionless form, including locations of terminal rise height, the maximum centerline peak, the location of the return point, and the impact point. These geometric parameters can be extracted from the centerline trajectory of the IDJ. Some experimental studies have indicated that the return point and impact point can be treated as one point due to the limitation of operability (Oliver, Davidson *et al.*, 2013). In this study, the return point and impact point will be discussed separately.

A summary of parameters from this study and previous studies is shown in Table 4.3. The parameters of terminal rise height, the horizontal location of the terminal rise height, and vertical location of the centerline peak, all have good agreement with experimental and numerical studies.

*Jet terminal rise height*

For an IDJ with an inclined angle, the jet will rise then fall back to the bottom. The terminal height ($X_t$, $Y_t$) is an important parameter in the outfall design to make sure the effluent water under the water’s surface prevents water surface pollution. Terminal rise height is defined as the point at which the vertical component of the momentum decreases to zero. Various terminologies have been used in previous studies, such as the maximum height of top boundary (Zeitoun and McIlhenny 1971), terminal rise height (Roberts *et al.*, 1997) (Shao and Law 2010) (Gildeh *et al.*, 2015), maximum rise height (Madni *et al.*, 1989), final fountain height

(Bloomfield and Kerr, 2002), maximum rise level (Cipollina *et al*., 2005) (Jirka, 2008) and maximum height of the outer edge (Kikkert *et al*., 2007). In this study, the term “terminal rise height” is adopted. It is made dimensionless as $C_1 = Y_t/L_m$.

In previous experimental studies, the most common way to obtain the terminal rise height was to find the boundary of the jet in captured photos, which will involve uncertainties and error due to the different types and the amounts of dye or the quality of the images.

There are two methods to determine the jet boundary. For the positively buoyant jet in a stagnant environment, the visual boundary for the jet can be defined by $0.25C_{max}$ concentration contour in the experiments (Chu *et al*., 1999) (LEE *et al*., 2012). This method was also adopted in the study of IDJ, since the tracer distribution at the upper half of the jet was Gaussian and the outer jet width growth had the same rate as the positively buoyant jet; the details can be found in Lai and Lee (2012). Figure 4.15 shows the $0.25C_{max}$ contour (white line with black arrow) at the highest point of profile of the trajectory ($C_{max}$ is the maximum concentration at the profile).

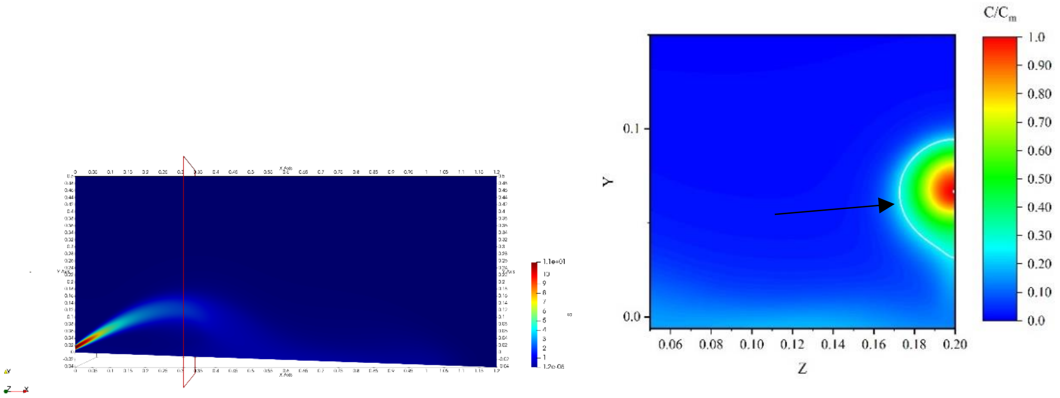

(a) (b)

Figure 4.15 $0.25C_{max}$ contour profile (a) A longitudinal section of the jet for Froude number F= 20 and slope=2° (b) Contour line corresponding to $0.25C_{max}$ highlighted by white line and black arrow

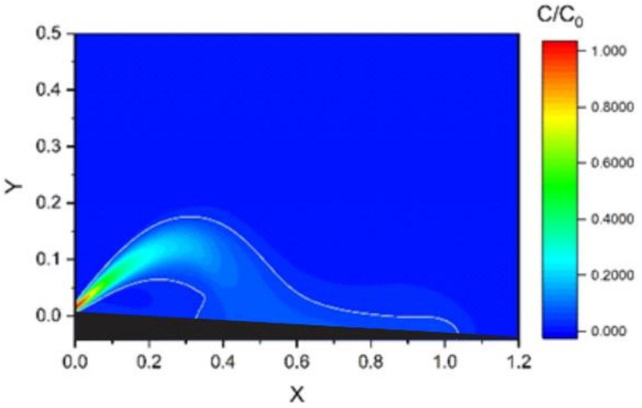

Figure 4.16 Contour line corresponding to 0.03C$_0$ (white line represents $0.03C_0$ contour line)

There is another way to obtain the terminal rise height. Shao and Law (2010) and Gildeh *et al.*, (2015) used $0.03C_0$ ($C_0$ is the initial concentration) as the visual boundary of the jet. Figure 4.16 shows the $0.03C_0$ contour presented by the white line.

The terminal rise height over the diameter $Y_t/D$ versus F is plotted in Figure 4.17a and compared with previous experimental studies. The terminal rise height values derived from two methods are very similar. There is a linear relationship between $Y_t/D$ and F. A higher Froude number has a larger terminal rise height, which is reasonable since the jet is dominated by the initial momentum during the ascending phase. In addition, the terminal rise height normalized by the DF versus F compared with the experiments from Lai and Lee (2012) is shown in Figure 4.17b. The results show good agreement of the dimensionless terminal rise height $Y_t/FD$ as a function of the jet Froude number.

The linear relationship between$Y_t/D$ and Fr could be better presented by normalizing $Y_t$ by $L_m$. In many experimental studies, $Y_t/L_m$ was only a function of the initial discharge angle. However, only one discharge angle was investigated in this study, and the results were compared with other studies (with 30°) to verify the numerical modeling results (Figure 4.18), which exhibited good agreement with the various experimental studies.

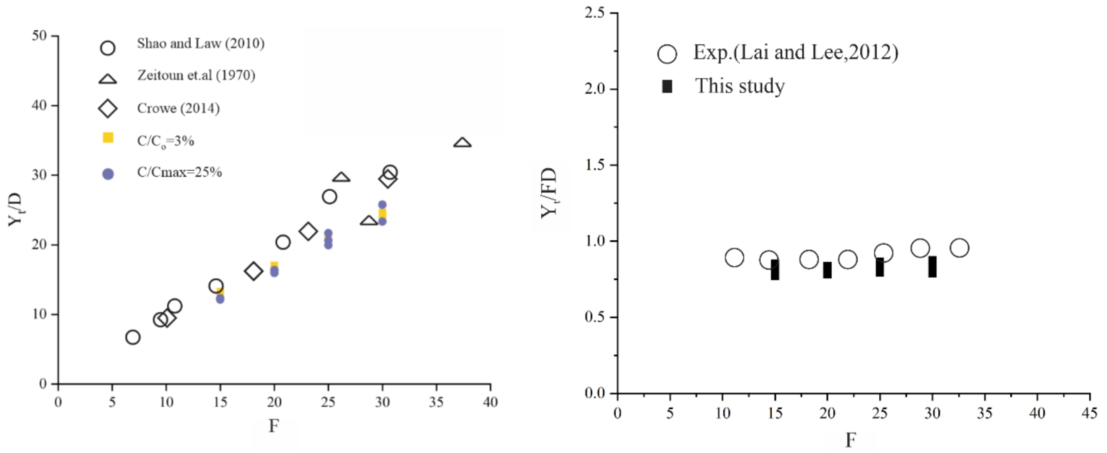

(a) (b)

Figure 4.17 (a) Terminal rise height normalized by D against Froude number; (b) Dimensionless terminal rise height against Froude number

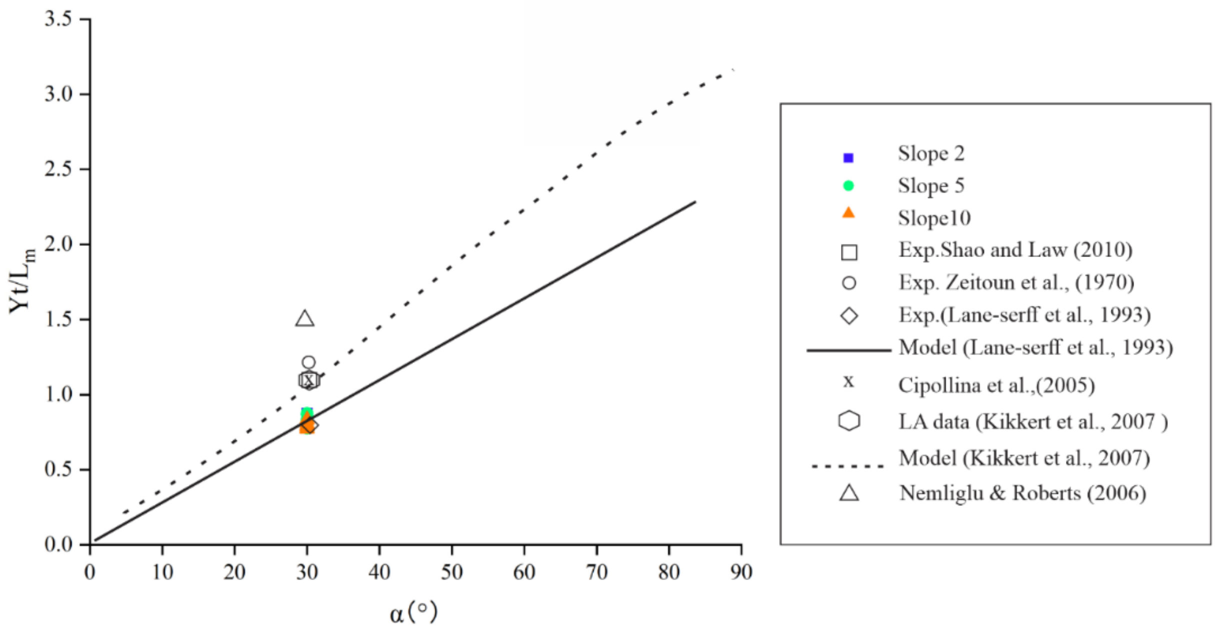

Figure 4.18 Normalized terminal rise height compared with one discharge angle (30°)

Table 4.3 Comparison of numerical and experimental coefficients for 30° discharge inclination

| Parameters | | Realizable KE | Lai and Lee (2012) | Shao and Lao (2010) | Kikkert (2007b) | Cipplina (2005) | Crow (2013) | Papakonstantis (2011) | Zeitouns (1971) | Oliver (thesis experiment) (2012) | Oliver numerical (2012) | Gildeh (2015) | Visjet (Lai and Lee 2012) |
|---|---|---|---|---|---|---|---|---|---|---|---|---|---|
| Terminal rise height ($Y_t$) | $C_1 = Y_t/L_m$ | 0.90 | 0.95 | - | 1.17 | 1.08 | 1.09 | 0.9 | 1.15 | 1.15 | 1.02 | 1.13 | 0.86 |
| Horizontal location of Terminal rise height ($X_t$) | $C_2 = X_t/L_m$ | 1.48 | 1.95 | 1.54 | 1.84/1.75 | 1.95 | 1.87 | | | 1.7 | 1.6 | | 1.52 |
| Vertical location of centerline peak ($Y_c$) | $C_3 = Y_c/L_m$ | 0.61 | 0.65 | | | | 0.69 | | | 0.66 | 0.58 | 0.71 | 0.56 |
| Centerline peak dilution ($S_m/Fr$ | $C_4 = S_m/L_m$ | 0.34 | 0.4 | 0.62 | | | | | 0.36 | 0.34 | | 0.65 | 0.31 |
| Return point($X_r$) | $C_5 = X_r/L_m$ | 2.24 | 3.18 | 3.00 | 3.40/3.07 | 3.03 | 3.56 | | - | 3.08 | | 3.4 | 2.15 |
| Dilution at return point | $C_6 = S_r/Fr$ | 0.65 | 0.82 | 1.45 | | | | | | 0.84 | | 1.27 | 0.64 |

*The location of the jet centerline peak*

The centerline peak can be derived from the centerline trajectory. Some researchers have assumed that the locations for $X_c$ and $X_t$are not the same. In this study, the difference between both points ranged from 0.52% to 3.87%. Thus, the two points were considered the same herein. The location of the maximum trajectory centerline ( $X_c$) was adopted.

Figure 4.19 shows the normalized $X_c$ and $Y_c$ from the present study compared with the previous study with the source angle. The results were consistent with the previous studies (Crowe 2013), (Oliver 2012) (Kikkert *et al*., 2007b) (Lai and Lee 2012) and (Cipollina *et al*. 2005). The horizontal location $X_c$ from the present study was slightly under-predicted compared with the experimental study(Crowe 2013) (Oliver 2012) (Kikkert *et al*., 2007b) (Lai and Lee 2012) and (Cipollina *et al*., 2005); the reason might be due to the limitations of the employed turbulence modeling approaches. Despite this, the results are still reasonable.

The centerline was closer to the upper edge of the dense jet. This is because the vertical density gradient at the upper edge of the jet with a negative value dampened the turbulent fluctuation. The opposite situation happened at the lower edge due to the positive value of the vertical density gradient. Thus, the upper edge was sharper and the centerline was closer to the upper edge. The same phenomenon can be seen in the experimental data of Shao and Law (2010).

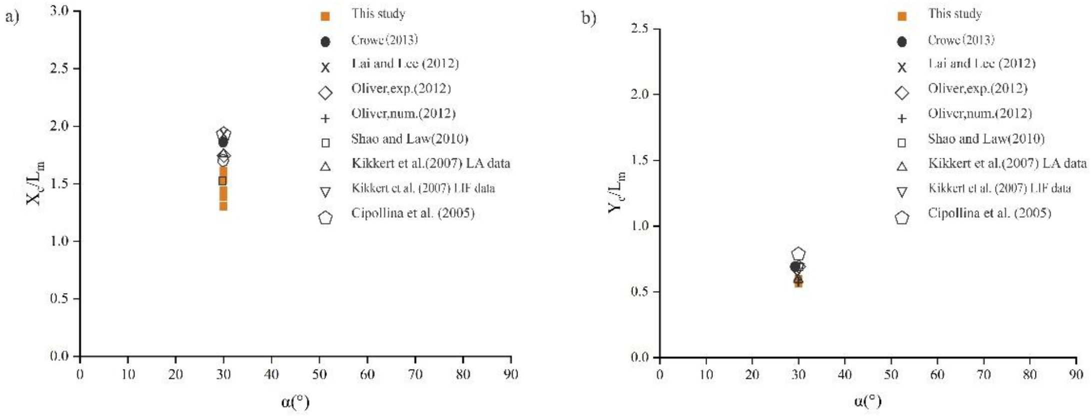

(a) Horizontal location

(b) Vertical location

Figure 4.19 Location of centerline peak compared with other experimental studies

*The location of the return point*

The IDJ will fall back to the lower boundary because of the negative buoyancy, and the location where the downward flow impinges on the boundary is often defined as the impact point or the impingement point ( $X_i$). The definition of return point ( $X_r$) is the location where the flow falls back to the source elevation, it is independent of the source height and bed slope. These two points (return point and impact point) are related with the source height and lower bottom condition, which is site specific. They can be seen as one point if the source is close to the bottom so that the difference between the return point and actual impact point is not significant (Figure 4.2). However, if the bed slope is large, these differences should be taken into consideration. In the present study, the return point and impact point were different points due to the sloped bottom (Figure 4.3).

According to Roberts *et al*., (1997), in the horizontal bottom, the impact point can be determined by the concentration variation along the lower boundary. In principle, the concentration increases from zero to the maximum at around the impact point and will be maintained at that level for a short distance before decrease. The same method is adopted in this study.

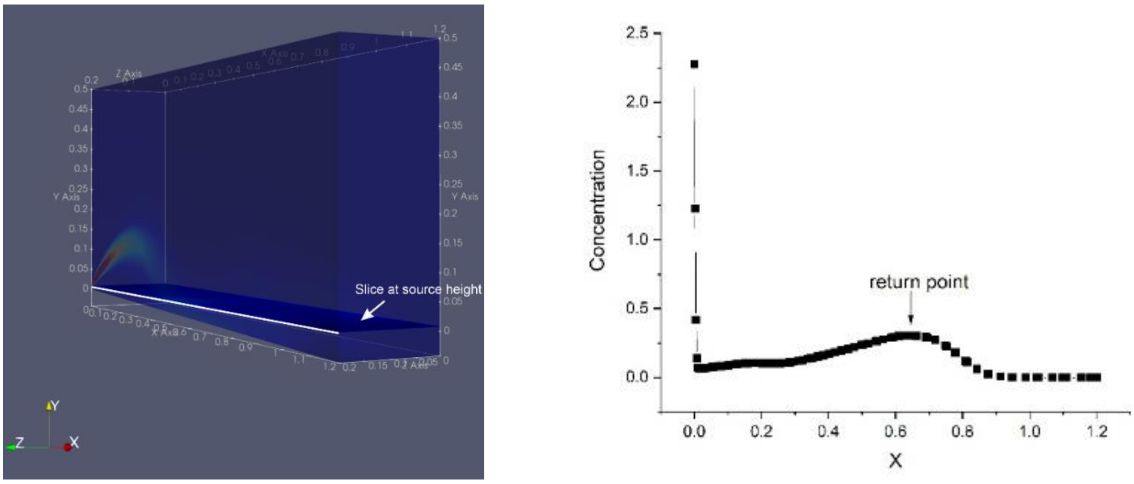

(a) (b)

*(a) Demonstration of a slice at the source height; (b) the concentration variation along the source elevation (along the white line in Figure 4.20a )*

Figure 4.20 Concentration variation on the horizontal slice at the source elevation

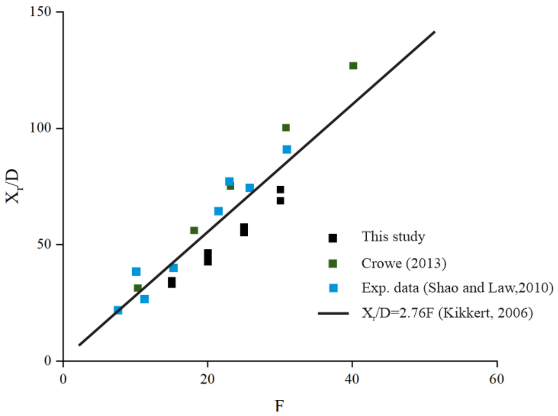

Figure 4.21 Normalized location of return point obtained from simulation compared with experiments

As shown in Figure 4.20, the return points were determined from the highest concentration point at the horizontal profile at the source elevation. The scatters are also plotted in Figure 4.21. $X_r$ was normalized by $D$ against Froude number and compared with the experimental studies as shown in Figure 4.21. The results demonstrated an under-prediction compared with experiments. The reason could be related to the employed turbulence model which might not be accurate enough given the complexity of the problem. In particular, buoyancy generated turbulence is not considered in the present study. Thus, during the descending phase, the concentration dropped faster than the velocity, which made the highest concentration point move inward in the numerical model.

*The location of impact point*

The location of the impact point was derived from the same method as the return point. It was found from the variation of lower boundary dilution along the bottom shown in while line (Figure 4.22).

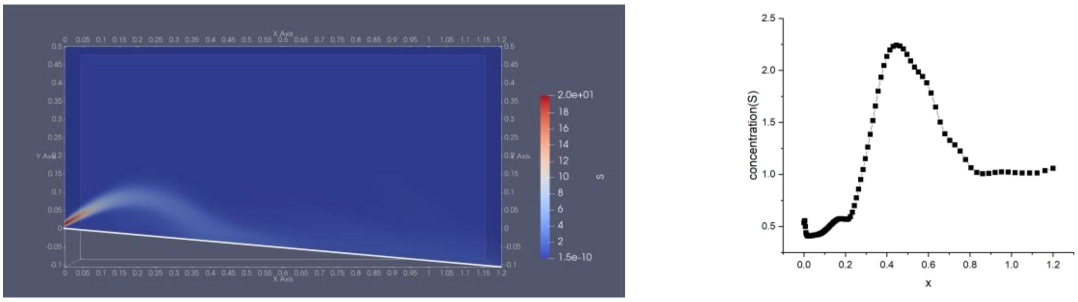

(a) (b)

*(a) Demonstration of the white line along the bottom (b)Concentration variation on the white line and determination of impact point*

Figure 4.22 Illustration of location of impact point

The horizontal and vertical locations of the impact point ( $X_i$ $Y_i$,) normalized by $L_m$ are plotted in Figure 4.23. Compared with the research from Jika (2008) and Oliver *et al.*, (2013), in the present work, the horizontal location was under-predicted compared with the extended solution by (Oliver, 2013). The results were closer to CORJET, which is an Eulerian integral model that uses the entrainment relationship to close the system of differential equations. The vertical location of the impact point was consistent with the previous studies. The location of the impact point was affected by the slope angle; both values for horizontal and vertical coordinates ( $X_i$ $Y_i$,) changed with slope angle.

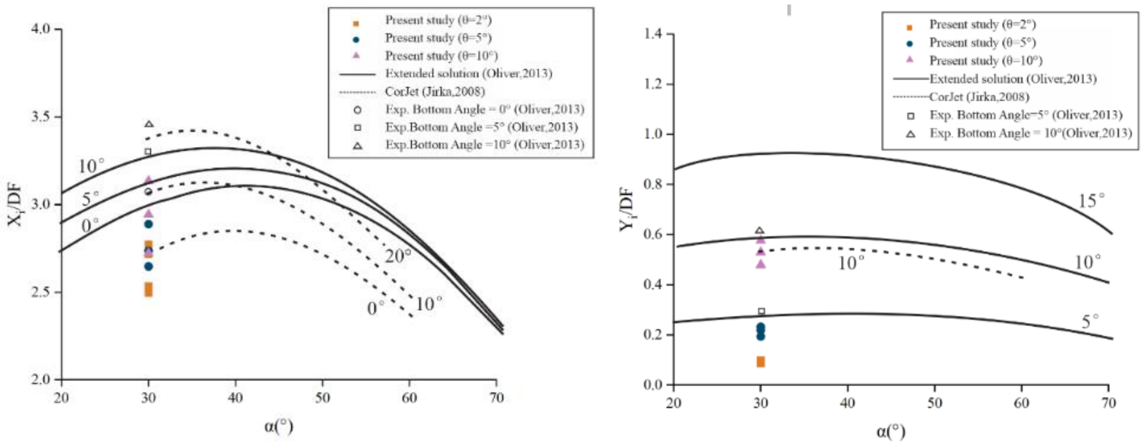

(a) Horizontal location

(b) Vertical location

Figure 4.23 Comparison between normalized location of impact point and previous studies

*Dilution properties at the centerline peak, return point*

As mentioned, the dilution characteristics at some specific location are quite important for outfall design, such as the concentration at the centerline peak ($S_m$) and return point $S_r$. The impact point dilution ($S_i$) is another parameter that can be used for comparison in the sloped environment. It is to be noted that impact point and return point are the same for horizontal bottom but they are different for the case of a sloped bed. Return point is at the same elevation of discharge point but impact point is where the jet hits the bed. Dilutions are normalized by F here.

Figure 4.24 shows that dilution at terminal level and return point can be normalized by Froude number. Normalized minimum dilution at the terminal level and at the return point can be represented by coefficients $\frac{S_m}{F} = C_4, \frac{S_r}{F} = C_6$ (Table 4.4). The evident difference with Shao's study might be due to the measurement methods. The results were still consistent with other studies.

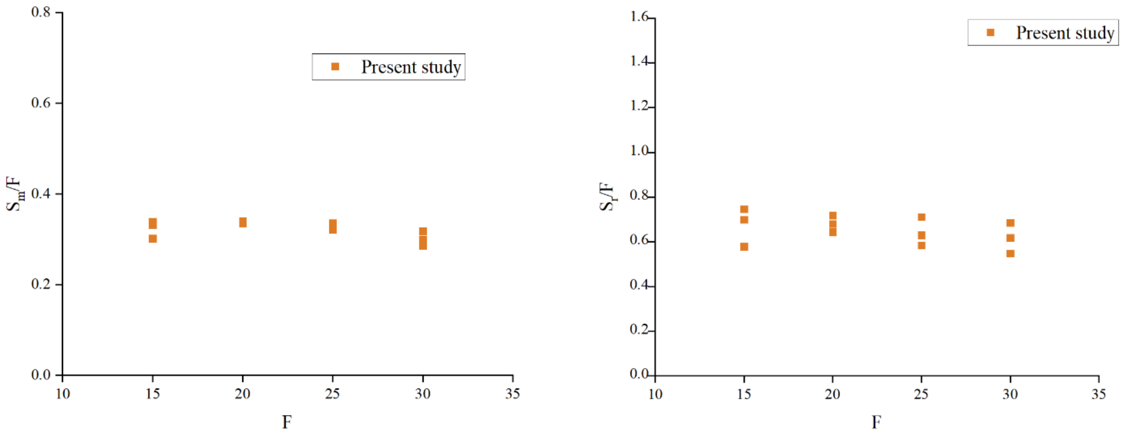

(a) Centerline peak

(b) Return point

Figure 4.24 Normalized dilution Versus Froude number

Table 4.4 Normalized dilution at centerline peak and return point compared with previous studies

| Normalized dilution | Present study | Zeitoun (1971) | Shao and Lao (2010) | EXP.Lai and Lee(2012) | Corjet (Jirka 2008) | Visjet (Lai and Lee 2012) |
|---|---|---|---|---|---|---|
| Centerline peak ($S_m/F$) | 0.34 | 0.36 | 0.62/0.66 | 0.40 | 0.27 | 0.31 |
| Return point ($S_r/F$) | 0.65 | - | 1.45 | 0.82 | 0.55 | 0.64 |

### *Dilution at impact point*

The dilution at the impact point was also normalized by the Froude number. Figure 4.25 shows the normalized dilution plotted against the slope angle which demonstrates shows that dimensionless dilution $\frac{S_i}{F}$ was affected by the sloped bottom.

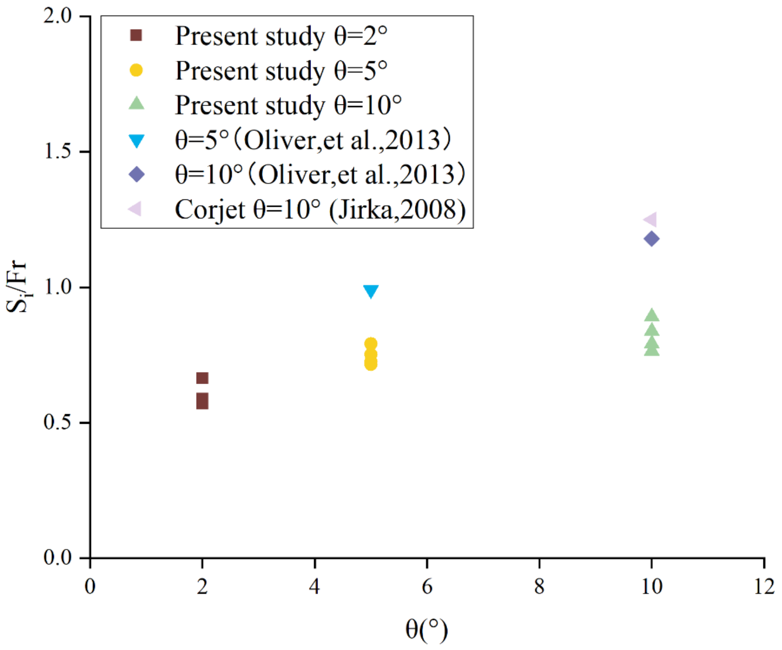

Figure 4.25 Normalized dilation at impact point against slope angle

To figure out how the slope affected jet mixing, the concentration difference between return point and impact point ($\frac{C_r - C_i}{Cr}$) versus slope angle (θ) were plotted in Figure 4.26.

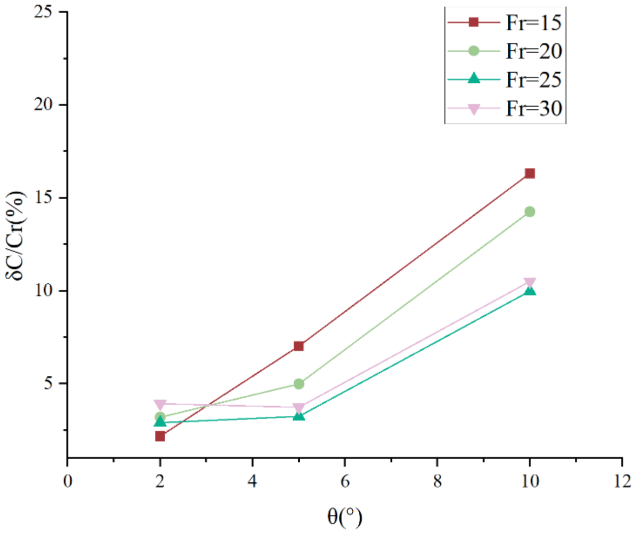

Figure 4.26 Concentration difference between return point and return point

Slope can enhance the dilution from the return point to the impact point, especially for the small Froude number flow (15 and 20), as expected. With a greater slope, the distance between the return point and impact point increase and thus more dilution will occur.

*The concentration variation along the slope*

Many previous studies pointed out that the mixing is significantly reduced after the impact point when the flow stays attached on the bottom, while the ultimate dilution will be higher than the impact point due to the additional complicated mixing processing when the flow becomes horizontal. In this study, the flow moved along the sloped bottom due to gravity after the impact point, which might lead more dilution Figure 4.27 presents the dilution variation after the impact point along the bottom (Fr≤25). When Fr>25, the impact point is close to the boundary and no enough concentration data on the slope after impact point can be provided. Concentration data along the slope after the impact point were used. Dilution was normalized by Froude number, and the location was normalized by DF. The horizontal bottom case was also selected for comparison ($\theta = 0°$).

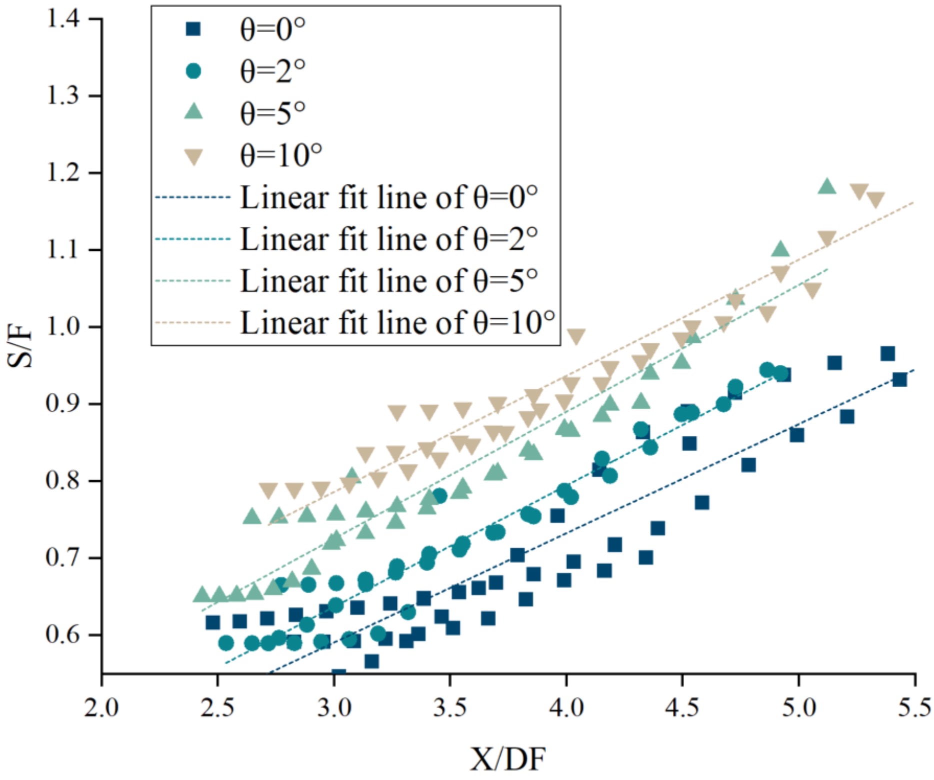

Figure 4.27 Dilution variation on the sloped bottom (Fr≤ 25)

A reasonably linear relationship between the location and dilution was observed for different slope angles in the form of $S/F = a + b(\frac{X}{DF})$. Table 4.5 shows the parameters of the linear fitting line.

Table 4.5 Parameters of the linear approximation

| Equation | $S/F = A + B(X/DF)$ | | | |
|---|---|---|---|---|
| Slope angle | 0° | 2° | 5° | 10° |
| A | 0.166 | 0.165 | 0.232 | 0.333 |
| B | 0.142 | 0.157 | 0.165 | 0.151 |
| $R^2$ | 0.86 | 0.94 | 0.91 | 0.97 |

If average of B is selected, it is possible to get an equation of dilution of any location on the slope:

$$\frac{S}{F} = 0.135 + 0.931\sin\theta + 0.15\left(\frac{\mathrm{X}}{\mathrm{DF}}\right)\ (for\ \theta \leq 10°)$$

The dilution was found to be higher for the larger slope. The slope can enhance the mixing efficiency and also shorten the distance required for the plume to reach a given dilution, which will help protect the creatures that grow on the sea bed. Comparing the case $\theta = 10°$ with $\theta = 0°$, the dilution can be enhanced by around 10%~20%. Thus it is easier to reach the dilution requirements on a sloped bed than on a horizontal bottom, which is of practical value particularly with respect to meeting regulations on the required level of dilution.

## 4.6 Conclusions

IDJ on a sloped bottom in stagnant ambient water was investigated numerically in this study. Three slope angles (2°, 5° and 10°) and 4 different Froude numbers (15, 20, 25, 30; adjusted by density difference in each case) with a source angle of 30 degrees were analyzed by selected RANS models (among which Realizable k-$\epsilon$ being the most accurate) in OpenFOAM. The results showed that the dilution at the impact point can be estimated based on the Froude number and initial conditions. After the impact point, the slope did enhance the dilution of the plume due to the fact that gravity force enhances the speed and thus mixing compared to horizontal bed. The dilution was thus affected by the slope and the dilution after the impact point on the slope appeared linearly related with the distance from the source. For the same jet moving downstream on a slope after the impact point, the slope could enhance the dilution up to 20% compared with the horizontal bed, within the range considered here.

# Chapter 5 Conclusions and recommendations for future work

Inclined dense jets have been widely applied at the outfalls of desalination plants to mitigate the impact on marine environments. Many studies have been done to explore the geometric and mixing characteristics of inclined dense jets in ambient water. Most of them focus on horizontal bottoms. Sloped bottoms should also be addressed due to the natural seabed inclination. Inclined dense jets on sloped bottoms have been rarely studied in the literature. In this thesis, the numerical modeling of inclined dense jets and sloped bottoms was studied for the first time (to the best of the author's knowledge) and the results were compared with limited experiments. 48 numerical simulations were performed via an open source code (OpenFOAM) using a modified *pisoFoam* solver with four different RANS turbulence models, Realizable $-\varepsilon$ , RNG $K-\varepsilon$, Standard $K-\varepsilon$, and nonlinear $K-\varepsilon$.

Realizable $K-\varepsilon$ and Standard $K-\varepsilon$ performed better in predicting dilution among the four models. RNG $K-\varepsilon$ was more stable than the other models but the results were quite different. Nonlinear $K-\varepsilon$ over-predicted the geometrical properties and also had poor performance on dilution prediction.

Many properties of inclined dense jets were compared with experimental studies, and most results were consistent with the experiments, including velocity decay, jet development, important geometric parameters and mixing characteristics.

Compared with horizontal bottoms, a change of geometrical and mixing characteristics after the return point was found in the study. The locations of both points were related with the discharge angle and initial conditions. The impact point was also affected by the slope angle. The dilution from the return point to the impact point increased with the slope angle since the larger slope can provide a longer path between two points. This effect was more obvious for small Froude numbers in this study.In addition, the results also suggested that the dilution after the impact point is highly affected by the slope. The dilution at any point on the slope can be approximated linearly based on its location. Within the range studied in this thesis, the presence of the slope can lead to up to 20% more dilution on the slope compared with a horizontal bottom.

## Recommendations for Future work

The following recommendations are proposed for future work related to this topic:

- Related experimental studies should be conducted, and researchers should focus on the characteristics of the jet after the impact point, as the characteristics after this point are also related to environmental benefits.
- Other turbulence models can also be used for simulation, such as Reynolds Stress Model, LES, .etc.
- The roughness of the bottom should be considered as a factor affecting dilution on the bottom for both experimental and numerical modeling.
- Mesh quality should be improved by different mesh generation methods such as SnappyHexMesh.
- Another multiphase solver such as interFoam, twoliquidMixingFoam and interMixingFoam also are suitable for this type of simulation.
- Larger range of Froude number and bigger computational domain should be taken into consideration.

# References

Abessi, Ozeair, and Philip JW Roberts. "Effect of nozzle orientation on dense jets in stagnant environments." Journal of Hydraulic Engineering 141, no. 8 (2015): 06015009.

Al-Mutaz, Ibrahim S. "Environmental impact of seawater desalination plants." Environmental Monitoring and Assessment 16, no. 1 (1991): 75-84.

Anderson, John David, and J. Wendt. Computational fluid dynamics. Vol. 206. New York: McGraw-Hill, 1995.

Ardalan, Hossein, and Fereidon Vafaei. "CFD and Experimental Study of 45 Inclined Thermal-Saline Reversible Buoyant Jets in Stationary Ambient." Environmental Processes 6, no. 1 (2019): 219-239.

Ardalan, Hossein, Fereidon Vafaei, Mohammad Azizi, Davoud Gohary Kamel, and Azadeh Kalate Arabi. "Investigation of the Velocity and Angle Effects on the Behavior of Brine Discharge by Inclined Jet into the Stationary and Homogenize Ambient." Journal of Oceanography 9, no. 33 (2018): 51-58.

Baig, Mohammed Badrulla, and Abdul Aziz Al Kutbi. "Design features of a 20 migd SWRO desalination plant, Al Jubail, Saudi Arabia." Desalination 118, no. 1-3 (1998): 5-12.

Balabel, A., and W. A. El-Askary. "On the performance of linear and nonlinear k–ε turbulence models in various jet flow applications." European Journal of Mechanics-B/Fluids 30, no. 3 (2011): 325-340.

Baldwin, Barrett, and Timothy Barth. "A one-equation turbulence transport model for high Reynolds number wall-bounded flows." In 29th Aerospace Sciences Meeting, p. 610. 1991.

Bashitialshaaer, Raed, Magnus Larson, and Kenneth M. Persson. "An Experimental Investigation on Inclined Negatively Buoyant Jets." 4, no. 4 (2012): 720-38.

Bleninger, Tobias, and Gerhard H. Jirka. "Modelling and Environmentally Sound Management of Brine Discharges from Desalination Plants." Desalination 221, no. 1-3 (2008): 585-97. https://doi.org/10.1016/j.desal.2007.02.059.

Bleninger, Tobias, Anne Niepelt, and Gerhard Jirka. "Desalination Plant Discharge Calculator." Desalination and Water Treatment 13, no. 1-3 (2010): 156-73.

Bloomfield, Lynn J., and Ross C. Kerr. "Inclined Turbulent Fountains." 451 (2002).

Bosanquet, C., G. Horn, M. Thring, G. I. J. P. o. t. R. S. o. L. S. A. M. Taylor and P. Sciences (1961). "The effect of density differences on the path of jets." 263(1314): 340-352.

Carazzo, G, E Kaminski, and S Tait. "The Rise and Fall of Turbulent Fountains: A New Model for Improved Quantitative Predictions." Journal of fluid mechanics 657 (2010): 265.

Cebeci, Tuncer, G. J. Mosinskis, and A. M. O. Smith. "Calculation of viscous drag in incompressible flows." Journal of Aircraft 9, no. 10 (1972): 691-692.

Chen, Ching Jen, and Wolfgang Rodi. "Vertical turbulent buoyant jets: a review of experimental data." *STIA* 80 (1980): 23073.

Chen, Zhaohui, Jin Wu, Glen B. Baker, Marise Parent, and Norman J. Dovichi. "Application of Capillary Electrophoresis with Laser-Induced Fluorescence Detection to the Determination of Biogenic Amines and Amino Acids in Brain Microdialysate and Homogenate Samples." 914, no. 1-2 (2001): 293-98.

Cheung, S. K. B., D. Y. L. Leung, W. Wang, Joseph Hun Wei Lee, and Valiant Cheung. "VISJET-a computer ocean outfall modelling system." In Proceedings Computer Graphics International 2000, pp. 75-80. IEEE, 2000.

Choi, KW, Chris CK Lai, and Joseph HW Lee. "Mixing in the Intermediate Field of Dense Jets in Cross Currents." Journal of Hydraulic Engineering 142, no. 1 (2016): 04015041.

Chou, P Yo. "On Velocity Correlations and the Solutions of the Equations of Turbulent Fluctuation." Quarterly of Applied Mathematics 3, no. 1 (1945): 38-54.

Chu, Paul CK, Joseph H Lee, and Vincent H Chu. "Spreading of Turbulent Round Jet in Coflow." Journal of Hydraulic Engineering 125, no. 2 (1999): 193-204.

Cipollina, A., A. Brucato, F. Grisafi, and S. Nicosia. "Bench-scale investigation of inclined dense jets." Journal of Hydraulic Engineering 131, no. 11 (2005): 1017-1022.

Cipollina, Andrea, Angelo Bonfiglio, Giorgio Micale, and Alberto Brucato. "Dense jet modelling applied to the design of dense effluent diffusers." Desalination 167 (2004): 459-468.

Coolen, M. C. J., R. N. Kieft, C. C. M. Rindt, and A. A. Van Steenhoven. "Application of 2-D LIF temperature measurements in water using a Nd: YAG laser." Experiments in Fluids 27, no. 5 (1999): 420-426.

Davidson, Lars. "Second-order corrections of the k-ε model to account for non-isotropic effects due to buoyancy." International Journal of Heat and Mass Transfer 33, no. 12 (1990): 2599-2608.

Davidson, M. J., and R. I. Nokes. "NEAR FIELD MIXING OF DESALINATION PLUMES." (2007).

Deardorff, James W. "A numerical study of three-dimensional turbulent channel flow at large Reynolds numbers." J. Fluid Mech 41, no. 2 (1970): 453-480.

Ehrhard, Jan. Untersuchung linearer und nichtlinearer Wirbelviskositätsmodelle zur Berechnung turbulenter Strömungen um Gebäude. VDI-Verlag, 1999.

Ferrier, A. J., D. R. Funk, and P. J. W. Roberts. "Application of optical techniques to the study of plumes in stratified fluids." Dynamics of Atmospheres and Oceans 20, no. 1-2 (1993): 155-183.

Fox, Rodney O. "Large-eddy-simulation tools for multiphase flows." Annual Review of Fluid Mechanics 44 (2012): 47-76.

Frick, Walter E. "Non-empirical closure of the plume equations." Atmospheric Environment (1967) 18, no. 4 (1984): 653-662.

Gildeh, H. Kheirkhah, A. Mohammadian, I. Nistor, and H. Qiblawey. "Numerical modelling of brine discharges using OpenFOAM." In Proc. Int. Conf. New Trends Transp. Phenom., Ottawa, Ontario, Canada. 2014.

Groume-Grjimailo, W. E. (1923). "The flow of gases in furnaces. New York: Wiley."

Holly, F. M., and John L. Grace. Model Studies of Outfall Systems for Desalination Plants:(part I--flume Study). No. 714. US Office of Saline Water, 1971.

Ince, N. Z., and B. E. Launder. "Three-dimensional and heat-loss effects on turbulent flow in a nominally two-dimensional cavity." International journal of heat and fluid flow 16, no. 3 (1995): 171-177.

Issa, Raad I., A. D. Gosman, and A. P. Watkins. "The computation of compressible and incompressible recirculating flows by a non-iterative implicit scheme." Journal of Computational Physics 62, no. 1 (1986): 66-82.

Jamshed, Shamoon. Using HPC for Computational Fluid Dynamics: A Guide to High Performance Computing for CFD Engineers. Academic Press, 2015.

Jirka, Gerhard H. "Improved discharge configurations for brine effluents from desalination plants." Journal of Hydraulic Engineering 134, no. 1 (2008): 116-120.

Jirka, Gerhard H. "Integral model for turbulent buoyant jets in unbounded stratified flows. Part I: Single round jet." Environmental Fluid Mechanics 4, no. 1 (2004): 1-56.

Jones, Edward, Manzoor Qadir, Michelle TH van Vliet, Vladimir Smakhtin, and Seong-mu Kang. "The state of desalination and brine production: A global outlook." Science of the Total Environment 657 (2019): 1343-1356.

Kheirkhah Gildeh, Hossein, Abdolmajid Mohammadian, Ioan Nistor, Hazim Qiblawey, and Xiaohui Yan. "Cfd Modeling and Analysis of the Behavior of 30° and 45° Inclined Dense Jets – New Numerical Insights." Journal of Applied Water Engineering and Research 4, no. 2 (2016-07-02 2016): 112-27.

Kheirkhah Gildeh, Hossein. "Numerical Modeling of Thermal/Saline Discharges in Coastal Waters." PhD diss., Université d'Ottawa/University of Ottawa, 2013.

Kikkert, Gustaaf A., M. J. Davidson, and R. I. Nokes. " Inclined negatively buoyant discharges." Journal of Hydraulic Engineering 133, no. 5 (2007): 545-554.

Kikkert, Gustaaf A., Mark J. Davidson, and Roger I. Nokes. "Buoyant jets with three-dimensional trajectories." Journal of hydraulic research 48, no. 3 (2010): 292-301.

Kolmogorov, A. N. "Equations of motion of an incompressible turbulent fluid." Izv Akad Nauk SSSR Ser Phys 6, no. 6 (1942): 56-58.

Krishnan, Vivek. Advancing detached eddy simulation. Arizona State University, 2008.

Lai, Chris CK, and Joseph HW Lee. "Initial mixing of inclined dense jet in perpendicular crossflow." Environmental Fluid Mechanics 14, no. 1 (2014): 25-49.

Lai, Chris CK, and Joseph HW Lee. "Mixing of inclined dense jets in stationary ambient." Journal of hydro-environment research 6, no. 1 (2012): 9-28.

Lane-Serff, G. F., P. F. Linden, and M. Hillel. "Forced, angled plumes." Journal of hazardous materials 33, no. 1 (1993): 75-99.

Latteman, Sabine. Development of an environmental impact assessment and decision support system for seawater desalination plants. CRC press, 2010.

Launder, Brian Edward, and Dudley Brian Spalding. Mathematical models of turbulence. No. BOOK. Academic press, 1972.

Launder, Brian Edward, G. Jr Reece, and W. Rodi. "Progress in the development of a Reynolds-stress turbulence closure." Journal of fluid mechanics 68, no. 3 (1975): 537-566.

Lee, Joseph Hun-wei, and Vincent Chu. Turbulent jets and plumes: a Lagrangian approach. Springer 2012.

Lee, Myoungkyu, Nicholas Malaya, and Robert D. Moser. "Petascale direct numerical simulation of turbulent channel flow on up to 786k cores." In SC'13: Proceedings of the International Conference on High Performance Computing, Networking, Storage and Analysis, pp. 1-11. IEEE, 2013.

Lindberg, W. R. "Experiments on negatively buoyant jets, with and without cross-flow." In Recent research advances in the fluid mechanics of turbulent jets and plumes, pp. 131-145. Springer, Dordrecht, 1994.

Liu, F., and J. X. Wen. "The effect of turbulence modelling on the CFD simulation of buoyant diffusion flames." Fire safety journal 37, no. 2 (2002): 125-150.

Liu, J. T., Z. G. Zuo, S. H. Liu, and Y. L. Wu. " Pressure fluctuation prediction of a model pump turbine at no load opening by a nonlinear k-ε turbulence model." In IOP Conference Series: Earth and Environmental Science, vol. 22, no. 3, p. 032031. IOP Publishing, 2014.

Madni, I. K., and S. Z. Ahmad. "Prediction of turbulent, axisymmetric, dense jets discharged to quiescent ambients." Mathematical and Computer Modelling 12, no. 3 (1989): 363-370.

Marti, Clelia L., Jason P. Antenucci, David Luketina, Patricia Okely, and Jörg Imberger. "Near-field dilution characteristics of a negatively buoyant hypersaline jet generated by a desalination plant." Journal of Hydraulic Engineering 137, no. 1 (2011): 57-65.

McCutcheon, Steven C. "Water quality modeling." Encyclopedia of Hydrological Sciences (2006).

McKendrick, Donna. "Physical Modelling of Turbulent Single-and Multi-phase, Impinging Jets using Particle Image Velocimetry (PIV)." PhD diss., University of Leeds, 2015.

Menter, Florian R. "Two-equation eddy-viscosity turbulence models for engineering applications." AIAA journal 32, no. 8 (1994): 1598-1605.

Menter, Florianr. "Zonal two equation kw turbulence models for aerodynamic flows." In 23rd fluid dynamics, plasmadynamics, and lasers conference, p. 2906. 1993.

Millero, Frank J., and Alain Poisson. "International one-atmosphere equation of state of seawater." Deep Sea Research Part A. Oceanographic Research Papers 28, no. 6 (1981): 625-629.

Mohammadian, Abdolmajid, Hossein Kheirkhah Gildeh, and Ioan Nistor. "CFD modeling of effluent discharges: a review of past numerical studies." Water 12, no. 3 (2020): 856.

Nemlioglu, S., and P. J. W. Roberts. "Experiments on dense jets using three-dimensional laser-induced fluorescence (3DLIF)." In 4th International conference on marine waste water disposal and marine environment. 2006.

Nemlioglu, Semih, and Naim Sezgin. "Water depth effects on initial dilution of horizontally discharged cold water from an elevated outfall." International Journal of Global Warming 6, no. 2-3 (2014): 284-294.

Nikiforakis, I. K., G. C. Christodoulou, and A. I. Stamou. "Bottom concentration field due to impingement of inclined dense jets on a slope." In Proceedings of the 7th international symposium on environmental hydraulics, Singapore, pp. 54-57. 2014.

Oliver, C. J., M. J. Davidson, and R. I. Nokes. "k-ε Predictions of the initial mixing of desalination discharges." Environmental Fluid Mechanics 8, no. 5-6 (2008): 617.

Oliver, C. J., M. J. Davidson, and R. I. Nokes. "Behavior of dense discharges beyond the return point." Journal of hydraulic engineering 139, no. 12 (2013a): 1304-1308.

Oliver, C. J., M. J. Davidson, and R. I. Nokes. "Removing the boundary influence on negatively buoyant jets." Environmental Fluid Mechanics 13, no. 6 (2013b): 625-648.

Oliver, Cameron. "Near field mixing of negatively buoyant jets." PhD diss . (2012).

Orszag, Steven A., and G. S. Patterson Jr. "Numerical simulation of three-dimensional homogeneous isotropic turbulence." Physical Review Letters 28, no. 2 (1972): 76.

Papakonstantis, Ilias G., George C. Christodoulou, and Panos N. Papanicolaou. "Inclined negatively buoyant jets 1: geometrical characteristics." Journal of Hydraulic Research 49, no. 1 (2011a): 3-12.

Papakonstantis, Ilias G., George C. Christodoulou, and Panos N. Papanicolaou. "Inclined negatively buoyant jets 2: concentration measurements." Journal of Hydraulic Research 49, no. 1 (2011b): 13-22.

Papanicolaou, Panos N., Ilias G. Papakonstantis, and George C. Christodoulou. "On the entrainment coefficient in negatively buoyant jets." Journal of Fluid Mechanics 614 (2008): 447-470.

Peiró, Joaquim, and Spencer Sherwin. "Finite difference, finite element and finite volume methods for partial differential equations." In Handbook of materials modeling, pp. 2415-2446. Springer, Dordrecht, 2005.

Piomelli, Ugo, and Elias Balaras. "Wall-layer models for large-eddy simulations." Annual review of fluid mechanics 34, no. 1 (2002): 349-374.

Prandtl, L. "Report Oninvestigation O, Fdeveloped Turbulence." Mechanik 5, no. 2 (1925).

Ramakanth, Aditya. "Quantifying boundary interaction of negatively buoyant jets." (2016).

Reynolds, Osborne. "IV. On the dynamical theory of incompressible viscous fluids and the determination of the criterion." Philosophical transactions of the royal society of london.(a.) 186 (1895): 123-164.

Roberts, Philip JW, Adrian Ferrier, and Greg Daviero. "Mixing in inclined dense jets." Journal of Hydraulic Engineering 123, no. 8 (1997): 693-699.

Rodi, W., and G. Scheuerer. "Scrutinizing the k-ε turbulence model under adverse pressure gradient conditions." (1986): 174-179.

Rogallo, Robert Sugden. Numerical experiments in homogeneous turbulence. Vol. 81315. National Aeronautics and Space Administration, 1981.

Scharnowski, Sven, and Christian J. Kähler. "On the effect of curved streamlines on the accuracy of PIV vector fields." Experiments in fluids 54, no. 1 (2013): 1435.

Schewe, Jacob, Jens Heinke, Dieter Gerten, Ingjerd Haddeland, Nigel W. Arnell, Douglas B. Clark, Rutger Dankers *et al*. "Multimodel assessment of water scarcity under climate change." Proceedings of the National Academy of Sciences 111, no. 9 (2014): 3245-3250.

Schobeiri, Meinhard T. Fluid mechanics for engineers: a graduate textbook. Springer Science & Business Media, 2010.

Sciacchitano, Andrea, Fulvio Scarano, and Bernhard Wieneke. "Multi-frame pyramid correlation for time-resolved PIV." Experiments in fluids 53, no. 4 (2012): 1087-1105.

Seil, G., and Q. Zhang. "CFD modeling of desalination plant brine discharge systems." J. Aust. Water Assoc 37, no. 6 (2010): 79-83.

Shao, Dongdong, and Adrian Wing-Keung Law. "Mixing and boundary interactions of 30 and 45 inclined dense jets." Environmental fluid mechanics 10, no. 5 (2010): 521-553.

Shao, Dongdong. "Desalination discharge in shallow coastal waters." Ph.D. diss., 2010.

Shih, Tsan-Hsing, William W. Liou, Aamir Shabbir, Zhigang Yang, and Jiang Zhu. "A new k-ϵ eddy viscosity model for high Reynolds number turbulent flows." Computers & fluids 24, no. 3 (1995): 227-238.

Smagorinsky, Joseph. "General circulation experiments with the primitive equations: I. The basic experiment." Monthly weather review 91, no. 3 (1963): 99-164.

Spiegel, Edward A. "A Generalization of the Mixing-Length Theory of Turbulent Convection." The Astrophysical Journal 138 (1963): 216.

Turner, James S. "Jets and plumes with negative or reversing buoyancy." Journal of Fluid Mechanics 26, no. 4 (1966): 779-792.

UNESCO, WWAP. "The United Nations world water development report 2019: Leaving no one behind." (2019).

Vafeiadou, P., I. Papakonstantis, and G. Christodoulou. "Numerical simulation of inclined negatively buoyant jets." In The 9th international conference on environmental science and technology, September, pp. 1-3. 2005.

Van Maele, Karim, and Bart Merci. "Application of two buoyancy-modified k–ε turbulence models to different types of buoyant plumes." Fire Safety Journal 41, no. 2 (2006): 122-138.

White, Frank M. "Fluid Mechanics 7th edn University of Rhode Island." Publication company: Mc Graw Hill (2010).

Wilcox, D. C. "Turbulence modeling for CFD: DCW industries La Canada." CAL, USA (1998).

Wilcox, David C. "Formulation of the kw turbulence model revisited." AIAA journal 46, no. 11 (2008): 2823-2838.

WILCOX, DAVID. "A half century historical review of the k-omega model." In 29th Aerospace Sciences Meeting, p. 615. 1991.

Wolfshtein, M. "The velocity and temperature distribution in one-dimensional flow with turbulence augmentation and pressure gradient." International Journal of Heat and Mass Transfer 12, no. 3 (1969): 301-318.

Yakhot, Victor, and Leslie M. Smith. "The renormalization group, the ε-expansion and derivation of turbulence models." Journal of scientific computing 7, no. 1 (1992): 35-61.

Yin, Jun-Lian, De-Zhong Wang, Yu-Lin Wu, and D. Keith Walters. "A modified k-ε model for computation of flows with large streamline curvature." Advances in Mechanical Engineering 5 (2013): 592420.

Zeitoun, M. A., and William Franklin McIlhenny. "Conceptual designs of outfall systems for desalination plants." In Offshore Technology Conference. Offshore Technology Conference, 1971.

Zeitoun, M. A., R. O. Reid, W. F. McHilhenny, and T. M. Mitchell. "Model studies of outfall systems for desalination plants." Research and Development Progress Rep 804 (1970).

Zhang, Shuai, Adrian Wing-Keung Law, and Mingtao Jiang. "Large eddy simulations of 45 and 60 inclined dense jets with bottom impact." Journal of hydro-environment research 15 (2017): 54-66.

Zhang, Shuai, Baoxin Jiang, Adrian Wing-Keung Law, and Bing Zhao. "Large eddy simulations of 45 inclined dense jets." Environmental Fluid Mechanics 16, no. 1 (2016): 101-121.

# Appendix A Experimental geometric and dilution coefficients from previous IDJ studies

Table A.1. 15° empirical coefficients

| Previous studies | $X_m/dF_0$ | $Y_m/dF_0$ | $\mathrm{Y}_t/dF_0$ | $\mathrm{S}_m/F_0$ | $X_r/dF_0$ | $\mathrm{S}_r/dF_0$ |
|---|---|---|---|---|---|---|
| Lane-Serff *et al*. (1993) | - | -- | 0.57±0.08 | | | |
| Nemlioglu and Roberts (Nemlioglu 2006) | - | -- | 0.68 | | 2.4 | 1.4 |
| Kikkert *et al*.(2007) LA data | 1.3 | 0.22 | 0.57 | | 2.3 | |
| Kikkert *et al*.(2007) LIFdata | 1.5 | 0.26 | -0.6 | - | 2.59 | |
| Lai and Lee (2012) | | - | - | 0.27±0.01 | | 0.42±0.03 |
| VISJET(Lai and Lee 2012) | 1.19 | 0.21 | 0.52 | -0.24 | | 0.44 |
| CorJet (Jirka 2008) | 1.18 | 0.2 | 0.54 | 0.21 | 1.9 | 0.39 |
| Analytical Model (Kikkert *et al*. 2007) | 1.28 | 0.23 | | 0.25 | 2.41 | |

Table 2. 30° empirical coefficients

| Previous studies | $X_m/dF_0$ | $Y_m/dF_0$ | $\mathrm{Y}_t/dF_0$ | $\mathrm{S}_m/F_0$ | $X_r/dF_0$ | $\mathrm{S}_r/dF_0$ |
|---|---|---|---|---|---|---|
| Zeitoun *et al*. (1970) | - | | 1.15 | 0.36 | | |
| Lane-Serff *et al*. (1993) | - | -- | 1.10±0.11 | | | |
| Lindberg (1994) | 2.39±0.32 | | 1.27±0.17 | | | |
| Bloomfield and Kerr (2002) | | | 1.19 | | | |
| Cipollona *et al*. (2005) | 1.95 | 0.79 | 1.08 | | 3.03 | |
| Nemlioglu and Roberts (2006) | - | -- | 1.4 | | 3.3 | 1.9 |
| Kikkert *et al*.(2007) LA data | 1.79 | 0.6 | 1.06 | | 3.17 | |
| Kikkert *et al*.(2007) LIFdata | 1.86 | 0.69 | 1.2 | - | | |

| | | | | | | |
|---|---|---|---|---|---|---|
| Shao and Law (2010) $0.1 \leq \frac{H_0}{L_M} \leq 0.15$ | 1.7 | 0.66 | 1.05 | 0.62 | 2.88 | 1.18 |
| Shao and Law (2010) ($\frac{H_0}{L_M} > 0.15$) | 1.54 | | | 0.66 | 3 | 1.45 |
| Lai and Lee (2012) | 1.94 | 0.65 | 0.95 | 0.4±0.01 | 3.17 | |
| VISJET (Lai and Lee 2012) | 1.51 | 0.56 | - | 0.31 | | 0.65 |
| CorJet (Jirka 2008) | 1.48 | 0.56 | 0.95 | 0.27 | 2.53 | 0.56 |
| Analytical Model (Kikkert *et al.* 2007) | 1.72 | 0.63 | 1.07 | 0.34 | 2.96 | 0.68 |

Table 3. 45° empirical coefficients

| Previous studies | $X_m/dF_0$ | $Y_m$ $/dF_0$ | $\mathrm{Y}_t/dF_0$ | $\mathrm{S}_m/F_0$ | $X_r$ $/dF_0$ | $\mathrm{S}_r/dF_0$ |
|---|---|---|---|---|---|---|
| Bosanquet *et al.* (1961) | 2.68 | 1.67 | | | | |
| Zeitoun *et al.* (1970) | | | 1.43 | 0.42 | | |
| Lane-Serff *et al.* (1993) | 1.86±0.25 | | 1.77±0.20 | | | |
| Lindberg (1994) | | | 1.57±0.21 | | | |
| Bloomfield and Kerr (2002) | | | 1.76 | | | |
| Cipollona *et al.* (2005) | 1.8 | 1.17 | 1.61 | | 2.82 | |
| Nemlioglu&Roberts (Nemlioglu 2006) | | | 2.0 | | 3.2 | 1.7 |
| Kikkert *et al.* LA data (Kikkert *et al.* 2007a) | 1.86 | 1.09 | 1.71 | | 3.31 | |
| Kikkert *et al.* LIFdata (Kikkert *et al.* 2007a) | 2.01 | 1.21 | 1.78 | | | |
| Papakonstantis *et al.* (2011a) | 2.03±0.13 | | 1.58±0.03 | | | |
| Papakonstantis *et al.* (2011b) | | 1.17 | | 0.52±0.05 | 3.16 | 1.55±0.14 |
| Shao and Law (2010) ($\frac{H_0}{L_M} > 0.05$) | 1.69 | 1.14 | 1.47 | 0.46 | 2.83 | 1.26 |
| Lai and Lee (2012) | 2.08 | 1.18 | 1.57 | 0.45±0.05 | 3.32 | 1.09±0.05 |
| VISJET (Lai and Lee 2012) | 1.58 | 1.00 | | 0.32 | | 0.78 |

|  |  |  |  |  |  |  |
|---|---|---|---|---|---|---|
| CorJet (Jirka 2008) | 1.51 | 0.99 | 1.48 | 0.28 | 2.62 | 0.65 |
| Analytical Model (Kikkert *et al*. 2007) | 1.89 | 1.14 | 1.66 | 0.41 | 3.05 | 0.96 |

Table 4. 60° empirical coefficients

| Previous studies | $X_m/dF_0$ | $Y_m/dF_0$ | $\mathrm{Y}_t/dF_0$ | $\mathrm{S}_m/F_0$ | $X_r/dF_0$ | $\mathrm{S}_r/dF_0$ |
|---|---|---|---|---|---|---|
| Zeitoun *et al*. (1970) |  |  | 2.04 | 0.56 |  |  |
| Roberts and Toms (1987) |  |  | 2.08 for F0>20 | 0.38 for F0>25 |  | 1.03 for F0>12 |
| Zeitoun *et al*. (1970) |  |  | 2.33±0.34 |  |  |  |
| Lindberg (1994) | 1.82±0.24 |  | 2.16±0.29 |  |  |  |
| Roberts et al. (1997) |  |  | 2.2 |  | 2.4 | 1.6±12% |
| Bloomfield and Kerr (2002) |  |  | 2.32 |  |  |  |
| Cipollona *et al*. (2005) | 1.42 | 1.77 | 2.32 |  | 2.25 |  |
| Nemlioglu and Roberts (2006) |  |  | 2.85 |  | 3.25 | 1.7 |
| Kikkert *et al*.(2007) LA data | 1.66 | 1.6 | 2.28 |  | 2.78 |  |
| Kikkert *et al*.(2007) LIFdata | 1.80 | 1.76 | 2.45 |  |  |  |
| Papakonstantis *et al*. (2011a) | 1.83±0.08 |  | 2.16±0.04 |  |  |  |
| Papakonstantis *et al*. (2011b) |  | 1.68 |  | 0.56±0.05 | 2.75 | 1.68±0.1 |
| Marti (Marti et al. 2010) |  |  |  |  |  | 1.72 |
| Lai and Lee (2012) | 1.76 | 1.62 | 2.06 | 0.44±0.05 | 2.81 | 1.06±0.03 |
| VISJET (Lai and Lee 2012) | 1.34 | 1.43 |  | 0.29 |  | 0.82 |
| CorJet (Jirka 2008) | 1.24 | 1.38 | 1.93 | 0.27 | 2.23 | 0.69 |
| Analytical Model (Kikkert *et al*. 2007a) | 1.8 | 1.7 | 2.27 | 0.45 | 2.72 | 1.27 |

Table 5. 75° empirical coefficients

| Previous studies | $X_m/dF_0$ | $Y_m$ $/dF_0$ | $Y_t/dF_0$ | $S_m/F_0$ | $X_r$ $/dF_0$ | $S_r/dF_0$ |
|---|---|---|---|---|---|---|
| Lane-Serff *et al*. (1993) | | | 2.82±0.53 | | | |
| Bloomfield and Kerr (2002) | | | 2.59 | | | |
| Ferrari (2004) | | 1.91 | | | 1.66 | |
| Nemlioglu and Roberts (2006) | | | 3.0 | | 1.9 | 1.8 |
| Kikkert *et al*.(2007) LA data | 1.01 | 1.90 | 2.57 | | | |
| Papakonstantis *et al*. (2011a) | 1.15±0.05 | | 2.48±0.07 | | | |
| Papakonstantis *et al*. (2011b) | | 1.93 | | 0.51±0.02 | 1.80 | 1.67±0.15 |
| VISJET (Lai and Lee 2012) | | | | 0.23 | | |
| CorJet (Jirka 2008) | 0.73 | 1.65 | 2.19 | 0.25 | 1.29 | 0.69 |
| Analytical Model (Kikkert *et al*. 2007a) | 1.36 | 2.23 | 2.84 | 0.48 | 1.88 | 1.57 |

# Appendix B Simulation results from turbulence models RNG $-\varepsilon$ , Standard $k-\varepsilon$, and Nonlinear $k-\varepsilon$.

## *Value of y+*

Table B.1. Value of y+ for four model

| Model | Case name ∗ | 215 | 220 | 225 | 230 | 515 | 520 | 525 | 530 | 1015 | 1020 | 1025 | 1030 |
|---|---|---|---|---|---|---|---|---|---|---|---|---|---|
| Realizable $k-\varepsilon$ | LW∗ | 3.33 | 2.93 | 2.27 | 2.26 | 4.10 | 3.8 | 3.80 | 3.80 | 3.96 | 3.72 | 3.70 | 2.85 |
| | BTM ∗ | 2.90 | 2.14 | 0.84 | 0.78 | 2.78 | 2.15 | 2.03 | 2.01 | 2.47 | 1.89 | 1.82 | 0.81 |
| | BW∗ | 14.5 | 12.5 | 25.10 | 24.90 | 16.2 | 14.99 | 14.80 | 14.78 | 15.25 | 14.13 | 14.05 | 29.64 |
| RNG $k-\varepsilon$ | LW | 2.70 | 2.49 | 2.42 | 2.38 | 2.79 | 2.79 | 2.82 | 2.87 | 4.01 | 2.83 | 2.74 | 3.27 |
| | BTM | 3.76 | 2.83 | 2.00 | 1.54 | 3.55 | 20.30 | 1.73 | 1.41 | 3.98 | 2.22 | 1.62 | 1.12 |
| | BW | 20.15 | 18.96 | 17.36 | 15.69 | 21.81 | 20.47 | 18.57 | 18.66 | 22.01 | 20.32 | 19.1 | 7.99 |
| standard $k-\varepsilon$ | LW | 2.60 | 2.45 | 2.41 | 2.34 | 3.26 | 2.7 | 2.67 | 2.59 | 3.12 | 2.77 | 3.39 | 3.24 |
| | BTM | 3.54 | 2.77 | 2.23 | 1.96 | 3.90 | 2.1 | 1.21 | 1.23 | 3.92 | 2.14 | 2.66 | 2.55 |
| | BW | 19.2 | 16.9 | 15.4 | 15.1 | 25.4 | 17.7 | 19.8 | 17.8 | 25.8 | 18.7 | 17.0 | 17.4 |
| Nonlinear $k-\varepsilon$ | LW | 2.21 | 2.57 | 2.57 | 2.6 | 2.32 | 2.6 | 2.6 | 2.57 | 2.02 | 2.66 | 2.96 | 2.6 |
| | BTM | 3.53 | 1.86 | 1.35 | 1.17 | 3.53 | 1.75 | 1.23 | 1.1 | 3.28 | 2.15 | 2.01 | 1.1 |
| | BW | 18.5 | 20.45 | 20.7 | 21.34 | 18 | 22.1 | 20.1 | 21.1 | 13.62 | 19.8 | 18.71 | 19.04 |

∗ : Case name: 215 means slope angle is 2°, Froude number is 15; LW: Leftwall; BTM: Bottom ; BW: Backwall

***Concentration profile (compared with Lai and Lees (2012 experiments))***

*RNG* $k-\varepsilon$

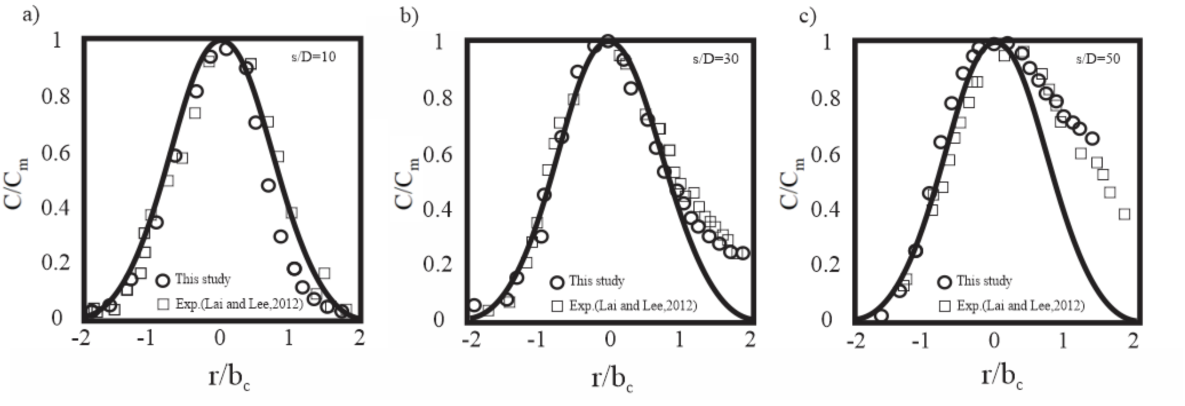

Figure B.1 representative cross-sectional profiles (same profile location as Figure 4.10a)

*Standard* $k-\varepsilon$

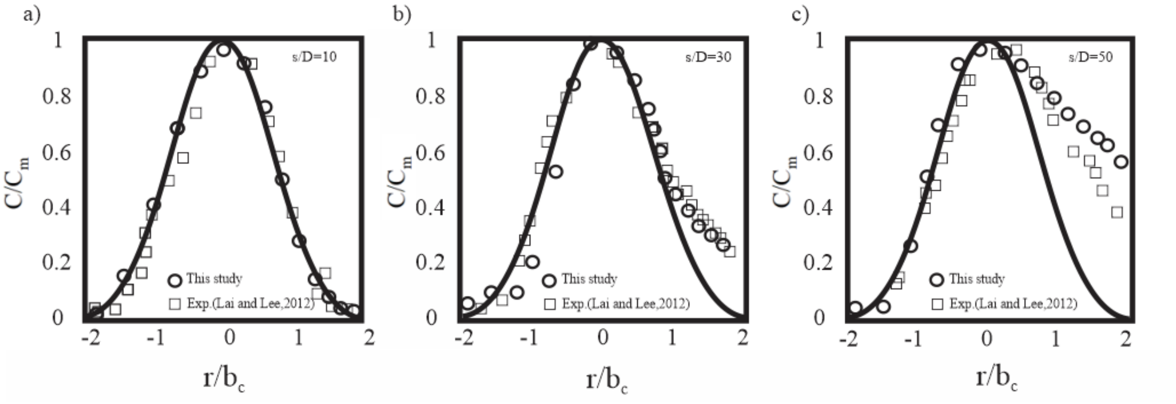

Figure B.2 representative cross-sectional profiles Standard $\mathrm{k}-\varepsilon$

*Nonlinear $k-\varepsilon$*

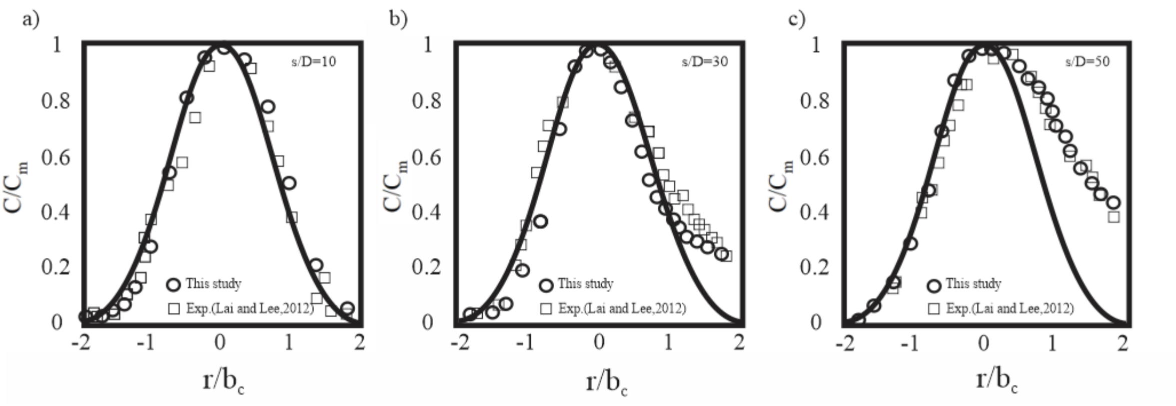

Figure B.3 representative cross-sectional profiles for Nonlinear $\mathrm{k}-\varepsilon$

***Velocity and concentration decay***

*RNG $k-\varepsilon$*

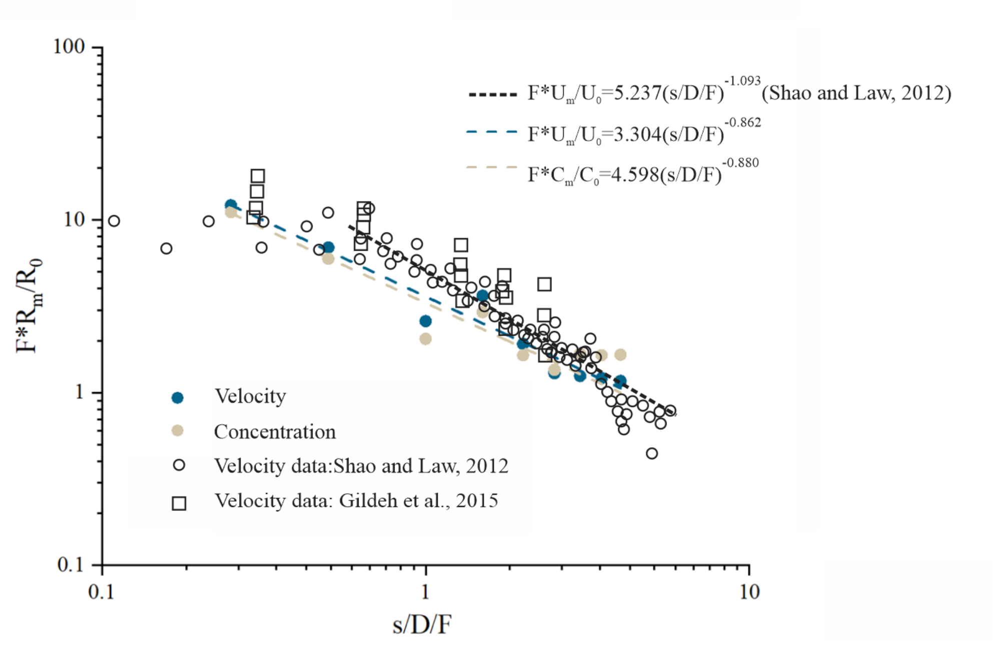

Figure B.4 Non-dimensionalized centerline maximum velocity and concentration magnitude decay for RNG $\mathrm{k}-\varepsilon$ (log scale)

*Standard* $k - \varepsilon$

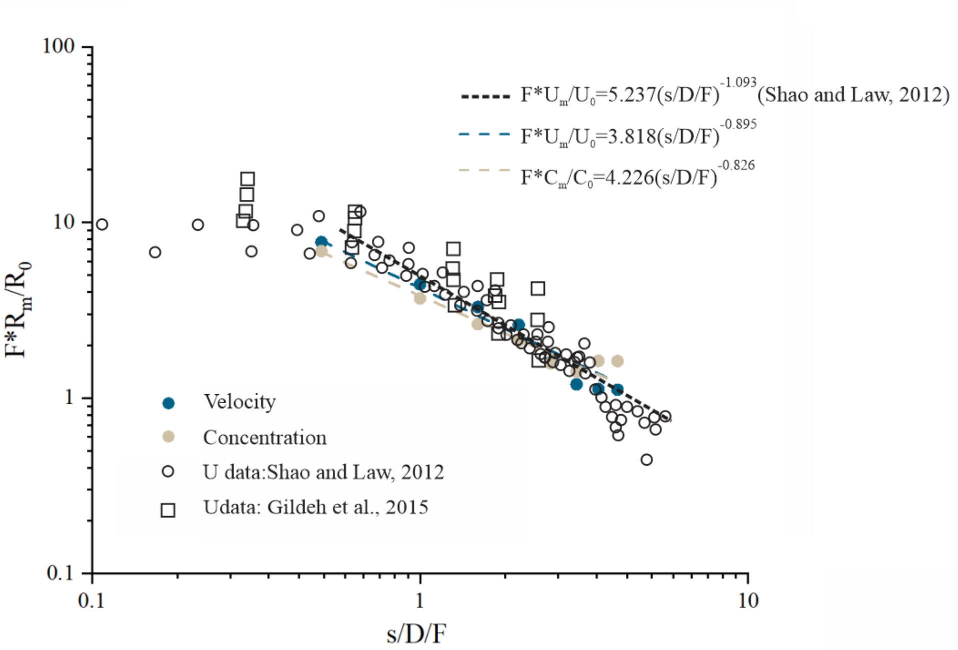

Figure B.5 Non-dimensionalized centerline maximum velocity and concentration magnitude decay for Standard $k - \varepsilon$ (log scale)

*Nonlinear* $k - \varepsilon$

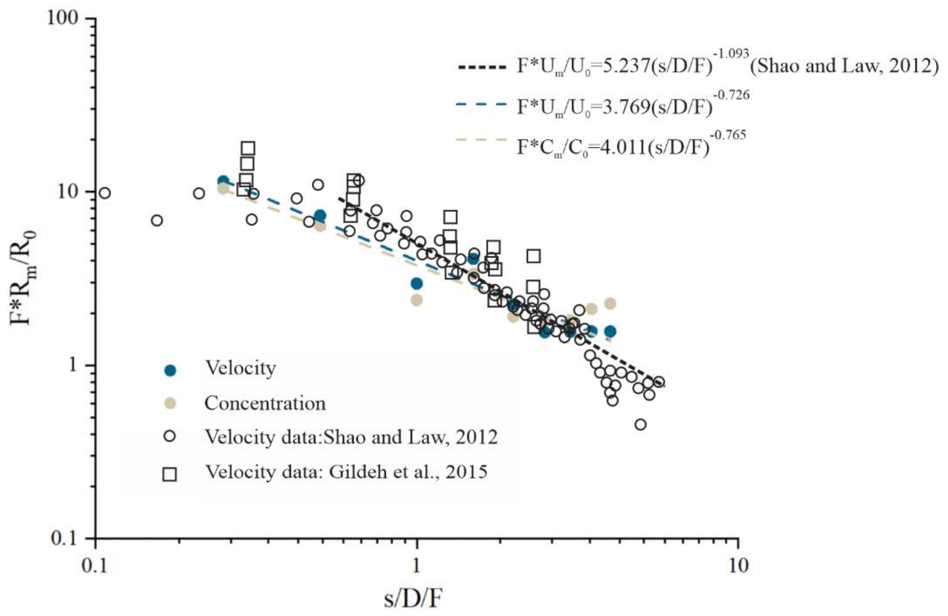

Figure B.6 Non-dimensionalized centerline maximum velocity and concentration magnitude decay for Nonlinear $k - \varepsilon$ (log scale)

***Trajectory***

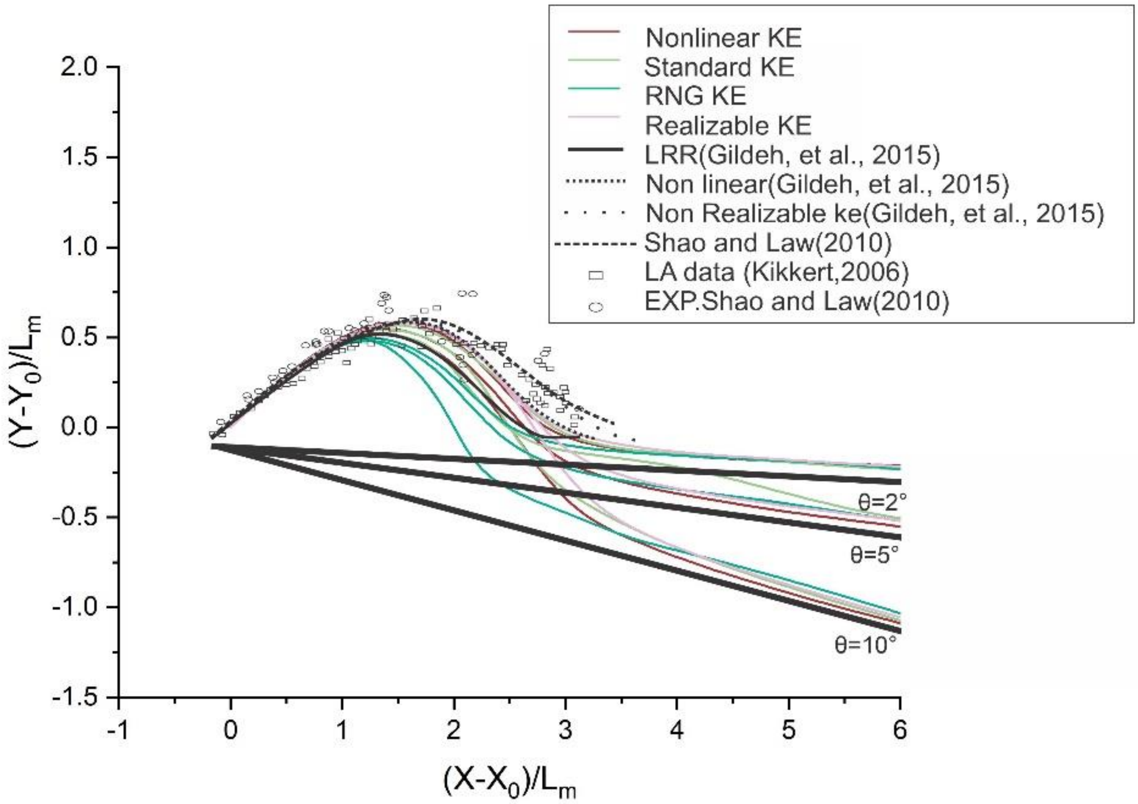

Figure B.7 Trajectories of inclined dense jets from four models

The results of the four selected numerical models showed good agreement with previous studies (Figure B.7). For the Froude number from 15 to 25, the Nonlinear $-\varepsilon$ , Realizable $k-\varepsilon$ and standard $k-\varepsilon$ models are closer to the experimental data. However, the RNG $k-\varepsilon$ model under-predicted the jet trajectories, while for the Fr =30, in RNG $-\varepsilon$ , there is a jump in the trajectory for the slope of 10 degrees. The reason for this is likely due to the limitation of the numerical simulation.

***Location of terminal rise height and return point***

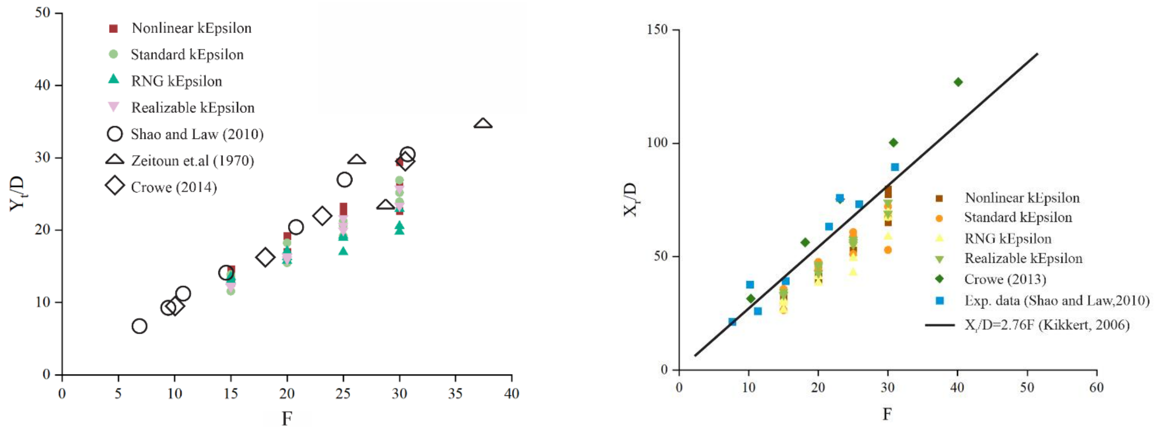

(a) (b)

Figure B.8 (a)Terminal rise height normalized by D against Froude number (b) Return point location normalized by D against Froude number

***Location of centerline peak***

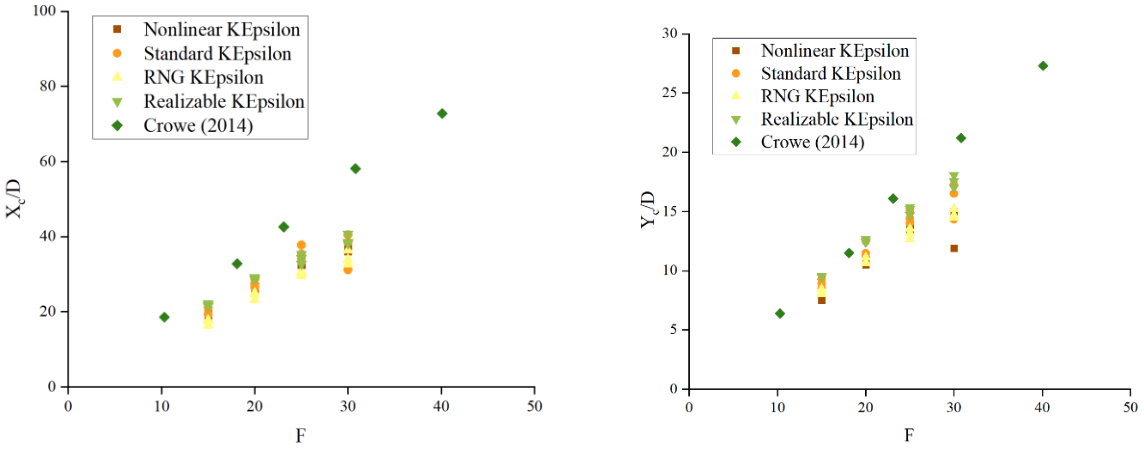

(a) (b)

Figure B.9 (a) Horizontal location of centerline peak normalized by D against Froude number (b) Vertical location of centerline peak normalized by D against Froude number

Table B.2 Normalized dilution at centerline peak and return point compared with other studies

| Normalized dilution | Realizable KE | RNG KE | Standard KE | Nonlinear KE | Zeitoun (1971) | Shao and Lao (2010) | EXP.Lai and Lee(2012) | Corjet (Jirka 2008) | Visjet (Lai and Lee 2012) |
|---|---|---|---|---|---|---|---|---|---|
| Centerline peak ($S_m/F$) | 0.34 | 0.35 | 0.33 | 0.32 | 0.36 | 0.62/0.66 | 0.40 | 0.27 | 0.31 |
| Return point ($S_r/F$) | 0.65 | 0.56 | 0.54 | 0.52 | - | 1.45 | 0.82 | 0.55 | 0.64 |

### *Location of the impact point and dilution at the impact point*

*RNG* $k-\varepsilon$

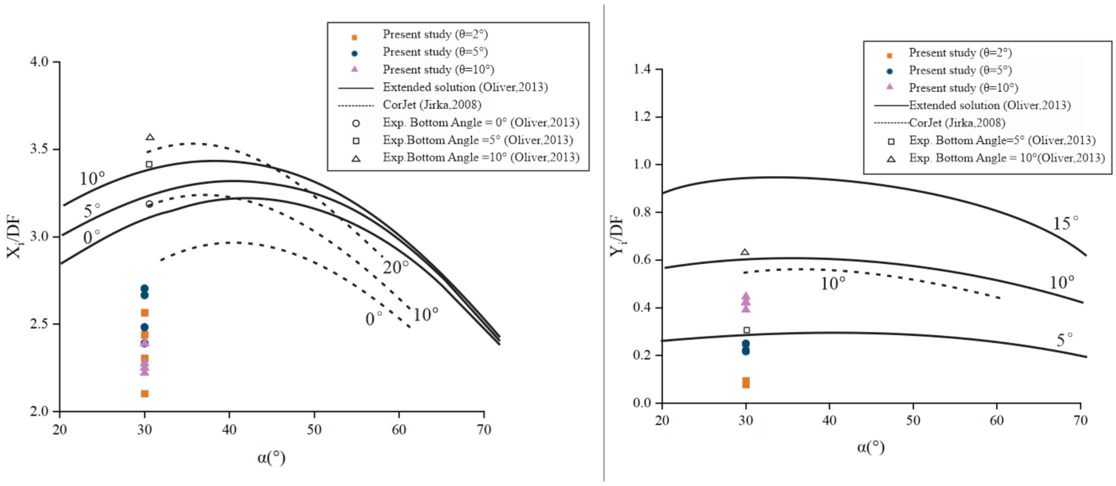

(a) (b)

Figure B.10 (a) horizontal location of impact point; (b) vertical location of impact point (Y is absolute value)

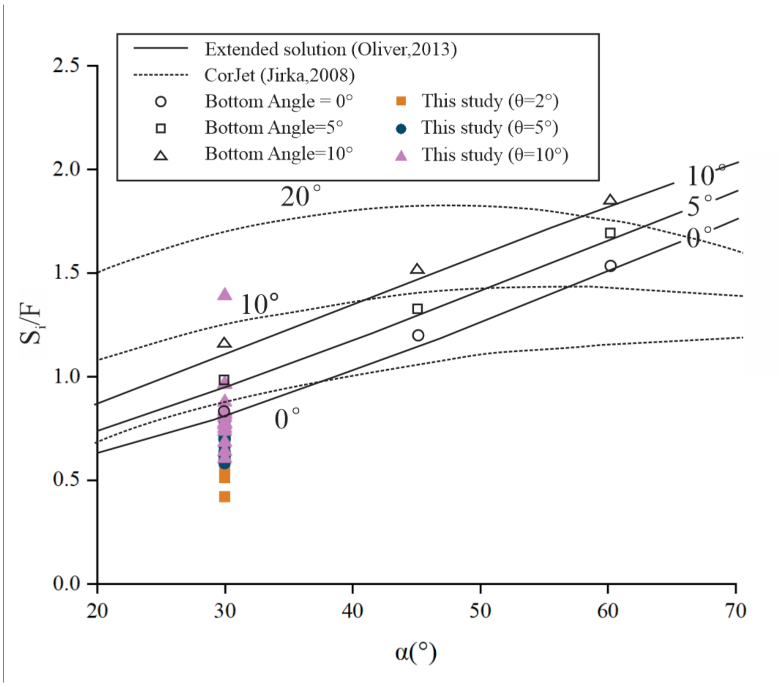

Figure B.11 Dilution at the impact point ($RNG\ \ k-\varepsilon$)

$Standard\ k-\varepsilon$

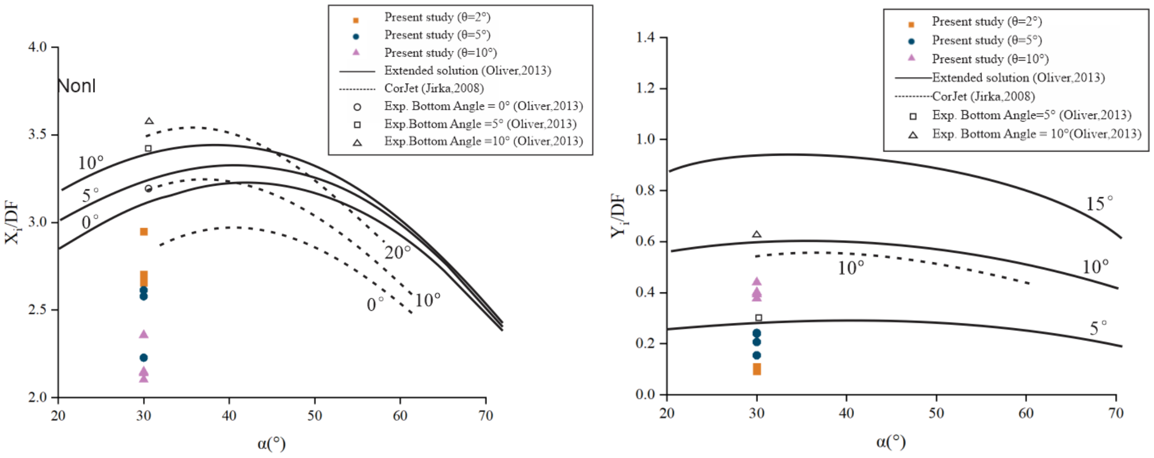

(a) (b)

Figure B.12 (a) horizontal location of impact point ; (b) vertical location of impact point (Y is absolute value)

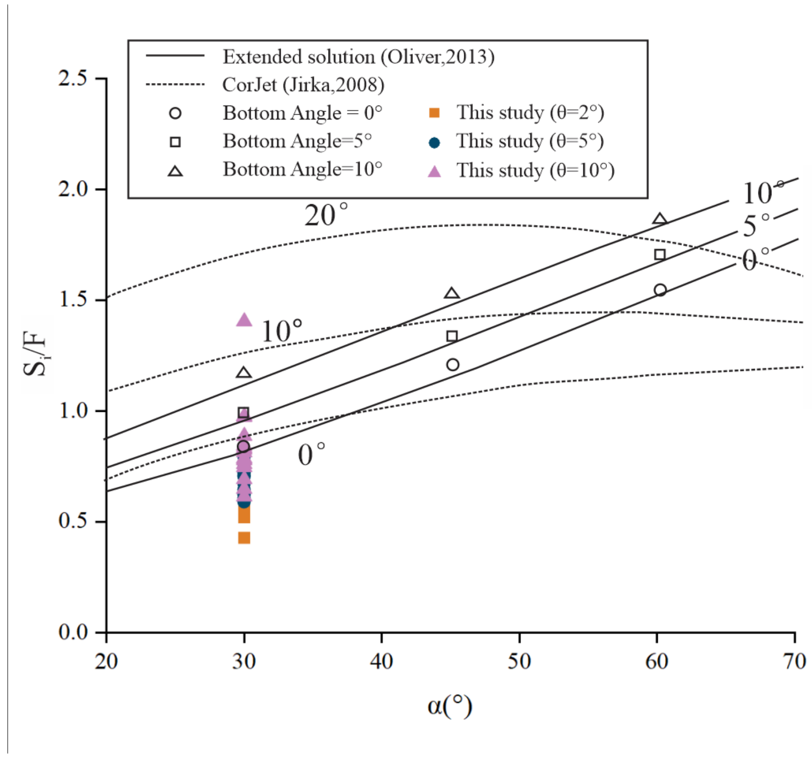

Figure B.13 Dilution at the impact point (Standard $k-\varepsilon$)

*Nonlinear* $k-\varepsilon$

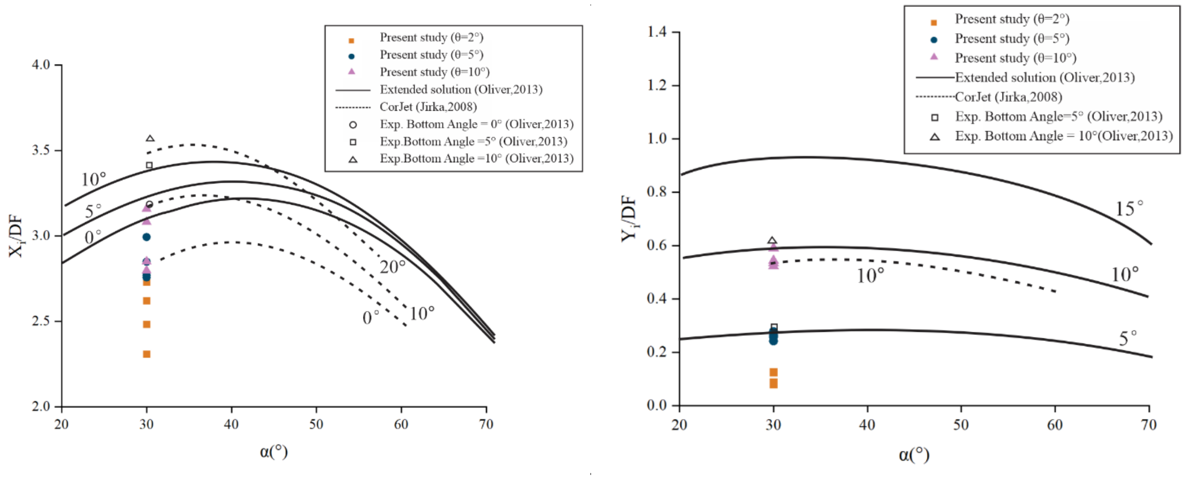

(a)

(b)

Figure B.14 (a) horizontal location of impact point; (b) vertical location of impact point (y is absolute value)

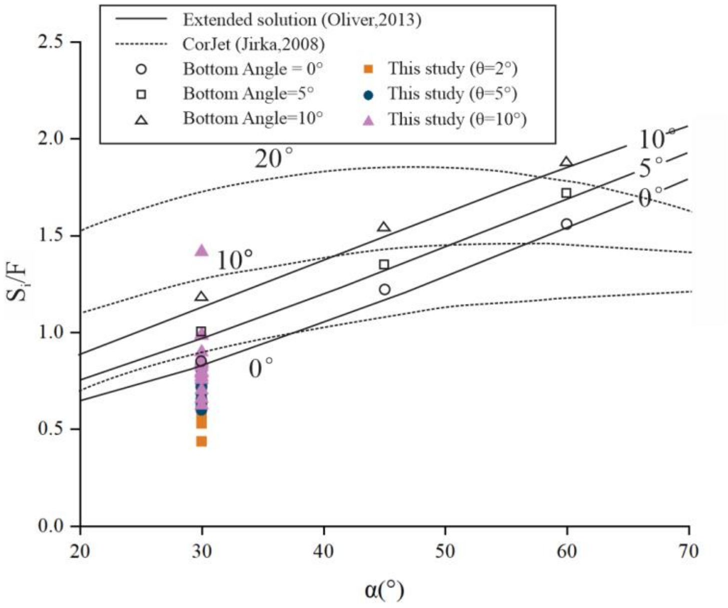

Figure B.15 Dilution at the impact point (Nonlinear $k-\varepsilon$)

*Concentration variation along the slope after the impact point*

*RNG* $k-\varepsilon$ *(Fr=20)*

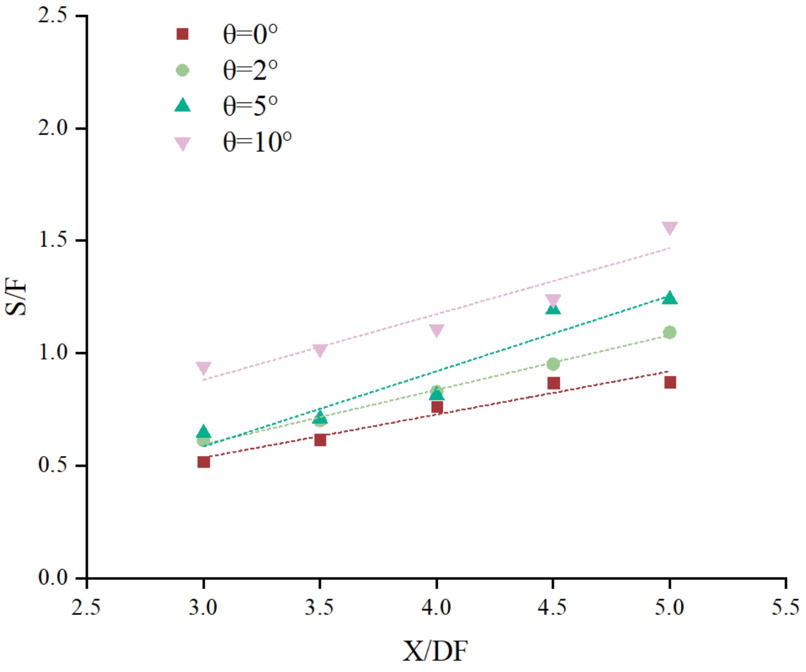

Figure B.16 Dilution variation on the sloped bottom(RNG $k-\varepsilon$)

Table B.3 Parameters of the linear approximation Equation(RNG $k-\varepsilon$)

| Equation(A) | $S/F = a + b(X/DF)$ | | | |
|---|---|---|---|---|
| Slope angle | 0° | 2° | 5° | 10° |
| a | $-0.041$ | $-0.133$ | $-0.419$ | 0.004 |
| b | 0.192 | 0.243 | 0.335 | 0.293 |
| R-square | 0.92 | 0.99 | 0.88 | 0.87 |

*Standard $k-\varepsilon$ (Fr=20)*

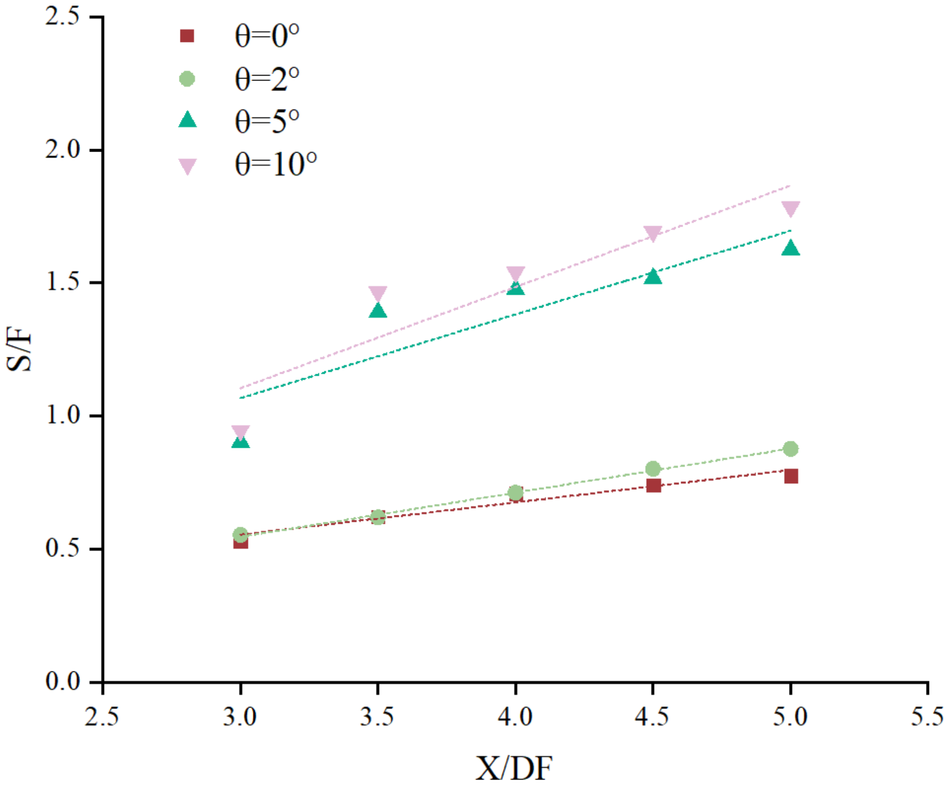

Figure B.17. Dilution variation on the sloped bottom(Standard $k-\varepsilon$)

Table B.4. Parameters of the linear approximation Equation(Standard $k - \varepsilon$)

| Equation(A) | $S/F = a + b(X/DF)$ | | | |
|---|---|---|---|---|
| Slope angle | 0° | 2° | 5° | 10° |
| a | 0.341 | −0.178 | −0.261 | 0.03 |
| b | 0.104 | 0.232 | 0.270 | 0.195 |
| R-square | 0.77 | 0.87 | 0.93 | 0.81 |

*Nonlinear* $k - \varepsilon$*(Fr=20)*

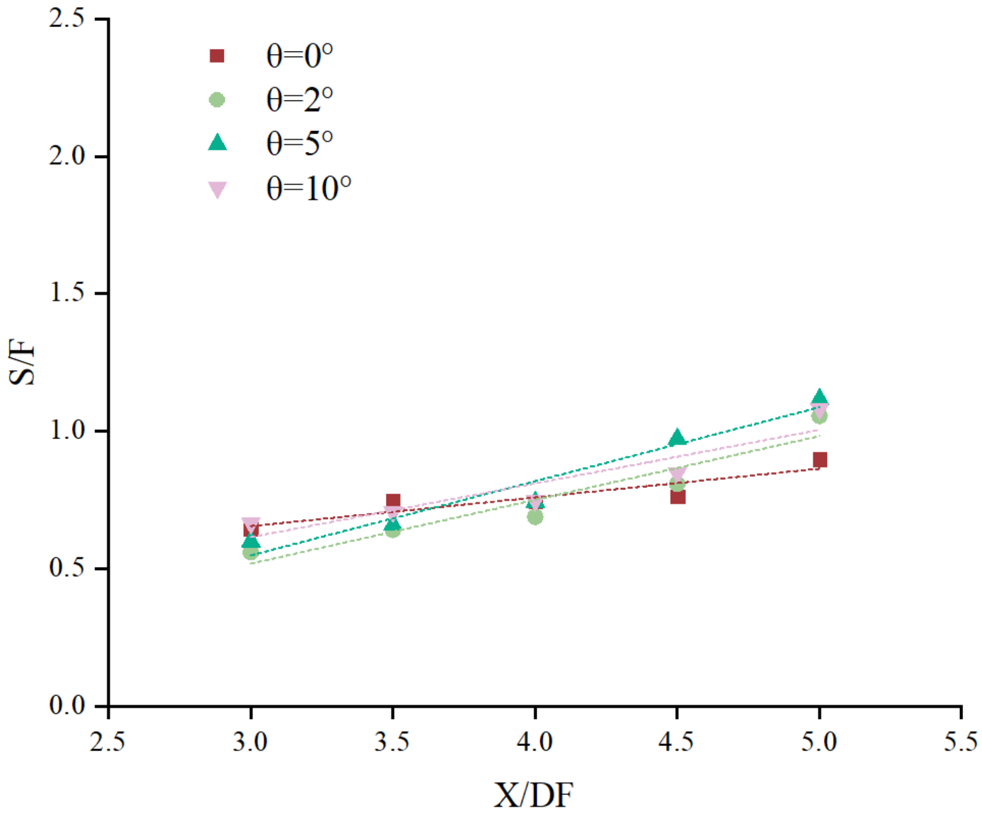

Figure B.18. Dilution variation on the sloped bottom (Nonlinear $k - \varepsilon$)

Table B.5. Parameters of the linear approximation Equation(Nonlinear $k - \varepsilon$)

| Equation(A) | $S/F = a + b(X/DF)$ | | | |
|---|---|---|---|---|
| Slope angle | 0° | 2° | 5° | 10° |
| a | 0.189 | 0.049 | 0.123 | 0.44594 |
| b | 0.121 | 0.166 | 0.315 | 0.11827 |
| R-square | 0.93 | 0.99 | 0.71 | 0.80 |

Comparing the results, the RNG $k - \varepsilon$ and Standard $k - \varepsilon$ illustrate the same trends with Realizable $k - \varepsilon$ that the slope does enhance the dilution after impact point. However, this situation is not observed with the employed Nonlinear $k - \varepsilon$ model. In the results obtained by the standard $k - \varepsilon$, there is a gap between the milder slope angles (0°, 2°) and steeper slopes (5°, 10°). The reason for this behavior could be related to the simplifying assumptions in the standard $k - \varepsilon$ model and ignorance of buoyancy generated turbulence in the present study. The RNG k-ε equation performed more reasonably which could be due to the fact that its turbulent Prandtl number is an analytical formula (rather than a constant), and it considers low Reynolds number viscosity, etc., thus it has better performance for transient flows. More research is needed to analyze the performance of the Nonlinear $k - \varepsilon$ model. Limited research results are available about this model in the context of buoyant jets. It is to be noted that buoyancy generated turbulence was ignored in the present research which could be the subject of future studies.

***Parameters compared with previous studies***

Table B.6. Parameters of three models

| Parameters | | Nonlinear KE | Standard KE | RNG KE | RealizableKE | Lai and Lee (2012) | Shao and Lao (2010) | Kikkert (2007b) | Cippllina (2005) | Crow (2013) | Zeitouns (1970) | Oliver (EXP.) (2012) | Oliver numerical (2012) | Gildeh (2015) | Visjet (Lai and Lee 2012) |
|---|---|---|---|---|---|---|---|---|---|---|---|---|---|---|---|
| Terminal rise height ($Y_t$) | $C_1 = Y_t / L_m$ | 0.88 | 0.84 | 0.78 | 0.90 | 0.95 | - | 1.17 | 1.08 | 1.09 | 1.15 | 1.15 | 1.02 | 1.13 | 0.86 |
| Horizontal location of Terminal rise height($X_t$) | $C_2 = X_t / L_m$ | 1.36 | 1.41 | 1.25 | 1.48 | 1.95 | 1.54 | 1.84/1.75 | 1.95 | 1.87 | - | 1.7 | 1.6 | - | 1.52 |
| Vertical location of centerline peak($Y_c$) | $C_3 = Y_c / L_m$ | 0.53 | 0.57 | 0.52 | 0.61 | 0.65 | - | - | - | 0.69 | - | 0.66 | 0.58 | 0.71 | 0.56 |
| Centerline peak dilution ($S_m/Fr$) | $C_4 = S_m / L_m$ | 0.33 | 0.33 | 0.35 | 0.34 | 0.4 | 0.62 | - | - | - | 0.36 | 0.34 | - | 0.65 | 0.31 |
| Return point($X_r$) | $C_5 = X_r / L_m$ | 2.41 | 2.33 | 2.14 | 2.24 | 3.18 | 3.00 | 3.40/3.07 | 3.03 | 3.56 | - | 3.08 | - | 3.4 | 2.15 |
| Dilution at return point | $C_6 = S_r / Fr$ | 0.52 | 0.54 | 0.56 | 0.65 | 0.82 | 1.45 | - | - | - | - | 0.84 | - | 1.27 | 0.64 |